Title
Molecular Insight into Nonlinear Transport Behaviors

Author
Gao, Ya Chloe

Publication Date
2021

Peer reviewed|Thesis/dissertation

Molecular Insight into Nonlinear Transport Behaviors

by

Ya Gao

A dissertation submitted in partial satisfaction of the

requirements for the degree of

Doctor of Philosophy

in

Chemistry

in the

Graduate Division

of the

University of California, Berkeley

Committee in charge:

Assistant Professor David Limmer, Chair
Professor Phillip Geissler
Assistant Professor Kranthi Mandadapu

Spring 2021

Molecular Insight into Nonlinear Transport Behaviors

Abstract

Molecular Insight into Nonlinear Transport Behaviors

by

Ya Gao

Doctor of Philosophy in Chemistry

University of California, Berkeley

Assistant Professor David Limmer, Chair

Nonlinear response occurs naturally when a strong perturbation takes a system far from equilibrium. Despite of its omnipresence in nanoscale systems, it is difficult to predict in a general and efficient way. Here we introduce a way to compute arbitrarily high order transport coefficients of stochastic systems, using the framework of large deviation theory. Leveraging time reversibility in the microscopic dynamics, we relate nonlinear response to equilibrium multi-time correlation functions among both time reversal symmetric and asymmetric observables, which can be evaluated from derivatives of large deviation functions. This connection establishes a thermodynamic-like relation for nonequilibrium response and provides a practical route to its evaluation, as large deviation functions are amenable to importance sampling. Two important features of this new method are highlighted in this work. Firstly, its efficiency is demonstrated by comparison with direct nonequilibrium simulations, the Green-Kubo method, and brute-force evaluations of the higher order correlation functions. Secondly, its utility in generating molecular insight is showcased in a couple of examples, including the field-dependent conductivities in electrolyte solutions, and thermal rectification in nonlinear lattices.

In addition to the methodology development, we also explore how molecular insight into nonlinear transport behaviors can provide us with design principles for nanoscale devices. This is done by introducing a thermodynamically consistent, minimal stochastic model for complementary logic gates built with field-effect transistors. We characterize the performance of such gates with tools from information theory and study the interplay between accuracy, speed, and dissipation of computations. This work provides a platform to study design principles for low dissipation computing devices harnessing the theoretical developments in stochastic thermodynamics.

To my parents
To Qiao

Contents

Acknowledgments

The past five years has been both a fulfilling and challenging journey, and I have been lucky to have the company of many great mentors and friends along the way. I want to start by giving a special thank to my advisor, David Limmer. David has been highly supportive and nourishing in my intellectual developments towards an independent researcher, and always trustful and respective of my scientific opinions. He has also done tremendous work in fostering a cooperative, friendly and egalitarian research environment, from which I have benefited a lot. His curiosity and working ethics have been and will be a constant source of inspiration for me.

I am also extremely fortunate to count myself as a member of the Chandlerian school of statistical mechanics. I would not have begun such a journey without the encouragement and support from David Chandler. The lectures from him and Phill Geissler were some of the best teaching I've ever received, and help lay a solid foundation for my future research work. My work has also benefited from the guidance of many senior members of the Chandler family, including Phill Geissler, Kranthi Mandadapu, and Gavin Crooks, with all the questions and inspirations, and not to mention the support of the closely-knit Pitzer center community.

Apart from these mentors during graduate school, I'm also deeply indebted to some of my earlier guides in the scientific community - my undergraduate advisors Weihua Li, Hsueh-Chia Chang, Zhen-Gang Wang, and Ahmad Omar. I cannot overemphasise their importance in my forming years as a young scientist. They have not only provided me with essential training in scientific methods as mentors, but also love, care and trust as friends. It is through their eyes that I saw a better version of me that I had not recognized myself.

I could not have survived the past five years without the support of folks in the Limmer group. They have essentially filled the role of my extended family while my biological family are far away. These lovely people have not only been helpful in intellectual exchanges, and cooperative to my administrative work, but also been a strong source of emotional support. I'm sincerely grateful for the company of Addison and Trevor, who are the best cohort I can imagine; Amael and Laura, whose unique French mojo always lights up the room with joy; Shujia and Frank, for giving me the opportunity to become a mentor; Mirza and Sam, who keep a sanity check in the office; Avishek and Ben, who are always there for my complaints when I need them; and all the cool new kids, Aditya, Anthony, Michelle, Tom and Yoon, who have brought so much fun to the workplace. I wish we could have shared more lunches admist fruity laughs, if not for the social distancing situation, but I'm sure our friendship will last longer than the pandemic. Besides friends at the Limmer group, I'd also like to acknowledge my dear friends in the department, especially Jom, Chris, and Dip; and friends I've met at Cambridge, especially Yunwei, Siyu and Fredrik, who have taken great care of me while I was there.

Last but not least, I want to thank my parents for their support in the past five years. Even though we have mostly been an ocean apart, and speak different languages, I have only recently come to realize the gifts they have given me in my forming years - the curiosity, the perseverance, and the courage to live. Of course this passage will not be complete without a

special shout-out to Qiao, my best friend, travel buddy, and pillar of support for the past five years. In those most traumatizing moments, when I'm suffocated with superciliousness and passive aggressiveness, it is Qiao who has always been by my side, supplying me with the air to breathe, and the reason to live. We have left beautiful memories in Tahoe, Morocco, Memphis, Chicago, San Diego, Yosemite, Yellow Stone, Utah, Boston, Seattle, Las Vegas, Montana, Hawaii, Portland and New Mexico, and I can't wait to start the next page of our lives with you.

Chapter 1

Introduction

Transport processes are often described by phenomenological laws, such as Fourier's law for heat conduction, Fick's law for diffusion, and Ohm's law for electrical conduction. These equations propose a simple relationship between the thermodynamic force, or affinity, that drives the system out of equilibrium, and the resultant current, where the strength of the response is described by a material specific transport coefficient. As the external perturbation grows stronger, nonlinear transport behaviors naturally arise, such as shear thinning in complex fluids, and current rectification in electrical transistors. From a practical point of view, such behaviors become especially prevalent in nanoscale systems, where microscopic fluctuations play an important role. As a consequence, understanding the origin of nonlinear effects are key to the design and manipulation of nanoscale devices.

While the evaluation of transport coefficients from molecular dynamics simulations has become a standard practice throughout physics and chemistry, such calculations remain computationally demanding. Transport coefficients are most commonly computed with direct nonequilibrium molecular simulations, where a current is driven through the system by the application of specific boundary conditions [1, 2], or by altering the equations of motion [3–5]. Such methods, however, are generally not transferable among different transport processes, and the result can be sensitive to how the current is generated [6, 7]. Moreover, with direct simulation the computed response is not easily connected to specific molecular degrees of freedom.

On the other hand, statistical mechanics provides a theoretical framework for correlating the macroscopic properties of a system with its microscopic degrees of freedom. While this is achieved successfully for equilibrium systems by Boltzmann and Gibbs, it is natural to ask whether a unified theory can be applied to nonequilibrium systems as well. More specifically, what microscopic quantities should we observe in order to predict transport properties of a macroscopic system? This question has concerned statistical mechanicians since the 1950s. While Onsager laid out a theoretical framework for irreversible processes and proposed the regression hypothesis [8], a major breakthrough came from the work of Kubo [9], and the ensuing development of the so-called Green-Kubo formulas [9, 10]. Kubo showed that the linear transport coefficients can be calculated from equilibrium fluctuations of the current, in

the form of a correlation function. While connections between transport coefficients and the underlying microscopic degrees of freedom are well established when forces are small, such connections are much less clear when forces are large and responses are nonlinear. From a theoretical point of view, a satisfying statistical mechanical theory of transport phenomena should be capable of describing these nonlinear processes as well.

During the 1970-1980's, with the advancement of molecular dynamics simulations, there have been many new developments regarding the nonoequilibrium statistical mechanics of dense classical systems, especially in the area of thermostatted linear response, and nonlinear response theories, such as the Kawasaki [11] and the time transient correlation function formalism [12]. These developments have had a major impact on the computer simulation methods used to model nonequilibrium fluids, and have established a clearer relationship between transport processes and microscopic fluctuations. What remains to be developed is a unified theory of nonequilibrium thermodynamics, especially in the steady state.

The last two decades have observed a growing interest in the field of stochastic thermodynamics, stimulated by new possibilities in experimental interrogation of nanoscale systems. Nonequilibrium fluctuation theorems [13–15] and thermodynamic uncertainty relations [16, 17] impose constraints on the distribution functions of fluctuating thermodynamic quantities like heat and work, which represent refinements of the second law to driven systems. These theoretical developments have enabled the establishment of a more formal theory for nonequilibrium steady states. In particular, a considerable amount of work has been devoted to predicting response coefficients for stochastic systems. Extended fluctuation-dissipation theorems have been derived for linear responses of nonequilibrium steady states [18–21], which can be translated into second order response around equilibrium [22]. More generally, multivariate fluctuation relations imply connections between transport coefficients and cumulants of the current [23, 24]. Many of these advances have been enabled by large deviation theory [25, 26], which provides a set of mathematical tools for characterizing and evaluating fluctuations in nonequilibrium systems. These tools have been employed widely to illustrative model systems, which not only serve as testing grounds for theories, but also reveal new insights into nonequilibrium phenomena [27–29].

In the present work, I aim to extend these earlier efforts in stochastic thermodynamics to a larger class of nonequilibrium systems, with the focus on the efficient evaluation and molecular interpretation of transport coefficients. I will develop a general scheme for the calculation of arbitrarily high order transport coefficients in stochastic systems from microscopic equilibrium fluctuations, and illustrate its viability by computing nonlinear transport coefficients from the derivatives of large deviation functions. The rest of this dissertation is organized as follows. Chapter 1 briefly reviews theoretical descriptions of transport processes, providing the context and background for this work. Chapter 2 is devoted to an illustration of a novel method which relates transport coefficients to large deviation functions. The rest of the chapters provide a sample of nonlinear transport behaviors that can be studied using the method above. We start with ionic transport in electrolyte solutions in Chapter 3, where field-dependent conductivities induced by the Onsager-Wien effect is known as one of the most common nonlinear transport behaviors. In Chapter 4, we explore anomalous heat

transport and thermal rectification behaviors in a nonlinear lattice. Finally in Chapter 5, we turn to nonlinear electron transport in semiconductor devices, which has wide implications in low dissipation computing.

1.1 From Macroscopic to Microscopic Descriptions

The earliest theoretical description of transport processes is the hydrodynamics approach. The field of fluid mechanics, or hydrodynamics, provides a continuous description of transport processes. In this section, we review the basics of hydrodynamics approach and linear irreversible thermodynamics, and comment on some of the limitations of the approach. We also describe how to go from this macroscopic description to microscopic definitions.

While classical mechanics establishes conservation laws of mass, momentum and energy, at the hydrodynamics level we are interested in how their densities evolve over time. This is described by the Navier-Stokes equations, which take the form of continuity equations. For example, the change in the mass density $\rho(\mathbf{r},t)$ at position $\mathbf{r}$ and time t can be described by the streaming velocity $\mathbf{u}(\mathbf{r},t)$ according to

$$\frac{d\rho(\mathbf{r},t)}{dt} = -\rho(\mathbf{r},t)\nabla\cdot\mathbf{u}(\mathbf{r},t)\,, \tag{1.1}$$

while the momentum density evolves according to the pressure tensor $\mathbf{P}(\mathbf{r},t)$,

$$\rho(\mathbf{r},t)\frac{d\mathbf{u}(\mathbf{r},t)}{dt} = -\nabla\cdot\mathbf{P}(\mathbf{r},t)\,, \tag{1.2}$$

and the energy density $e(\mathbf{r},t)$ is described by

$$\rho(\mathbf{r},t)\frac{de(\mathbf{r},t)}{dt} = -\nabla\cdot[\mathbf{q}^h(\mathbf{r},t)+\mathbf{P}(\mathbf{r},t)\cdot\mathbf{u}(\mathbf{r},t)]\,, \tag{1.3}$$

where $\mathbf{q}^h$ is the heat flux vector.What differentiates these nonequilibrium transport processes from their equilibrium counterpart is the production of excess entropy. In the framework of linear irreversible thermodynamics, the entropy production takes the canonical form [30]

$$\sigma = \sum_i J_i X_i\,, \tag{1.4}$$

where J_i are thermodynamic fluxes, X_i are their conjugate thermodynamic affinities, which can be either an external force, or contact with reservoirs. For example, by combining the Navier-Stokes equations with a local version of the Gibbs relation with temperature $T(\mathbf{r},t)$, one can recognize pairs of thermodynamic fluxes and affinities, such as the heat flux $\mathbf{q}^h(\mathbf{r},t)$ conjugate to the temperature gradient $-\nabla T(\mathbf{r},t)T(\mathbf{r},t)^{-2}$, and the viscous pressure tensor $\Pi(\mathbf{r},t)$ conjugate to $-\nabla\mathbf{u}(\mathbf{r},t)T(\mathbf{r},t)^{-1}$.

Furthermore, based on the local thermodynamic equilibrium postulate, which is assumed to be valid sufficiently close to equilibrium, the two are related in a linear relation,

$$J_i = \sum_j L_{ij} X_j \,. \tag{1.5}$$

In the case where multiple types of affinities are applied onto an isotropic system, one can use Curie's principle to greatly simplify the form of the transport coefficient tensor L, and thus justify the linear constitutive equations such as the Fourier's law of heat conduction, and Newton's law of viscosity. By combining these constitutive equations with Navier-Stokes equations, one arrives at a closed system of equations that can be solved exactly.

To summarize, while Navier-Stokes equations give an accurate macroscopic description of fluids, it must be supplemented with the appropriate boundary conditions and constitutive equations. The latter typically comes from postulates in linear irreversible thermodynamics, thus the form of which lacks a molecular justification, and the transport coefficients are usually measured from experiments. In addition, to develop theories based on hydrodynamics approach, one often has to invoke the local thermodynamic equilibrium postulate, which puts constraints on the length and time scales, and the nonequilibrium regime that can be investigated. As an example, the linear phenomenological relation in Eq. 1.5 is clearly a truncation of the Taylor expansion. More generally, a transport process that is driven by a single affinity X is described by the full expansion

$$J = L_0 + L_1 X + L_2 X^2 + O(X^3) \,. \tag{1.6}$$

This nonlinear response relation will be the starting point of our analysis throughout this dissertation. It is worth pointing out that nontrivial response behavior is affordable in the framework of linear irreversible thermodynamics as well, for example by introducing time dependency in the linear constitutive relation Eq. 1.5 so that the flux depends on the history of the affinity. For example, in viscoelastic fluids, the relation between the strain rate γ and the shear stress S_{xy} can be written as [31]

$$S_{xy}(t) = -\int_0^t ds \; \eta(t-s)\gamma(s) \,, \tag{1.7}$$

where η is called the Maxwell memory function. Such a relation is known as non-Markovian, which arise when the strain rate varies significantly over either the time or length scales characteristic of the molecular relaxation for the fluid. However, such a constitutive relation is still a linear one, which is fundamentally different from the nonlinear expansion in Eq. 1.6.

As a first step to go from a macroscopic to microscopic descriptions, one needs to translate the macroscopic quantities defined in continuum into molecular descriptions. Such a procedure is proposed by Irving and Kirkwood [32], which relates hydrodynamic variables to nonequilibrium ensemble averages of microscopic quantities. By introducing some microscopic volume in a system of N particles of mass m, one can define the local density of mass $\rho(\mathbf{r}, t)$

as

$$\rho(\mathbf{r},t) = \left\langle \sum_{i=1}^{N} m\delta(\mathbf{r}-\mathbf{r}_i) \right\rangle , \tag{1.8}$$

where the bracket denotes ensemble average, and similarly for momentum and energy, and then write down conservation equations for these local quantities. This allows us to derive microscopic expression for the thermodynamic fluxes, such as the heat flux

$$\mathbf{q}^h(\mathbf{r},t) = \left\langle \left[\sum_i (\mathbf{v}_i - \mathbf{u}) e_i - \frac{1}{2} \sum_{i,j} \mathbf{r}_{ij} (\mathbf{v}_i - \mathbf{u}) \cdot \mathbf{F}_{ij} O_{ij} \right] \delta(\mathbf{r}-\mathbf{r}_i) \right\rangle , \tag{1.9}$$

where $\mathbf{v}_i$ is the velocity of particle i, $\mathbf{F}_{ij}$ is the force from the pair-wise potential energy, and the operator O_{ij} is given by

$$O_{ij} = \sum_{n=1}^{\infty} \frac{1}{n!} \left(-\mathbf{r}_{ij} \cdot \frac{\partial}{\partial \mathbf{r}} \right)^{n-1} . \tag{1.10}$$

We'll later use these microscopic definitions to compute thermodynamic quantities in molecular simulations.

1.2 Statistical Mechanical Theory of Transport Processes

The theory of statistical mechanics is developed to give a molecular basis for the laws of phenomenological thermodynamics. While it has enjoyed great success for equilibrium systems, it is natural to ask whether it can be extended to phenomenological laws of transport processes. In this section, we review a few classical theories that provide a statistical mechanical basis for transport processes.

The nonequilibrium statistical mechanics of dilute atomic gases is well described by the kinetic theory [33]. However, extending the simple theory to systems of higher densities has proved to be a difficult task. A breakthrough came in 1931 with Onsager's regression hypothesis, which proposes the notion of relating transport coefficients to spontaneous fluctuations in equilibrium [8]. It is asserted that spontaneous fluctuations from thermal equilibrium decay, on the average, according to the transport laws governing the corresponding macroscopic variables. A further connection between the two was established later by deriving the path probability of a given succession of states in a system where the macroscopic variables are Gaussian distributed [34], and it is conjectured that the log-likelihood of a current fluctuation was given by the entropy production [8].

Zwanzig later compared the role of time-correlation functions in the theory of transport processes to partition functions in equilibrium statistical mechanics [35]. However, finding the appropriate form for each distinct transport process has proved to be a daunting task.

A myriad of results have been derived to relate time-correlation functions to transport coefficients, of which we will highlight the work by Kubo and Green below. We restrict ourselves to classical systems, though a similar approach with some modifications can be made for quantum systems.

Time-Correlation Functions

Let's first review some of the properties of time-correlation functions, which will come handy in the rest of this section. We define the time-correlation function between a variable A and another variable B as

$$C_{AB}(t) = \langle A(0)B(t)\rangle_X = \int d\Gamma\, A(0)B(t)f_X(\Gamma)\,, \tag{1.11}$$

where Γ denotes the phase space, and f_X is the steady state phase distribution under some time-invariant affinity X. We list some of its properties below, the proof of which can be found for example in [36].

- Time translational invariance:
  Since the ensemble averages are taken over a stationary distribution, time-correlation functions are only dependent on the time difference t instead of the particular choice of the time origin, i.e.

  $$C_{AB}(t) = \langle A(0)B(t)\rangle_X = \langle A(t_1)B(t_2)\rangle_X\,, \quad t = t_2 - t_1\,. \tag{1.12}$$

  A useful property follows from the time translational invariance for auto-correlation function $C_{AA}(t)$:

  $$\frac{1}{t_{\rm N}}\int_0^{t_{\rm N}} dt' \int_0^{t_{\rm N}} dt''\, \langle A(t')A(t'')\rangle_X = 2\int_0^{\infty} dt\, C_{AA}(t), \quad t_{\rm N}\to\infty\,, \tag{1.13}$$

  where the right hand side takes the Green-Kubo form.

- Time derivative:

  $$\frac{d}{dt}C_{AB}(t) = -C_{\dot{A}B}(t) = C_{A\dot{B}}(t)\,, \tag{1.14}$$

  where the dot denotes time derivatives.

- Symmetry:
  An important property of equilibrium time-correlation functions is derived from the time reversal symmetry of the equation of motion. For each variable, define the time reversal transformation as $A \to \epsilon_A A$, where $\epsilon_A = \pm 1$ depending on whether A is even or odd in the combined power of the momenta, then

  $$C_{AB}(t) = \langle A(0)B(t)\rangle_0 = \epsilon_A\epsilon_B\,\langle A(0)B(-t)\rangle_0 = \epsilon_A\epsilon_B\,\langle A(t)B(0)\rangle_0 = \epsilon_A\epsilon_B C_{BA}(t)\,. \tag{1.15}$$

Combined with Eq. 1.13 it follows that

$$\int_0^\infty dt\, C_{AB}(t) = 0 \quad \text{if } \epsilon_A + \epsilon_B = 0\,, \tag{1.16}$$

as any time reversed trajectory is also a legitimate trajectory of the system. The relationship can be extended to correlation functions of multiple variables, as long as the combined parity is 0.

Green-Kubo Formalism

While Onsager's regression hypothesis infers that one can calculate transport coefficients from knowledge of the equilibrium fluctuations, the specific formalism remains unclear. Here we review one way to derive the Green-Kubo formula following the notes in [37]. Consider a classical system of N particles where the dynamical state is specified by the coordinates $\mathbf{q} = (q_1, q_2, \cdots, q_N)$ and the conjugate momenta $\mathbf{p} = (p_1, p_2, \cdots, p_N)$. We are interested in some function $A(\mathbf{p}(t), \mathbf{q}(t))$ of the state of the system at time t. The system starts from an equilibrium state with the Hamiltonian $\mathcal{H}_0$ and the corresponding distribution $f_0(\mathbf{p}, \mathbf{q})$. The two quantities are related by the Liouville's equation of motion

$$\frac{\partial f_0}{\partial t} = (\mathcal{H}_0, f_0) = 0\,, \tag{1.17}$$

where the bracket denotes the Poisson bracket

$$(A, B) = \sum_i \left(\frac{\partial A}{\partial q_i}\frac{\partial B}{\partial p_i} - \frac{\partial A}{\partial p_i}\frac{\partial B}{\partial q_i} \right)\,. \tag{1.18}$$

Now at $t = 0$ consider an external perturbation $\mathcal{H}_e$ applied onto the system

$$\mathcal{H} = \mathcal{H}_0 + \mathcal{H}_e, \quad \mathcal{H}_e = -AX(t)\,, \tag{1.19}$$

where $X(t)$ is the affinity conjugate to A. This form of linear perturbation is not uncommon in physical systems, for example, if A is the electric dipole moment, then X is an electric field. If we separate the new distribution function $f(t)$ into the unperturbed part f_0 and a small perturbation Δf, the latter follows the equation of motion to the first order

$$\frac{\partial \Delta f}{\partial t} = (\mathcal{H}_0, \Delta f) - (A, f_0)X(t)\,, \tag{1.20}$$

the solution of which is

$$\Delta f(t) = -\int_{-\infty}^{t} dt' e^{i(t-t')\mathcal{L}_0}(A, f_0)X(t')\,, \tag{1.21}$$

where the Liouville's operator $i\mathcal{L}_0 g = (\mathcal{H}_0, g)$, so that $g(t) = e^{i\mathcal{L}_0 t} g$ in the unperturbed system.

The response of an arbitrary quantity can now be expressed in terms of the new distribution function. For example, the current response, which is zero in equilibrium, can be expressed as

$$\langle \Delta J(t) \rangle = \int \mathbf{dp} \int \mathbf{dq}\ J(t) \Delta f(t) = \int_0^t dt' \phi(t-t') X(t') + O(X^2)\,, \tag{1.22}$$

where ϕ is called the after-effect function, or the response function

$$\phi(t) = \int \mathbf{dp} \int \mathbf{dq}(f_0, A) J(t)\,. \tag{1.23}$$

For the canonical distribution $f_0 = e^{-\beta \mathcal{H}_0}/Z$, where $\beta = 1/k_B T$ and Z is the partition function, we have $(f_0, A) = \beta \dot{A} f_0$, thus the after-effect function becomes

$$\phi(t) = \beta \left\langle \dot{A}(0) J(t) \right\rangle_0\,. \tag{1.24}$$

Thus in Fourier components, we get a linear relationship

$$\langle J(\omega) \rangle = L_1(\omega) X(\omega)\,, \tag{1.25}$$

and the transport coefficient is given by

$$L_1(\omega) = \beta \int_0^\infty dt \exp(-i\omega t) \left\langle \dot{A}(0) J(t) \right\rangle\,. \tag{1.26}$$

Kubo's theory relies on the perturbation expansion of the state distribution function. While the formula is exceptionally elegant, the perturbation described in Eq. 1.19 is restricted to external forces. Transport coefficients associated with internal disturbances, such as temperature gradients, cannot be treated directly by Kubo's method. Due to this reason, a variety of other methods have been proposed, among them is Green's theory. The new feature supplied by Green's theory is the introduction of Brownian motion into the general theory of irreversible processes [38]. By writing down the Fokker-Planck equation for the probability distribution of physical variables, Green's work is the first generalization to previous case studies that applies to a wide range of transport coefficients, such as viscosity, thermal conductivity, and diffusion. A related formalism called the Einstein-Helfand formula can be readily derived from the Green-Kubo formula [39], using the property of the correlation function in Eq. 1.13.

While Green's theory is based on Markov process and linear response, its extension to non-Markovian and nonlinear processes has been given by Zwanzig [40]. In the Mori-Zwanzig formalism, one can write down a generalized Langevin equation for an aribitrary phase variable $A(t)$ that evolves under the equilibrium distribution function, using the technique of projection operator,

$$\frac{dA(t)}{dt} = i\Omega A(t) - \int_0^t d\tau K(\tau) A(t-\tau) + F(t)\,, \tag{1.27}$$

where K is the memory kernel, F the random force, and the frequency $i\Omega$ is an equilibrium property of the system. By a Laplace transform, one can write down the memory kernel K, which plays the role of a transport coefficient, in terms of equilibrium auto-correlation function of the phase variable.

In Table 1.1, we list the Green Kubo formulas for a few commonly used transport coefficients with the reference for their earliest derivation. The popularity of the Green-Kubo formula lies in its simplicity and practicality, while its limitation is also evident. Firstly, the Green-Kubo formula is only expressed for linear response coefficients. Secondly, Green-Kubo formula is only able to relate transport coefficients to equilibrium fluctuations. This is evident in the Mori-Zwanzig formulism, where the zero wavevector limit has to be taken in the Laplace transform, since there is no equilibrium fluctuations in the affinity at zero wavevector limit. Extending the Mori-Zwanzig formalism to the finite wavevector case is subtle [41]. Thirdly, from a practical perspective, for some low-dimension systems, it is found that the current auto-correlation function decays slow enough that its integral does not converge [42].

It is worth noting that there exists many other methods that relate transport coefficients to time-correlation functions, such as the local equilibrium theory by Mori [43], and the external reservoir theory [44]. While these theories all arrive at the same expression as the Green-Kubo formula, they aim to justify the simple form in irreversible processes as general as possible. It is perhaps important to point out that the transport coefficients are independent of the method used to establish a departure from equilibrium, at least on the level of linear response [45].

Table 1.1: Transport coefficients with corresponding Green-Kubo formula.

Transport Coefficient	**Green-Kubo Relations**[1]	**Reference**
shear viscosity	$\eta = \frac{V}{k_{\mathrm{B}}T}\int_0^\infty \langle S_{xy}(0)S_{xy}(t)\rangle\, dt$	Green [10], Kubo [46]
thermal conductivity	$\kappa = \frac{1}{Vk_{\mathrm{B}}T^2}\int_0^\infty \left\langle j_x^h(0)j_x^h(t)\right\rangle dt$	Green [10], Kubo [46]
electrical conductivity	$\sigma = \frac{1}{Vk_{\mathrm{B}}T}\int_0^\infty \langle q_x^e(0)q_x^e(t)\rangle\, dt$	Kubo [9]
interfacial friction coefficient	$\mu = \frac{A}{k_{\mathrm{B}}T}\int_0^\infty \langle f_x(0)f_x(t)\rangle\, dt$	Bocquet & Barrat [47]

Nonlinear Response Theory

Up to now, we have constrained ourselves to linear response theory. In section, we review several existing theories of nonlinear response. Kubo in his original framework also derived a perturbation expansion for the nonequilibrium phase space distribution. This is done by

[1] V: system volume, k_B: Boltzmann constant, T: temperature, S_{xy}: shear stress, j_x^h: heat flux, q_x^e: electron current, A: surface area, f_x: interfacial friction force

expanding the nonequilibrium distribution function Δf in Eq. 1.20 to higher order terms in the affinity. In a similar spirit, Yamada and Kawasaki [11] derived a closed expression for the perturbed distribution function Δf, instead of a power series expansion, using the Dyson decomposition of the Liouville propagators [48]. Unfortunately, such expressions, as well as many that followed [49–51], have been difficult to translate into easily measurable forms with clear physical interpretations. As a result, an explicit expression for computing nonequilibrium averages is still lacking.

Furthermore, the assumption that such a power series expansion exists is also questionable. Indeed, non-analytic phenomenological transport processes are found commonly in rheological systems. Such non-analyticity associated with conserved quantities is often explained by hydrodynamical theories. However, such complexities are not the main focus of this dissertation, and are often absent in simpler Markovian systems.

The simplest generalization of the Green-Kubo formula that fills in this gap is perhaps the transient time-correlation function formalism [52–54]. It gives an exact relation between the nonequilibrium ensemble average of an observable and the integral of a transient time-correlation function between the observable and the current. The full nonlinear response is embedded in the nonlinear evolution propagator of the observable. For example, in the case of a Couette flow with strain rate γ, the nonequilibrium response of an observable $A(t)$ is

$$\langle A(t)\rangle = \langle A(0)\rangle - \beta\gamma V \int_0^t ds\, \langle \Delta A(s) S_{xy}(0)\rangle \ , \tag{1.28}$$

where the system starts at an equilibrium ensemble at time $t = 0$, and the affinity is turned on afterwards. Unlike the Green-Kubo method, the transient time-correlation function has to be evaluated by performing a nonequilibrium simulation, yet the statistical uncertainty in the nonequilibrium average is often much larger than that of the direct nonequilibrium simulation [12].

1.3 Nonequilibrium Fluctuation Theorems from Stochastic Thermodynamics

Stochastic thermodynamics offers us a new tool to study generic nonequilibrium processes, of which transport is an example. Stochastic thermodynamic techniques not only establish a definition for fluxes and affinities, so that the canonical form of the entropy production in Eq. 1.4 can be justified, but also derive fluctuation theorems that hold arbitrarily far from equilibrium [13, 14, 55, 56], such as

$$\frac{P(J)}{P(-J)} = e^{\beta\sigma} \ , \tag{1.29}$$

which relates the ratio of probability of observing an arbitrary current J and its time reversal conjugate to the entropy production of the process. Unlike the previous results in classical

transport theory, these universal theorems do not rely on any near equilibrium assumptions, and thus hold for nonlinear transport regimes as well.

Many of the developments in stochastic thermodynamics are built around the large deviation function, which is a generalization of the free energy in nonequilibrium systems. It fully characterizes the fluctuations of a system, and thus its form obeys certain constraints imposed by the fluctuation theorems, such as the Gallovati-Cohen symmetry [14]. Based on the properties of the nonequilibrium large deviation function ψ_X biased on the current J, Gaspard derived multivariate fluctuation relations which relate the response of the current to mixed derivatives of the large deviation function [24],

$$\langle J \rangle_X = -\left(\frac{\partial^2 \psi_X}{\partial \lambda \partial X}\Big|_{\lambda=X=0} \right) X - \frac{1}{2}\left(\frac{\partial^3 \psi_X}{\partial \lambda \partial X^2}\Big|_{\lambda=X=0} \right) X^2 + O(X^3)\,. \tag{1.30}$$

While this relationship gives an explicit expression for transport coefficients when compared with Eq. 1.6, the evaluation of the mixed derivatives involve simulations at both different affinities and different auxiliary fields λ, which makes the computation inconvenient.

Another set of works concern modified fluctuation-dissipation theorems for nonequilibrium steady states. While nonequilibrium systems violate the fluctuation-response relation due to the lack of detailed balance, the extent of the violation can be related to the entropy dissipation [19]. This results in extended fluctuation-dissipation theorems, that acquire an additive contribution which involves the observable that is conjugate to the perturbation in the dissipation function [20, 21]. This additional piece is recognized as the time reversal dynamical activity, or frenesy [18, 22], with which we can write down higher order response of the current [57, 58],

$$\langle J \rangle_X = \langle J S_0' \rangle_0 \, X - \langle J S_0' D_0' \rangle_0 \, X^2 + O(X^3)\,, \tag{1.31}$$

where S and D are the time anti-symmetric and time symmetric part of the path action, and S_0', D_0' are their first derivatives evaluated at $X = 0$. This insight, that the higher order response is not only governed by dissipation, but also depends explicitly on the dynamical details of the system, is crucial to understanding nonlinear response behaviors. In the next chapter, we will build on this insight to derive a large deviation formalism for nonlinear transport coefficients.

Chapter 2

Transport Coefficients from Large Deviation Functions

2.1 Introduction to Large Deviation Functions

Large deviation theory is concerned with the exponential decay of probabilities of large fluctuations in stochastic systems. These probabilities are important in many fields of study, including statistics, finance, and engineering, as they yield valuable information about rare events. In the recent decades, physicists have found interesting connections between large deviation theory and statistical mechanics - the theories of equilibrium statistical mechanics can be rephrased using the language of large deviation theory, where large deviation functions (LDFs) play the role of free energy, an important concept in molecular simulations of chemical and biological systems. When it comes to nonequilibrium statistical mechanics, an area which lacks a universal physical theory, large deviation theory underlies much of the recent progress. They contain information on the stability and response of systems driven into nonequilibrium steady states.

As with equilibrium free energies, evaluating large deviation functions numerically for all but the simplest systems is difficult because by construction they depend on exponentially rare events. One of the first methods designed to compute the large deviation function, known as the cloning algorithm, involves a large number of walkers evolved in parallel, and achieves the desired tilted probability distribution by selectively branching and killing the walkers [59]. As the desired distribution deviates further from the original dynamics, it becomes more difficult to harvest useful trajectories, and high correlation among walkers introduce bias in the estimate of the large deviation functions [60]. Such population based methods are not only computationally expensive, but also suffer from sampling deficiencies that make application to high-dimensional systems difficult.

To mitigate these problems, a growing amount of work is exploring auxiliary dynamics that can push the trajectories to the rare fluctuations that contribute most to the large deviation function. For Markovian dynamics, it has been shown that a Markov process

conditioned on rare events involving time integrated random variables can be described in the long time limit by an effective Markov process, called the driven process [61]. Such an optimal auxiliary process always exists and can be constructed by a canonical transformation known as the Doob's transform. What's more, this driven process can be interpreted as an optimal stochastic control process minimizing a cost function related to large deviation functions [62]. The establishment of such a variational principle allows us to design optimization programs to solve for the large deviation function [63].

In what follows, we first review the large deviation principle in the context of chemical physics, and introduce the large deviation function. Afterwards, we review a few numerical methods developed to compute the large deviation function, including the direct diagonalization method, the cloning algorithm, and a variational algorithm that has been developed recently. While the materials in this section are only meant to provide the prerequisite for the rest of the chapter, a more complete review of the large deviation function and its computation can be found in [26].

Large Deviation Principle

We consider diffusion processes described by the stochastic differential equation

$$d\tilde{x}_t = F(\tilde{x}_t)dt + \sigma(\tilde{x}_t) \circ dw_t \,, \tag{2.1}$$

where the state of the system $\tilde{x}_t \in R^d$ is determined by the drift F: $R^d \to R^d$, the diffusion field σ: $R^d \to R^d$, and a Brownian motion $w_t \in R$. This is often referred to as the overdamped Langevin equation in the chemical physics literature, and is used to describe the motion of particles in implicit solvents. For such a system, we are interested in time integrated observables up to time t_{N}that have the general form

$$A(t_{\mathrm{N}}) = \frac{1}{t_{\mathrm{N}}} \int_0^{t_{\mathrm{N}}} f(\tilde{x}_t)dt + g(\tilde{x}_t) \circ d\tilde{x}_t \,, \tag{2.2}$$

where f is a scalar function, g is a vector function, and $\circ$ denotes the Stratonovich product. In many physical processes, the probability distribution of $A(t_{\mathrm{N}})$ satisfies a large deviation principle

$$P[A(t_{\mathrm{N}}) = a] \approx e^{-t_{\mathrm{N}} I(a)} \,, \tag{2.3}$$

in the limit $t_{\mathrm{N}} \to \infty$ with subexponential corrections in t_{N}. This scaling result implies that the probability of $A(t_{\mathrm{N}})$ decays exponentially with t_{N}, except at the global minimum a^* of the rate function $I(a)$ where it concentrates with t_{N}. Note that we will assume that the rate function $I(a)$ is convex and has a unique global minimum.

To characterize the fluctuations in $A(t_{\mathrm{N}})$, we define the large deviation function, which is a scaled cumulant generating function of $A(t_{\mathrm{N}})$,

$$\psi(\lambda) = \lim_{t_{\mathrm{N}} \to \infty} \frac{1}{t_{\mathrm{N}}} \ln \left\langle e^{-\lambda t_{\mathrm{N}} A(t_{\mathrm{N}})} \right\rangle_F \,. \tag{2.4}$$

Here, the average $\langle \cdots \rangle$ is taken within an ensemble of paths of length t_{N}, denoted as a vector of all the configurations visited over that time, or $\tilde{x}(t_{\mathrm{N}}) = \{\tilde{x}_0, \tilde{x}_1, \cdots, \tilde{x}_{t_{\mathrm{N}}}\}$. The probability of observing such a path is given by

$$P_F[\tilde{x}(t_{\mathrm{N}})] = \rho[\tilde{x}_0] \prod_{i=1}^{t_{\mathrm{N}}} \omega[\tilde{x}_{i-1} \to \tilde{x}_i] \,, \tag{2.5}$$

where $\rho[\tilde{x}_0]$ represents the distribution of initial conditions, and ω are the transition probabilities between time adjacent configurations as described in Eq. 2.1. Given a convex rate function, the large deviation function is related to the rate function by a Legendre-Fenchel transform

$$I(a) = \inf_{\lambda} [\lambda a + \psi(\lambda)] \,. \tag{2.6}$$

It follows from the property of cumulant generating function that the fluctuations of $A(t_{\mathrm{N}})$ are simply given by the derivatives

$$\frac{d\psi(\lambda)}{d\lambda} = -\left\langle A \right\rangle_F \,, \quad \frac{d^2\psi(\lambda)}{d\lambda^2} = t_{\mathrm{N}} \left\langle (\delta A)^2 \right\rangle_F \,, \tag{2.7}$$

where $\delta A = A - \langle A \rangle_F$.

Direct Diagonalization Method

According to its definition, the large deviation function can be seen as a normalization factor of the tilted ensemble,

$$P_\lambda[\tilde{x}(t_{\mathrm{N}})] = \frac{P_F[\tilde{x}(t_{\mathrm{N}})] e^{-\lambda t_{\mathrm{N}} A(t_{\mathrm{N}})}}{\left\langle e^{-\lambda t_{\mathrm{N}} A(t_{\mathrm{N}})} \right\rangle_F} \,, \tag{2.8}$$

where the original path probability $P_F[\tilde{x}(t_{\mathrm{N}})]$ is tilted exponentially. A straightforward way to compute the large deviation function is then to construct a non-conservative process associated with the tilted path measure. According to the Feynman-Kac formula, for the diffusion process in Eq. 2.1, such a process can be generated by the tilted operator [61]

$$\mathcal{L}_\lambda = F \cdot (\nabla - \lambda g) + \frac{1}{2} (\nabla - \lambda g) D (\nabla - \lambda g) - \lambda f \,, \tag{2.9}$$

where D is the covariance matrix involving the components of the diffusion field σ. The large deviation function is then the real dominant eigenvalue of the tilted operator

$$\mathcal{L}_\lambda r_\lambda = \psi(\lambda) r_\lambda \,, \tag{2.10}$$

with its associated right eigenvector r_λ. For those systems where the tilted operator can be derived exactly, computing the large deviation function is equivalent to an eigenvalue problem, which can be solved by numerical diagonalization. This method, however, only applies to simple systems with limited degrees of freedom.

Cloning Algorithm

Alternatively, the normalization factor in Eq. 2.8 can be computed from a diffusion Monte Carlo algorithm, known as the cloning algorithm [59, 64], where an ensemble of trajectories are integrated in parallel. Each individual trajectory is known as a walker, and collectively the walkers undergo a population dynamics whereby short trajectory segments are augmented with a branching process that results in walkers being pruned or duplicated in proportion to a weight. This algorithm has been used extensively in the study of driven lattice gases [28] and models of glasses [65, 66].

Without loss of generality, if we choose the observable of interest to be the current J, then we find a familiar relationship between biased ensembles

$$\ln p_\lambda(J) = \ln p(J) - \lambda t_{\rm N} J - t_{\rm N}\psi(\lambda)\,, \tag{2.11}$$

where $p_\lambda(J) = \langle \delta(J - J(t_{\rm N}))\rangle_\lambda$ is the probability of observing a given value of the current J in the tilted ensemble, and $p(J)$ is that in the unbiased ensemble. This demonstrates that $\psi(\lambda)$ is computable as a change in normalization through histogram reweighting [67].

In order to arrive at a robust estimate for $\psi(\lambda)$, the two distributions, $p_\lambda(J)$ and $p(J)$, must have significant overlap. However, for large systems or long observation times, each distribution narrows, and sampling $p_\lambda(J)$ by brute force is exponentially difficult. To evaluate the large deviation function, the cloning algorithm samples $P_\lambda[\tilde{x}(t_{\rm N})]$ by noting that it can be expanded to

$$P_\lambda[\tilde{x}(t_{\rm N})] \propto \rho[\tilde{x}_0] \prod_{i=1}^{t_{\rm N}/\delta t} \tilde{\omega}[\tilde{x}_{i-1} \to \tilde{x}_i] e^{-\lambda \delta t j[\tilde{x}_i]}\,, \tag{2.12}$$

where we have discretized the integral for J with timestep δt, and $\tilde{\omega}[\cdots]$ are the corresponding transition probabilities per δt. The argument of the product is the transition probability times a bias factor that is local in time. This combination of terms cannot be lumped together into a physical dynamics, as it is unnormalized. However, it can be interpreted as a population dynamics where the non-conservative part proportional to the bias is represented by adding and removing walkers. In particular, in the cloning algorithm, trajectories are propagated in two steps. First, $N_{\rm w}$ walkers are integrated according to the normalized dynamics specified by $\tilde{\omega}[\tilde{x}_{i-1} \to \tilde{x}_i]$ for a trajectory of length $n\delta t$. Over this time, a bias is accumulated according to

$$W_i(t, n\delta t) = \exp\left[-\lambda \delta t \sum_{j=1}^{n} j[\tilde{x}_{t+j\delta t}]\right]\,, \tag{2.13}$$

where, due to the multiplicative structure of the Markov chain, the bias is simply summed in the exponential. After the trajectory integration, $n_i(t)$ identical copies of the ith trajectory are generated in proportion to $W_i(t, n\delta t)$,

$$n_i(t) = \left\lfloor N_{\rm w} \frac{W_i(t, n\delta t)}{\sum_{j=1}^{N_{\rm w}} W_j(t, n\delta t)} + \xi \right\rfloor\,, \tag{2.14}$$

where ξ is a uniform random number between 0 and 1 and $\lfloor \dots \rfloor$ is the floor function. This process will result in a different number of walkers, and thus each walker in the new population is copied or deleted uniformly until N_{w} are left. With this algorithm, the large deviation function can be evaluated after each branching step as the deviation of the normalization

$$\psi^t(\lambda) = \ln \frac{1}{t_{\mathrm{N}}} \sum_{i=1}^{t_{\mathrm{N}}} W_i(t, n\delta t)\,, \tag{2.15}$$

which is an exponential average over the bias factors of each walker. In the limit of a large number of walkers, this estimate is unbiased [68]. The local estimate can be improved by averaging over the observation time

$$\psi(\lambda) = \frac{1}{t_{\mathrm{N}}} \sum_{t=1}^{t_{\mathrm{N}}/(n\delta t)} \psi^t(\lambda)\,, \tag{2.16}$$

which, upon repeated cycles of integration and population dynamics, yields a statistically converged estimate of $\psi(\lambda)$. Alternatively, $\psi(\lambda)$ can be computed from histogram reweighting using Eq. 2.11 from the distribution of J generated from each walker.

One of the key factors in determining the statistical efficiency of the cloning algorithm is the number of independent trajectories sampled over t_{N}. In all the calculations shown in this chapter, walker numbers are chosen individually for each parameter so that at the end of the simulation, the number of independent walkers which have not been replaced is at least on the order of 10^2.

Driven Process

From a sampling point of view, to compute the large deviation function for larger λ's, we have to sample exponentially rare events, which is computationally costly. Naturally, one can use importance sampling techniques [69–72], where an auxiliary dynamics is used to guide the original dynamics, given proper reweighting is compensated. While arbitrary guiding distribution can be used, particular ones that greatly improve the efficiency of the algorithm have been explored. Indeed, for Markovian dynamics, it has been shown that a Markov process conditioned on rare events involving time integrated random variables can be described in the long time limit by an effective Markov process, called the driven process [61]. For the diffusion process in Eq. 2.1, consider a modified diffusion process

$$d\tilde{x}_t = u(\tilde{x}_t)dt + \sigma(\tilde{x}_t) \circ dw_t\,, \tag{2.17}$$

with the path probability $P_u[\tilde{x}(t_{\mathrm{N}})]$. It can be shown by Doob's transform that the process with the modified force

$$u = F + D(-\lambda g + \nabla \ln r_\lambda)\,, \tag{2.18}$$

where r_λ is defined in Eq. 2.10, satisfies the equivalence condition

$$\lim_{t_{\rm N}\to\infty} \frac{1}{t_{\rm N}} \ln \frac{P_u[\tilde{x}(t_{\rm N})]}{P_\lambda[\tilde{x}(t_{\rm N})]} = 0\,. \tag{2.19}$$

As elegant as this theoretical result is, to compute r_λ involves solving a eigenvalue problem, which is not practical for many-body systems. Therefore, driven forces u has to be solved or approximated by numerical simulations.

Variational Representation of Large Deviation Functions

There are several ways to arrive at the variational representation of large deviation functions, including the contraction principle and stochastic optimal control. Here we follow the one that uses the notion of relative entropy. Recall that, given two probability measures P and Q, the relative entropy of P with respect to Q is defined as

$$S(P||Q) = \int dP(x) \ln \frac{P(x)}{Q(x)}\,. \tag{2.20}$$

This is also known as the Kullback-Leibler (KL) distance between probability measures, and is non-negative with equality if and only if $P = Q$. The rate function can then be expressed by

$$I(a) = \lim_{t_{\rm N}\to\infty} \inf \frac{1}{t_{\rm N}} S(P_u||P_F), \quad \text{s.t} \quad \langle A(t_{\rm N})\rangle_u = a\,, \tag{2.21}$$

where for the diffusion processes we are considering, the KL distance is easy to write down explicitly,

$$S(P_u||P_F) = \left\langle \frac{1}{2}[u(\tilde{x}) - F(\tilde{x})]D^{-1}[u(\tilde{x}) - F(\tilde{x})] \right\rangle_u\,. \tag{2.22}$$

Physically this shows that the driven process is the Markov process closest to the original process, in the sense of relative entropy, that satisfies the constraint $\langle A(t_{\rm N})\rangle_u = a$. The dual representation of this constrained problem defines the large deviation function

$$\psi(\lambda) = \lim_{t_{\rm N}\to\infty} \sup_u \{-\lambda \langle A(t_{\rm N})\rangle_u - \frac{1}{t_{\rm N}} S(P_u||P_F)\}\,. \tag{2.23}$$

This dual problem has the same solution as the original problem for convex rate functions, which follows from properties of Legendre-Fenchel transforms. Turning the computation of the large deviatioon function into an optimization problem gives us access to numerous optimization techniques that greatly improve the numerical efficiency compared to the cloning algorithm.

2.2 Derivation of Transport Coefficients [1]

We are now ready to derive transport coefficients using the large deviation formalism. We are interested in stochastic systems maintained in nonequilibrium steady states by an affinity X, which can either be an external force, or contacts with different thermodynamic reservoirs. We assume that the macroscopic current in Eq. 1.6 coincides with the nonequilibrium ensemble average and can be written as a polynomial expansion,

$$J = L_0 + L_1 X + L_2 X^2 + L_3 X^3 + O(X^4)\,, \tag{2.24}$$

where L_0 is the current in the absence of the affinity, which should vanish for equilibrium systems. L_1 is known as the linear transport coefficient, and all the higher order coefficients $L_2, L_3, \cdots$, are nonlinear transport coefficients. The generality of this polynomial expansion will be discussed further towards the end of this chapter. Given this assumption, in this section we derive an explicit expression for these transport coefficients. Although we will restrict ourselves to a single type of affinity, the generalization to multiple ones is straightforward.

Nonlinear Coefficients from LDFs

We adopt the same notation $\tilde{x}$ for a continuous stochastic trajectory of length $t_{\rm N}$ as in Eq. 2.5, where $\tilde{x}_t = \{\boldsymbol{r}(t), \boldsymbol{v}(t)\}$ is the specific configuration of the system at time t, with coordinates $\boldsymbol{r}(t)$ and velocities $\boldsymbol{v}(t)$. We define a relative stochastic action $\beta\mathcal{U}[\tilde{x}]$ by a ratio of the probability of observing a specific path with and without the affinity,

$$\frac{P_X[\tilde{x}]}{P_0[\tilde{x}]} = e^{\beta\mathcal{U}[\tilde{x}]}\,, \tag{2.25}$$

where the subscripts denote the value of the affinity; $\beta = 1/k_B T$ where T is the temperature, k_B is Boltzmann constant that will be set to 1 for the rest of the chapter.

We next decompose the total relative path action into two parts according to their time reversal symmetry,

$$\mathcal{U}[\tilde{x}] = \mathcal{A}[\tilde{x}] + \mathcal{S}[\tilde{x}]\,, \tag{2.26}$$

with $\mathcal{A}[\tilde{x}]$ denoting the asymmetric part, and $\mathcal{S}[\tilde{x}]$ the symmetric part. Specifically, if we define an operator $\mathbb{T}$ which returns the time reversed counterpart of a path $\tilde{x}$ so that $\mathbb{T}\tilde{x}_t = \{\boldsymbol{r}(t_{\rm N} - t), -\boldsymbol{v}(t_{\rm N} - t)\}$, it follows that $\mathcal{A}[\mathbb{T}\tilde{x}] = -\mathcal{A}[\tilde{x}]$, $\mathcal{S}[\mathbb{T}\tilde{x}] = \mathcal{S}[\tilde{x}]$. The time asymmetric part is the entropy production of the irreversible process, which can be written as the product of the affinity and the conjugated time extensive current [8],

$$\mathcal{A}[\tilde{x}] = t_{\rm N} J X, \;\; J[\tilde{x}] = \frac{1}{t_{\rm N}} \int_0^{t_{\rm N}} dt \;\; j(\tilde{x}_t)\,. \tag{2.27}$$

[1] Most of the content of this section was originally written by the author for the following publication: C. Y. Gao and D. T. Limmer, "Nonlinear Transport Coefficients from Large Deviation Functions", *The Journal of Chemical Physics* **2019**, 151 (1).

The symmetric part is often referred to as the activity [73],

$$\mathcal{S}[\tilde{x}] = \sum_{i=1}^{p} t_{\mathrm{N}} Q_i X^i, \;\; Q_i[\tilde{x}] = \frac{1}{t_{\mathrm{N}}} \int_0^{t_{\mathrm{N}}} dt \;\; q_i(\tilde{x}_t) \,. \tag{2.28}$$

The number of terms p depends on system details, though for Gaussian processes it is often only 1. For details, the derivation of J and Q_i's for a general underdamped Langevin system will be shown later in this section.

Next, we construct a LDF of the form

$$\psi_X(\boldsymbol{\lambda}) = \lim_{t_{\mathrm{N}} \to \infty} \frac{1}{t_{\mathrm{N}}} \ln \left\langle e^{-(\lambda_J t_{\mathrm{N}} J + \sum_i \lambda_{Q_i} t_{\mathrm{N}} Q_i)} \right\rangle_X \,, \tag{2.29}$$

where $\boldsymbol{\lambda} = (\lambda_J, \lambda_{Q_1}, \lambda_{Q_2}, \cdots)$, i.e. each dynamical variable is exponentially biased by a conjugated λ. The bracket denotes path ensemble average with respect to the path probability density $P_X[\tilde{x}]$. It follows by definition that

$$\psi_X(\lambda_J, \lambda_{Q_1}, \lambda_{Q_2}, \cdots) = \psi_0(\lambda_J - \beta X, \lambda_{Q_1} - \beta X, \lambda_{Q_2} - \beta X^2, \cdots) \,, \tag{2.30}$$

which provides a symmetry that links the statistical bias $\boldsymbol{\lambda}$ to the physical driving X. This relation is distinct from a fluctuation theorem and encodes the fact that X is not a conjugate variable to J, but rather a linear combination of J and the Q_i's. The derivatives of the cumulant generating function provide information about the self and cross correlation functions of J and the Q_i's. For example, the nonequilibrium average current is given by the first derivative

$$\langle J \rangle_X = -\frac{\partial \psi_X(\boldsymbol{\lambda})}{\partial \lambda_J}\Big|_{\boldsymbol{\lambda}=\mathbf{0}} = -\frac{\partial \psi_0(\boldsymbol{\lambda})}{\partial \lambda_J}\Big|_{\lambda_J = -\beta X, \lambda_{Q_i} = -\beta X^i} \,. \tag{2.31}$$

Expanding $\psi_0(\boldsymbol{\lambda})$ assuming βX is small,

$$\begin{aligned} \langle J \rangle_X = \langle J \rangle_0 &+ \beta t_{\mathrm{N}} \left[\left\langle (\delta J)^2 \right\rangle_0 + \langle \delta J \delta Q_1 \rangle_0 \right] X \\ &+ \frac{\beta^2 t_{\mathrm{N}}^2}{2} \left[\left\langle (\delta J)^3 \right\rangle_0 + \left\langle \delta J (\delta Q_1)^2 \right\rangle_0 + 2 \left\langle (\delta J)^2 \delta Q_1 \right\rangle_0 + \frac{2}{\beta t_{\mathrm{N}}} \langle \delta J \delta Q_2 \rangle_0 \right] X^2 + \cdots \,, \end{aligned} \tag{2.32}$$

we find a microscopic relation between the average current and affinity, where for brevity, we have only written down explicitly terms up to $O(X^2)$. The notation $\langle A_1 A_2 \cdots A_n \rangle = t_{\mathrm{N}}^{-n} \int_0^{t_{\mathrm{N}}} d\mathbf{t}^n \, \langle a_1(\tilde{x}_{t_1}) a_2(\tilde{x}_{t_2}) \cdots a_n(\tilde{x}_{t_{\mathrm{N}}}) \rangle$ and $\delta A = A - \langle A \rangle_0$ are adopted throughout. By comparing with Eq. 2.24, and assuming the time averaged current is equal to the macroscopic current, the expansion in Eq. 2.32 provides explicit expressions for arbitrarily high order transport coefficients in terms of multi-time correlation functions in the absence of the affinity, which can be computed from $\psi_0(\boldsymbol{\lambda})$. While multi-time correlation functions are in general difficult to converge by direct evaluation, $\psi_0(\boldsymbol{\lambda})$ can be computed efficiently using importance sampling methods, as reviewed in Section 2.1.

To highlight the novelty of our method, we discuss how our expression is different from a few previous results in the literature. Firstly, our result is intimately related to work by Maes

et al [57, 58], though our current expression Eq. 2.32 is different beyond the third order. This stems from the fact that the current is derived in terms of a cumulant expansion instead of a moment expansion, as seen clearly in Eq. 2.32, and from rewriting Eq. 2.31,

$$\langle J \rangle_X = \frac{\langle J e^{\beta \mathcal{U}} \rangle_0}{\langle e^{\beta \mathcal{U}} \rangle_0}. \tag{2.33}$$

The cumulant expansion ensures better convergence for the transport coefficients. Compared with the expression in Eq. 1.31, we have explicitly renormalized the nonequilibrium distribution function here, which is similar to the treatment in the renormalized form of the Kawasaki distribution function [74]. When the reference state is not in equilibrium, the renormalization is absolutely necessary in numerically computing the ensemble average of an observable when $t_{\rm N}$ is longer than the Lyapunov time for the system. Otherwise, the variance in the exponential term will grow exponentially in time, regardless of the accuracy of the simulation algorithm.

Secondly, our method is distinct from the multivariate fluctuation relations in Eq. 1.30 that have been derived by constructing the LDF of only current observables [24], where transport coefficients are expressed as mixed derivatives of both λ's and the affinities. Here, by introducing the time symmetric observables Q_i's, the knowledge of the equilibrium function $\psi_0(\boldsymbol{\lambda})$ completely determines the current-affinity relationship.

Decomposing the total action by time reversal symmetry enables us to greatly simplify Eq. 2.32. If the reference system without the affinity is in equilibrium, then it obeys microscopic time reversibility $P_0[\mathbb{T}\tilde{x}] = P_0[\tilde{x}]$. It follows that the time reversal odd terms, such as the average current $\langle J \rangle_0$, and terms like $\langle J Q_i \rangle_0$, $\langle J Q_i^2 \rangle_0$ and $\langle J^3 \rangle_0$, will vanish. This reduces Eq. 2.32 to

$$\langle J \rangle_X = \beta t_{\rm N} \langle J^2 \rangle_0 X + \beta^2 t_{\rm N}^2 \langle J^2 Q_1 \rangle_0 X^2 + O(X^3)\,. \tag{2.34}$$

Note that the linear response reduces to the normal fluctuation-dissipation theorem, while higher order responses are described by higher order correlations between J and Q_i's. These correlation functions are given by derivatives of $\psi_0(\boldsymbol{\lambda})$. Specifically, the linear and first nonlinear transport coefficients are

$$L_1 = \beta \frac{\partial^2 \psi_0}{\partial \lambda_J^2}\Big|_{\boldsymbol{\lambda}=\mathbf{0}}, \quad L_2 = -\beta^2 \frac{\partial^3 \psi_0}{\partial \lambda_J^2 \partial \lambda_{Q_1}}\Big|_{\boldsymbol{\lambda}=\mathbf{0}}. \tag{2.35}$$

Further simplifications can be made if the system exhibits certain spatial symmetries so that the dynamics is unchanged upon inverting the coordinates along a specific axis.

While transport coefficients can also be computed directly through nonequilibium simulation methods, we note that by evaluating them from equilibrium fluctuations, our method is less sensitive to finite size effects arising from boundary conditions and altered equations of motion required to simulate a driven system. In addition, while direct simulation measures the nonequilibrium response at a finite value of the affinity, our method generically generates

the response for a continuum of affinities. Indeed, if one is specifically interested in the current response at a finite field X, it suffices to measure the local curvature of ψ_X at $\boldsymbol{\lambda} = \mathbf{0}$ by computing the equilibrium large deviation function ψ_0 around $\lambda_J = \beta X, \lambda_{Q_i} = \beta X^i$ according to Eq. 2.30, where we have established a direct connection between the statistical biased and nonequilibrium ensembles.

Example: Overdamped Langevin System

Consider a system with N degrees of freedom interacting through potential $V(\boldsymbol{r})$ at temperature T. Each degree of freedom i evolves under the underdamped Langevin equation

$$m_i \dot{v}_i = -m_i \gamma v_i - \frac{dV(\boldsymbol{r})}{dr_i} + F + \eta_i, \tag{2.36}$$

where m_i is the mass, γ is the friction coefficient, F is a constant force, and η_i's are Gaussian noise satisfying $\langle \eta_i(0)\eta_j(t)\rangle = 2m_i\gamma k_B T \delta(t)\delta_{ij}$. The probability of observing a given trajectory can be written in the Onsager-Machlup form [34]

$$P_F[\tilde{x}] \propto \exp\left[-\int dt \sum_{i=1}^{N} \frac{(m_i \dot{v}_i + m_i\gamma v_i + dV(\boldsymbol{r})/dr_i - F)^2}{4m_i\gamma k_B T} \right]. \tag{2.37}$$

The relative stochastic action can be derived from the ratio of path probability with and without F,

$$\mathcal{U}[\tilde{x}] = -\sum_{i=1}^{N} \frac{-(2m_i\dot{v}_i + 2m_i\gamma v_i + 2dV(\boldsymbol{r})/dr_i)F + F^2}{4m_i\gamma}. \tag{2.38}$$

As only the velocities are asymmetric upon time reversal, we identify the time asymmetric and symmetric parts as

$$\begin{aligned} \mathcal{A}[\tilde{x}] &= \sum_{i=1}^{N} \frac{v_i F}{2}, \\ \mathcal{S}[\tilde{x}] &= \sum_{i=1}^{N} \frac{(m_i\dot{v}_i + dV(\boldsymbol{r})/dr_i)F}{2m_i\gamma} - \sum_{i=1}^{N} \frac{F^2}{4m_i\gamma}. \end{aligned} \tag{2.39}$$

As seen, the time symmetric part has a part proportional to F, and a part proportional to F^2; in other words, $\mathcal{S}[\tilde{x}] = \sum_{i=1}^{p} t_{\mathrm{N}} Q_i X^i$ where $p = 2$. Defining the affinity $X = F/2$, we arrive at the expressions of the dynamical variables,

$$j(\tilde{x}_t) = \sum_{i=1}^{N} v_i, \quad q_1(\tilde{x}_t) = \sum_{i=1}^{N} \frac{m_i\dot{v}_i + dV(\boldsymbol{r})/dr_i}{m_i\gamma}. \tag{2.40}$$

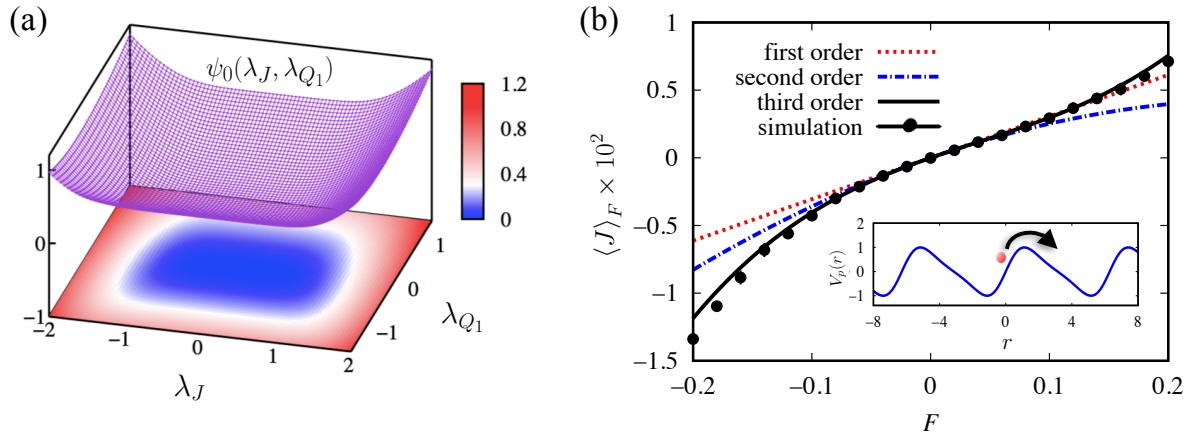

Figure 2.1: Computation of nonlinear transport coefficients of a Brownian ratchet. (a) 2D surface of the LDF, with a contour plot projected onto the $\lambda_J - \lambda_{Q_1}$ plane, from which the coefficients are derived. (b) Comparison between nonequilibrium simulation results (black dots) and theoretical approximations for the current up to first (dotted red), second (dotted dashed blue), and third (solid black) order. (*Inset*) The potential landscape of the Brownian ratchet.

As before, $q_2(\tilde{x}_t) = -\sum_{i=1}^{N} 1/m_i\gamma$ is a constant independent of the dynamics. Therefore, the expression for nonequilibrium current can be written in a closed form

$$\langle J \rangle_X = \sum_{n=1}^{\infty} \frac{(\beta t_{\mathrm{N}} X)^{n-1}}{n!} \sum_{i+j=n} i C_n^i \kappa_{i,j}^n \,, \tag{2.41}$$

where the second sum is taken over all combinations of nonnegative indices i, j such that $i + j = n$. $\kappa_{i,j}^n$ denotes the n-th order cumulant, with the first few terms:

$$\begin{aligned}
&\kappa_{1,0}^1 = \langle J \rangle_0 \,, \kappa_{0,1}^1 = \langle Q_1 \rangle_0 \,, \\
&\kappa_{2,0}^2 = \left\langle (\delta J)^2 \right\rangle_0 \,, \kappa_{1,1}^2 = \langle \delta J \delta Q_1 \rangle_0 \,, \kappa_{0,2}^2 = \left\langle (\delta Q_1)^2 \right\rangle_0 \,, \\
&\kappa_{3,0}^3 = \left\langle (\delta J)^3 \right\rangle_0 \,, \kappa_{2,1}^3 = \left\langle (\delta J)^2 \delta Q_1 \right\rangle_0 \,, \kappa_{1,2}^3 = \left\langle \delta J (\delta Q_1)^2 \right\rangle_0 \,, \\
&\kappa_{0,3}^3 = \left\langle (\delta Q_1)^3 \right\rangle_0 \,, \\
&\cdots
\end{aligned} \tag{2.42}$$

Higher Order Response: Brownian Ratchet

To validate our method, we consider a single Brownian particle moving on a one-dimensional asymmetric potential landscape $V_p(r) = \sin(r/l + \sin(r/l)/2)$. This is a simplest continuous model that exhibits an asymmetric response of the particle's displacement to an additional constant force. The dynamics of the particle with unit mass are described by the overdamped

Langevin equation

$$\gamma\dot{r} = -\frac{dV_p(r)}{dr} + F + \eta\,. \tag{2.43}$$

where F is a constant force, γ is the friction and η is the white noise satisfying $\langle\eta(t)\rangle = 0, \langle\eta(0)\eta(t)\rangle = 2\gamma\delta(t)/\beta$. We set γ and l to 1, to define a reduced unit system and take $\beta = 1/0.3$. Considering the mobility of the particle in response to the affinity $X = F/2$, the dynamical variables take the form

$$j(\tilde{x}_t) = \dot{r}(t),\;\; q_1(\tilde{x}_t) = \gamma^{-1}\frac{dV_p}{dr}(t)\,. \tag{2.44}$$

Here, the time symmetric part is characterized by the force exerted onto the particle by the ratchet potential. There is an additional second order term $q_2(\tilde{x}_t)$, which is a constant and does not enter into the expression for the current. Expanding Eq. 2.32 up to the third order, we arrive at an expression for the integrated nonequilibrium current, or displacement,

$$\begin{aligned}\langle J\rangle_F = {} & \beta t_{\rm N}\left\langle J^2\right\rangle_0\frac{F}{2} + \beta^2 t_{\rm N}^2\left\langle J^2Q_1\right\rangle_0\frac{F^2}{4} \\ & + \beta^3 t_{\rm N}^3\left[\frac{1}{6}(\left\langle J^4\right\rangle_0 - 3\left\langle J^2\right\rangle_0^2) + \frac{1}{2}(\left\langle J^2Q_1^2\right\rangle_0 - \left\langle J^2\right\rangle_0\left\langle Q_1^2\right\rangle_0)\right]\frac{F^3}{8} + O(F^4)\,.\end{aligned} \tag{2.45}$$

It is worth noting that the higher order responses are described not only by the current fluctuations, but also the correlations between current and force fluctuations. If the potential is symmetric, the second order term will vanish due to inversion symmetry. It is the asymmetry in the ratchet potential, and as a consequence, the asymmetry in the forces, that gives rise to the even order terms. Specifically, the correlation between the squared current and the force dictates the size of the rectification of the ratchet.

In this simple case, the LDF $\psi_0(\boldsymbol{\lambda})$ can be computed numerically exactly by the direct diagonalization method, where the tilted generator is

$$L_{\boldsymbol{\lambda}} = -\frac{\partial V_p}{\partial x}\left(\frac{\partial}{\partial x} - \lambda_J\right) + T\left(\frac{\partial}{\partial x} - \lambda_J\right)^2 - \lambda_{Q_1}\frac{\partial V_p}{\partial x}\,, \tag{2.46}$$

the largest eigenvalue of which is the LDF. To solve for the eigenvalues, we construct the tilted operator with a normalized Fourier basis set $\exp(ikx)$ where $k \in [-15, 15]$ and is an integer. The 2D surface of $\psi_0(\boldsymbol{\lambda})$ is shown in Fig. 2.1(a). The obvious deviation from the normal distribution, especially the asymmetry in the λ_{Q_1} direction, leads to the observed nonlinear behavior of $\langle J\rangle_F$. The correlation functions appearing in the average current are computed from numerical derivatives of ψ_0 as in Eq. 2.35, yielding $t_{\rm N}\left\langle J^2\right\rangle_0 = 0.0184$, $t_{\rm N}^2\left\langle J^2Q_1\right\rangle_0 = -0.0194$, $t_{\rm N}^3(\left\langle J^4\right\rangle_0 - 3\left\langle J^2\right\rangle_0^2) = 0.712$, and $t_{\rm N}^3(\left\langle J^2Q_1^2\right\rangle_0 - \left\langle J^2\right\rangle_0\left\langle Q_1^2\right\rangle_0) = -0.033$. Fitting errors in the coefficients are negligible. The nonequilibrium simulation results are obtained by integrating the equation of motion using a second-order Runge-Kutta algorithm [75] with a time step $h = 10^{-3}$. Numerical results shown are averaged over 10^3 realizations with a total observation time $t_{\rm N} = 10^3$. In Fig. 2.1(b), we compare direct nonequilibrium

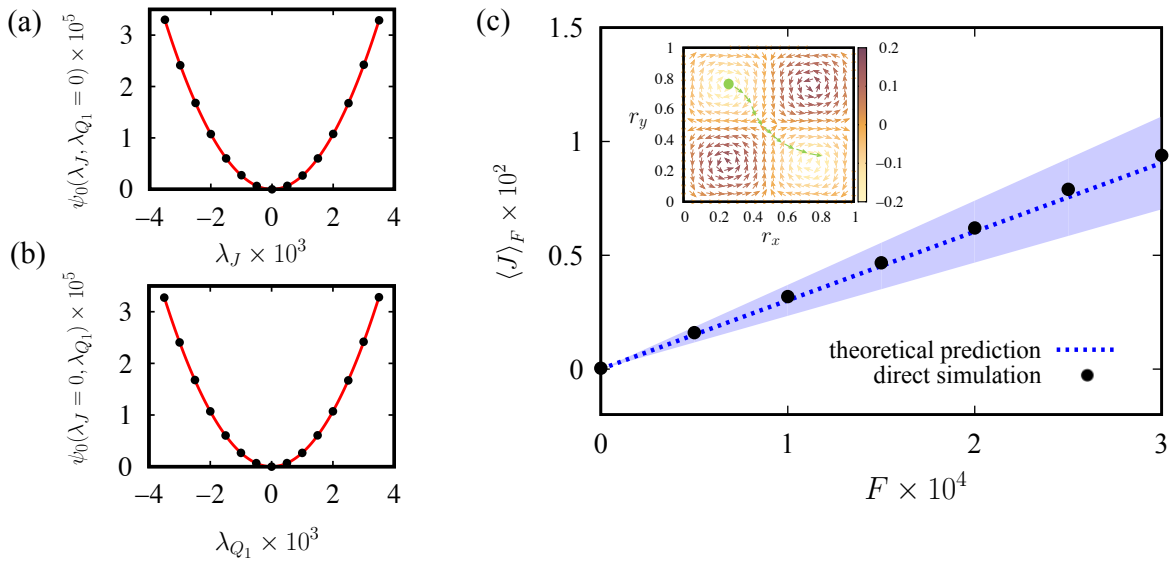

Figure 2.2: Linear response of a tracer particle in a hydrodynamic flow. (a) LDFs as a function of λ_J while fixing $\lambda_{Q_1} = 0$. Red curves are quadratic fits. (b) LDFs as a function of λ_{Q_1} while fixing $\lambda_J = 0$. (c) A comparison between direct nonequilibrium simulation results and the predicted response. Shaded area is the statistical error of the theoretically predicted response. The standard error in the direct simulation is smaller than the size of the dots. (*Inset*) The flow field and a schematic trajectory of the tracer. Orange arrows illustrate the underlying velocity field and colors map the value of the stream function.

simulation results with our theoretical predictions, which improve as we include higher order terms. It is worth noting that in this case, as the large deviation function can be solved conveniently by matrix diagonalization, the computational efficiency of our method is far superior compared to direct simulation, which requires sampling of the nonequilibrium dynamics.

Linear Response around Nonequilibrium Steady State

Lastly, we discuss a system out of equilibrium even at $X = 0$. This is fundamentally different from the two cases above, as even at linear response traditional Green-Kubo formulas do not apply. Nevertheless the response of the system is still encoded in a LDF computed at $X = 0$, though one evaluated in the nonequilibrium steady state. The previously derived extended fluctuation-dissipation theorems [19–21] follow naturally from our general expression for the nonequilibrium current in Eq. 2.32.

We consider an underdamped particle with unit mass moving in a 2D hydrodynamic flow

$$\dot{v}_x = -\gamma(v_x - U_x) + F + \eta_x, \;\; \dot{v}_y = -\gamma(v_y - U_y) + \eta_y \,, \tag{2.47}$$

where $U_x = \partial\phi(\boldsymbol{r})/\partial r_y$ and $U_y = -\partial\phi(\boldsymbol{r})/\partial r_x$ describe the divergenceless flow of the stream function $\phi(\boldsymbol{r}) = LU_0 \sin(2\pi r_x/L)\sin(2\pi r_y/L)/(2\pi)$. We set $U_0 = L = 1$, which sets a scale for length and time. The noise η_i's satisfy $\langle \eta_i(t)\rangle = 0$, $\langle \eta_i(0)\eta_j(t)\rangle = 2\gamma\delta_{ij}\delta(t)/\beta, i = x, y$. When the constant force $F = 0$, it is the non-gradient form of the velocity field that forces the system out of equilibrium, though the average particle current still vanishes due to spatial symmetry. As a consequence, the linear response of the particle current includes two terms proportional to X, as shown in Eq. 2.32. The extended fluctuation-dissipation theorem includes a term that is the correlation between the current and a time symmetric variable derived from the first order part of the relative action as has been described previously [18]. Defining the affinity $X = F/2$, the dynamical variables are

$$j(\tilde{x}_t) = v_x(t), \quad q_1(\tilde{x}_t) = \dot{v}_x(t)/\gamma - U_x(t)\,. \tag{2.48}$$

The time symmetric term includes the particle's inertia, relative to its local flow velocity, which is only a function of the particle's position. The linear response of the current can be viewed as a Green-Kubo relation, but correlating particle's velocity relative to the velocity field U_x [19, 21], up to a boundary term from the integral of $\dot{v}_x$.

We note that the dynamical variables satisfy the relation $j(\tilde{x}_t) + q_1(\tilde{x}_t) = \eta_x/\gamma$ when $F = 0$, which implies that $t_{\rm N}^{n-1}\langle (J+Q_1)^n\rangle_0 = (2/(\gamma\beta))^{n/2}(n-1)!!$ if n is even, and vanishes if n is odd. Note that this type of relationship is not restricted to this specific model - it is quite general for stochastic systems with quadratic path actions. These constraints on the moments reduce the number of unknown moments we have to compute. Here, we use the fact that the second order moments satisfy $t_{\rm N}\langle (J+Q_1)^2\rangle_0 = 2/(\gamma\beta)$, which allows us to rewrite the linear response as

$$\langle J\rangle_F = \beta\left(\frac{1}{\gamma\beta} + \frac{t_{\rm N}}{2}\langle J^2\rangle_0 - \frac{t_{\rm N}}{2}\langle Q_1^2\rangle_0\right)\frac{F}{2} + O(F^2)\,. \tag{2.49}$$

To compute the linear response coefficient, all we need are the curvatures of $\psi_0(\boldsymbol{\lambda})$ along $\lambda_J = 0$ and $\lambda_{Q_1} = 0$, which are easily computable from the cloning algorithm.

In the following calculations, we set $\gamma = 0.1$, $\beta = 0.5\times 10^4$. The underdamped equation is integrated with a second order Verlet-like integrator [76], with a timestep of $h = 10^{-3}$. Both nonequilibrium results and LDFs are calculated from trajectories of the length $t_{\rm N} = 8\times 10^5$. Fig. 2.2(a) and (b) shows the LDF while fixing $\lambda_{Q_1} = 0$ and $\lambda_J = 0$, respectively. To evaluate $t_{\rm N}\langle J^2\rangle_0$, we compute the LDFs at $\lambda_J \in [-0.0035, 0.0035]$, $\lambda_{Q_1} = 0$ and fit the curve with a parabola to estimate its curvature. Similarly, $t_{\rm N}\langle Q_1^2\rangle_0$ is estimated with LDFs at $\lambda_J = 0$, $\lambda_{Q_1} \in [-0.0035, 0.0035]$. The statistical errors in LDFs are estimated by the standard deviation among 15 independent samples. To evaluate the statistical error in the linear transport coefficient, we fit a parabola to each of the sample sets, and compute the standard error of the mean among the 15 curvatures. The fitted curves yield an estimate of $t_{\rm N}\langle J^2\rangle_0/2 = 2.6874 \pm 0.0015$, $t_{\rm N}\langle Q_1^2\rangle_0/2 = 2.6773 \pm 0.0013$, and the mobility is 30.2 ± 6.8.

In Fig. 2.2(c), we plot the theoretically predicted linear response along with the nonequilibrium simulation results to show their agreement at small values of F. Nonequilibrium results

are averaged over 2400 independent trajectories and standard errors of the mean are plotted. This model has recently been shown to exhibit a negative differential mobility [77]. Near equilibrium, the mobility is proportional to $\langle J^2 \rangle_0$, and thus must be non-negative. However, the linear response around a nonequilibrium steady state given in Eq. 2.49 clarifies how a negative differential mobility is possible. While not true at the conditions we consider, in principle $t_{\mathrm{N}} \langle Q_1^2 \rangle_0$ may be larger than $2/(\gamma\beta) + t_{\mathrm{N}} \langle J^2 \rangle_0$, resulting in a current that decreases with added force.

2.3 Linear Transport Coefficients: Comparison with Green-Kubo [2]

As seen in the last section, transport coefficients can be derived from the large deviation function, and to the first order, our result agrees with the Green-Kubo expression. In fact, this result can be derived alternatively from the projected large deviation function merely on the dimension of λ_J

$$\psi_X(\lambda_J, \lambda_{Q_i} = 0) = \lim_{t_{\mathrm{N}} \to \infty} \frac{1}{t_{\mathrm{N}}} \ln \left\langle e^{-\lambda_J t_{\mathrm{N}} J} \right\rangle_X \,, \tag{2.50}$$

where all the λ_{Q_i} in Eq. 2.29 are set to zero. For simplicity, we'll refer to this projected LDF as ψ, and use λ instead of λ_J for the rest of the section. As before, the derivatives of $\psi(\lambda)$ report on the fluctuations of the current J,

$$\frac{\partial \psi(\lambda)}{\partial \lambda}\Big|_{\lambda_J = 0} = -\langle J \rangle_X \,, \quad \frac{\partial^2 \psi(\lambda)}{\partial \lambda^2}\Big|_{\lambda = 0} = t_{\mathrm{N}} \left\langle \delta J^2 \right\rangle_X \,. \tag{2.51}$$

According to the fluctuation theorem Eq. 1.29, $\psi(\lambda)$ obeys the Gallovati-Cohen symmetry

$$\psi(\lambda) = \psi(\beta X - \lambda) \,, \tag{2.52}$$

where X is the generalized force as in Eq. 2.24. This symmetry implies a relation between the second derivatives of the large deviation function

$$\frac{\partial^2 \psi_X(\lambda)}{\partial \lambda \partial X}\Big|_{\lambda=0, X=0} = -\frac{\partial \langle J \rangle_X}{\partial X}\Big|_{X=0} = -\beta \frac{\partial^2 \psi_0(\lambda)}{\partial \lambda^2}\Big|_{\lambda=0} \,. \tag{2.53}$$

Combined with Eq. 2.24, this gives us the same expression as Eq. 2.35,

$$L_1 = \beta \frac{\partial^2 \psi_0(\lambda)}{\partial \lambda^2}\Big|_{\lambda=0} \,, \tag{2.54}$$

which states that the curvature of the large deviation function around $\lambda = 0$ is equal to the linear response coefficient L_1. For small values of λ, the large deviation function can be expanded as

$$\psi_0^2(\lambda) = \frac{1}{2} L_1 \lambda^2 + O(\lambda^4) \,, \tag{2.55}$$

[2] Most of the content of this section was originally written by the author for the following publication: C. Y. Gao and D. T. Limmer, "Transport Coefficients from Large Deviation Functions", *Entropy* **2017**, 19 (11).

which is parabolic, and completely determined by L_1. This implies the distribution of J is Gaussian, with a variance of $L_1/t_{\rm N}$. This inversion is a direct reflection of Onsager's notion of an effective thermodynamic potential, where the probability of a current is given by the exponential of the entropy production.

The connection between the large deviation result and the Green-Kubo formalism can be understood by invoking the time translational invariance of the equilibrium averaged time-correlation function,

$$\frac{\beta t_{\rm N}}{2}\left\langle(\delta J)^2\right\rangle_0 = \lim_{t_{\rm N}\to\infty}\beta\int_0^{t_{\rm N}}\langle j(\tilde{x}_0)j(\tilde{x}_t)\rangle dt\,, \tag{2.56}$$

where the right hand side is the familiar time integral over the current auto-correlation function that appears in the Green-Kubo relations, assumed to decay faster than $1/t$. As $\langle J\rangle = 0$ for an equilibrium system, where $X = 0$, it is straightforward to relate the second derivative of the large deviation function with respect to λ evaluated at $\lambda = 0$, to L_1 as

$$\psi_0^{''}(0) = 2\beta\int_0^{\infty}\langle j(\tilde{x}_0)j(\tilde{x}_t)\rangle\, dt = L_1\,, \tag{2.57}$$

This equation is known as the Einstein-Helfand relation and is well known to yield an equivalent expression for transport coefficients [39]. The additional factor of 2 is merely a result of our definition of the affinity in Eq. 2.25. Provided an estimate of $\psi_0(\lambda)$ accurate enough to compute $\psi_0^{''}(0)$, we thus have an alternative means of evaluating L_1. In what follows, we use a few examples to illustrate the relative systematic and statistical errors associated with the large deviation function method in comparison to traditional Green-Kubo calculations.

Analysis of Systematic Error: Interfacial Friction Coefficient

We first focus on the systematic errors determining the convergence of both methods. As a case study, we consider computing the interfacial friction coefficient between a liquid–solid interface. This friction coefficient is defined by the linear relationship,

$$f_x = -\mu A v_s\,, \tag{2.58}$$

where f_x is the total lateral force exerted on the solid wall on the x direction, A is the lateral area of the interface, and v_s is the tangential velocity of the fluid relative to the solid. We can identify a relevant molecular current as the momentum flux along the wall, in this case proportional to

$$f_x = -\sum_{i=1}^{N_l}\sum_{k=1}^{N_c}\frac{d}{dx_i}u_{ls}(|\mathbf{r}_i - \mathbf{r}_k|)\,, \tag{2.59}$$

the sum of the x component of the forces of all N_l liquid particles on the N_c wall particles, where the force is given by the gradient of the liquid-solid interaction potential u_{ls}. Given

this current, we can identify its conjugate force as $X = (A/T)v_s$, and, consequently, the friction coefficient is given by $\mu = L(A/T)$.

The system is modeled as a fluid of monatomic particles confined between two stationary atomistic walls parallel to the xy plane. The fluid particles interact through a Lennard-Jones (LJ) potential with characteristic length scale d, energy scale ϵ, time $\tau = \sqrt{md^2/\epsilon}$ with m as the mass of the fluid particle, and is truncated at $2.5d$. Reduced units will be used throughout this subsection. The walls are separated by a distance $H_z = 18.17d$ along the z-axis. Periodic boundary conditions are imposed along x- and y-directions, with the lateral dimensions of the simulation domain $H_x = H_y = 15.90d$. Each wall is constructed with 1568 atoms distributed as (111) planes of face-centered-cubic lattice with density $\rho_w = 2.73d^{-3}$, while the fluid density is $\rho_f = 0.786d^{-3}$. The wall atoms do not interact with each other, but are allowed to oscillate about their equilibrium lattice sites under the harmonic potential $u_h(r) = kr^2/2$, with a spring constant $k = 600\epsilon/d^2$. The mass of the wall atoms is chosen to be $m_c = 4m$. The interaction between the wall and the fluid atoms is also modeled by a LJ potential with the same length scale d and truncation, but a slightly smaller energy $\epsilon_{wf} = 0.9\epsilon$, to model the solvophobicity of the wall [78]. Only the wall particles are thermostatted by the Langevin equation

$$m_i\ddot{\mathbf{r}}_i = -\bigtriangledown_{\mathbf{r}_i} U(\mathbf{r}^N) - m_i\gamma\dot{\mathbf{r}}_i + \mathbf{R}_i\,, \tag{2.60}$$

where the dots denote time derivatives, $U(\mathbf{r}^N)$ is the total intermolecular potential from all N particles at position $\mathbf{r}^N$, m_i is the particle's mass, $\gamma = \tau^{-1}$ is the frictional coefficient, and $\mathbf{R}_i$ is a random force. The statistics of the random force is determined by the fluctuation-dissipation theorem, which for each component is

$$\langle R_i(t)\rangle = 0\,, \quad \langle R_i(t)R_j(t')\rangle = m_i k_{\mathrm{B}} T\gamma\delta(t-t')\delta_{ij}, \tag{2.61}$$

where $\delta(t)$ is Dirac's delta function and δ_{ij} is the Kronecker delta.

Previous studies have recognized that μ is difficult to compute due to the confinement of the corresponding hydrodynamic fluctuations [79, 80], which results in a large systematic error. This difficulty has led to some questioning the reliability and applicability of Green-Kubo calculations to compute μ, such as the one shown in Table 1.1 [81],

$$\mu = \frac{A}{k_B T}\int_0^{t_M} \langle f_x(0)f_x(t)\rangle\, dt, \quad t_M \to \infty\,. \tag{2.62}$$

Indeed, we have found that the details of the simulation, such as the ensemble, system geometry and γ used in the Langevin thermostat, all have an important influence on the calculation of μ. This sensitivity is because the fluctuations that determine the friction are largely confined to two spatial dimensions, which is well known to result in correlations that have hydrodynamic long time tails, whose integral may be divergent [82]. However, both our large deviation function method and the Green-Kubo calculations are based on equilibrium fluctuations. Provided an ensemble, simulation geometry, and equation of motion, the system samples the exact same trajectories, so we expect the friction coefficient computed in both

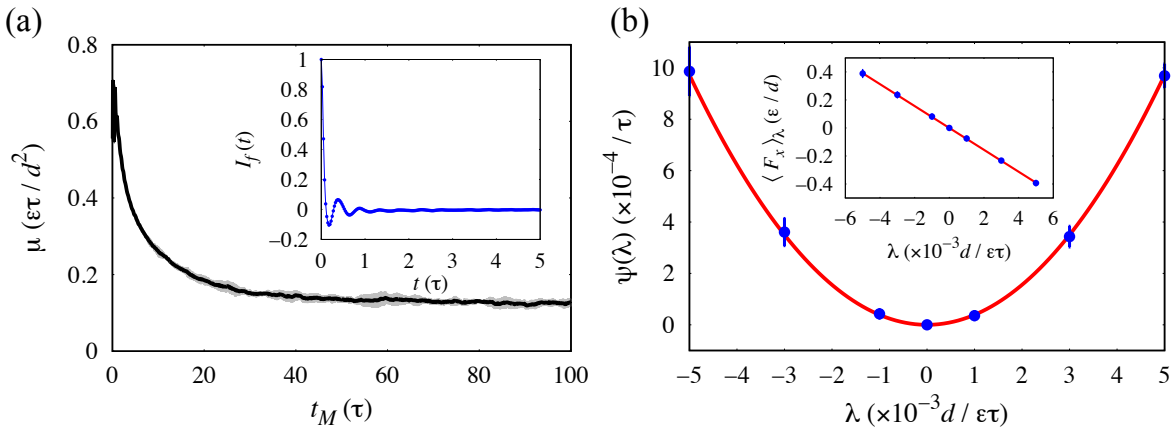

Figure 2.3: (a) Interfacial friction coefficient computed from Green-Kubo method as a function of the integration time t_M. (*Inset*) The normalized force auto-correlation function $I_f(t) = \langle f_x(0) f_x(t) \rangle \,/\, \langle f_x(0)^2 \rangle$. (b) Large deviation function of the dynamical observable F_x with $t_N = 400\tau$. The red line is the parabolic fit. (*Inset*) The average observable $\langle F_x \rangle_\lambda$ in the biased ensemble, with the linear fit in red.

ways to agree. Shown in the inset of Fig. 2.3(a) is the Green-Kubo correlation function, which includes a very slow decay extending to at least 100τ, following short time oscillatory behavior from the layered density near the liquid-solid interface. The main panel of Fig. 2.3(a) shows μ computed with increasing integration time t_M. Averaging over four independent samples with a cutoff $t_M = 1000\tau$, our estimation of the friction coefficient is $\mu = 0.109 \pm 0.019\epsilon\tau/d^2$. The interfacial friction coefficient is also computed from the large deviation function, with $t_\mathrm{N} = 400\tau$, using the time integrated force

$$F_x = \frac{1}{t_\mathrm{N}} \int_0^{t_\mathrm{N}} f_x(t) dt \,, \tag{2.63}$$

as our dynamical observable. The large deviation function and the average time integrated force $\langle F_x \rangle_\lambda$, are shown in the main panel and inset of Fig. 2.3(b), respectively, demonstrating that within the range of λ we consider the system still responds linearly. With $\lambda = 10^{-3}\sigma/\epsilon\tau$ and $t_\mathrm{N} = 4000\tau$, importance sampling gives us an estimate of the friction coefficient as $\mu = 0.121 \pm 0.002\epsilon\tau/d^2$, in reasonable agreement with the Green-Kubo estimate and with previous reports [79].

In both the Green-Kubo and the large deviation function calculations, the main source of systematic error is from finite time. This error is especially highlighted in this example, where the time-correlation function decays very slowly. We consider the systematic errors in the estimate of μ by defining a relative error as

$$\mathrm{Err}^{(\mathrm{sys})}[\mu] = (\mu(t) - \mu)/\mu \,, \tag{2.64}$$

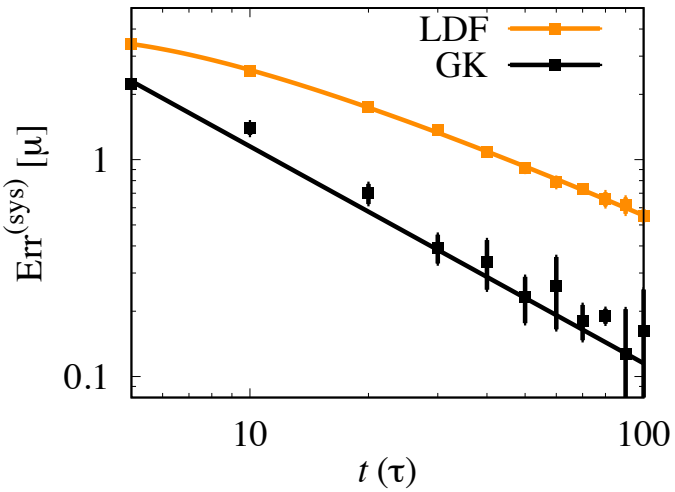

Figure 2.4: Relative systematic error $\mathrm{Err}^{(\mathrm{sys})}[\mu]$ due to finite time in the estimation of μ in the Green-Kubo method (black dots) and the large deviation function (LDF) method (orange dots). The time t in the x-axis denotes the upper limit of the integral, t_M in the Green-Kubo method, or the total length of the trajectory, t_{N} in computing the large deviation function. The orange line is a fit to the function $y = (a/t)\ln(bt)$, and the black line is a fit to $y = a/t$.

where $\mu(t)$ is the finite time value of the friction coefficient, and μ its asymptotic value at $t \to \infty$. The form of the time dependent systematic error is different in the Green-Kubo method compared to the large deviation estimate. In the Green-Kubo method, systematic errors come from truncating the integral before the correlation function has decayed, and we denote this time t_M, as the cutoff time in the integral of the correlation function. In the large deviation calculation, systematic errors come from both truncating the integral as well as sub-time-extensive contributions to the exponential expectation value, which are more analogous to finite size effects in normal free energy calculations. These contributions are both determined by the path length t_{N}. The relative systematic error is shown in Fig. 2.4 for both methods. For this case, it appears that the Green-Kubo method always has a smaller error than the large deviation function method, though their magnitudes are comparable.

In the Green-Kubo method, it follows that, if we know the analytical form of the correlation function, we can determine the scaling of the relative error. In the case of interfacial friction, Barrat and Boquet have proposed that for a cylindrical geometry where the dimension on the confined direction is much smaller than the other two directions, the force auto-correlation should decay asymptotically as $\sim 1/t^2$ using hydrodynamic arguments [81]. This is a direct consequence of the fact that the velocity autocorrelation function decays as $\sim 1/t$ in a two-dimensional system [82], neglecting the self-consistent mode coupling correction that adds an imperceptible $\sqrt{\ln t}$ correction [83, 84]. This is confirmed in our simulation result in

Fig. 2.4 (black line), where the integral of the force correlation function decays as $\sim 1/t$.

Since the large deviation function has a Gaussian form, we can analyze the form of the finite time correction exactly as

$$\mathrm{Err}^{(\mathrm{sys})}[\psi] = \frac{\tilde{\psi}(\lambda, t_N) - \psi(\lambda)}{\psi(\lambda)} = \frac{\mu(t_\mathrm{N}) - \mu}{\mu} + \frac{1}{2t_\mathrm{N}\mu\lambda^2} \ln[4\pi t_\mathrm{N}\mu(t_\mathrm{N})]\,, \tag{2.65}$$

where $\psi(\lambda)$ is the long time limit of the large deviation function, and $\tilde{\psi}(\lambda, t_\mathrm{N})$ is its finite time estimate. This follows from a fluctuation correction about a saddle point integration. Physically, this correction arises from a t_N that is too short, such that $\psi(\lambda)$ is not the dominant contribution to the tilted propagator, but rather includes temporal boundary terms from the overlap of the distribution of initial conditions and the steady state distribution generated under finite λ [68]. If we expand the first term, we arrive at

$$\mu(t_\mathrm{N}) - \mu \approx -\int_{t_\mathrm{N}}^{\infty} \langle j(0)j(t)\rangle\, dt + \frac{1}{t_\mathrm{N}} \int_0^{t_\mathrm{N}} t\, \langle j(0)j(t)\rangle\, dt\,, \tag{2.66}$$

which consists of the term included in the Green-Kubo expression, as well as an additional term modulated by a factor of $1/t_\mathrm{N}$. Given that the correlation decays as $\sim 1/t^2$, the first term on the right hand side scales as $\sim 1/t_\mathrm{N}$, as in the Green-Kubo method, while the second term scales as $\sim (1/t_\mathrm{N}) \ln t_\mathrm{N}$. This form is shown in Fig. 2.4 and agrees very well with our data. These additional terms explain why the magnitude of the systematic error is larger for the large deviation function. In cases where the Green-Kubo correlation function decays faster than $1/t^2$, we expect that the dominant contribution to the error will come from the last term in Eq. 2.65.

Analysis of Statistical Error: Thermal Conductivity

We finally discuss the statistical error of our method by studying the thermal conductivity κ, of a solid system with particles that interact via the Weeks-Chandler-Anderson (WCA) potential [85]. The thermal conductivity is defined through Fourier's law,

$$\mathbf{e} = -\kappa \nabla \mathbf{T}\,, \tag{2.67}$$

where $\mathbf{e}$ is the energy current per unit area and $\nabla\mathbf{T}$ is the temperature gradient. From the form of the entropy production in Eq. 1.4, the thermodynamic force is given by $X = -(1/k_\mathrm{B}T^2)\nabla T$, and so the thermal conductivity $\kappa = L/(Vk_\mathrm{B}T^2)$. As the relevant molecular current, we study the fluctuations of the heat flux $\mathbf{q}$ given by

$$\mathbf{q} = \mathbf{e}V = \sum_i \mathbf{v_i} e_i + \frac{1}{2}\sum_{i\neq k} (\mathbf{f_{ik}} \cdot \mathbf{v_i})\mathbf{r_{ik}}\,, \tag{2.68}$$

where e_i is the per-particle energy, $\mathbf{f_{ik}}$ is the force on atom i due to its neighbor k from the pair potential, and $\mathbf{r_{ik}}$ is the coordinate vector between the two particles. We use a system

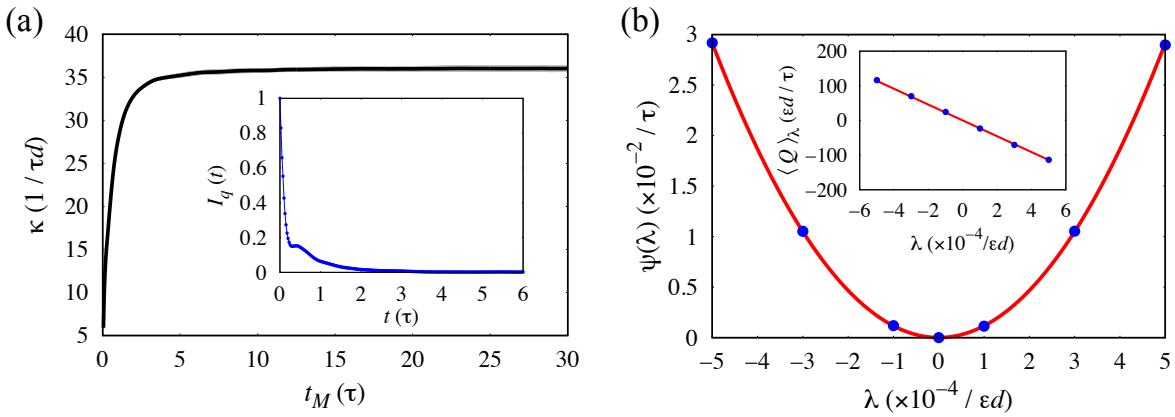

Figure 2.5: Calculation of the thermal conductivity κ, of a WCA solid at $T = 1.0\epsilon/k_{\rm B}$, $\rho = 1.2d^{-3}$. (a) $\kappa(t_M)$ calculated by integrating the heat flux correlation function up to time t_M. The data are averaged from four samples and the error bars are standard deviations, which are smaller than the symbols. (*Inset*) The normalized heat flux correlation function $I_q(t) = \langle q_x(0)q_x(t)\rangle \,/\, \langle q_x(0)^2\rangle$. (b) Large deviation function of dynamical observable Q_x, as a function of the bias λ. The red line is the parabolic fit. (*Inset*) The average observable in the biased ensemble $\langle Q\rangle_\lambda$, as a function of λ with the linear fit in red.

size of 10^3 unit cells, with lattice spacing $1.49d$. A Langevin thermostat with $\gamma = 0.01\tau^{-1}$ maintains the system at the state point $T = 1.0\epsilon/k_{\rm B}$, $\rho = 1.2d^{-3}$, which yields identical results for κ as an NVE calculation. We focus on the diagonal component κ_{xx}, of the thermal conductivity tensor.

Within Green-Kubo theory, the thermal conductivity can be computed by integrating the auto-correlation function of the x component of the heat flux q_x,

$$\kappa = \frac{1}{Vk_{\rm B}T^2}\int_0^{t_M} \langle q_x(0)q_x(t)\rangle\, dt, \quad t_M \to \infty\,. \tag{2.69}$$

The inset of Fig. 2.5(a) is the decay of the auto-correlation function, which comprises a fast decay from the high frequency vibrational modes, followed by a slower decay that contributes most to the thermal conductivity and arises due to the low frequency acoustic modes [86]. To compute κ from the integral, as shown in the main part of Fig. 2.5(a), the upper time limit is chosen as $t_M = 1500\tau$, though the relaxation of the correlation extends only to around 5τ. To compute κ from the large deviation function, we study fluctuations in the time averaged heat flux,

$$Q_x = \frac{1}{t_{\rm N}}\int_0^{t_{\rm N}} q_x(t)dt\,. \tag{2.70}$$

The transport coefficient κ, is again calculated using Eq. 2.57 by assuming the large deviation function $\psi(\lambda)$ as a parabola, which is justified in Fig. 2.5(b). The inset there shows clearly

the linear response of the biased ensemble average $\langle Q \rangle_\lambda$, computed in the tilted ensemble Eq. 2.8. Given sufficient statistics the two methods converge to the same value. The estimate of thermal conductivity from the Green-Kubo method using a long trajectory of $1.5 \times 10^6 \tau$ is $\kappa = 34.3 \pm 2.2 k_\mathrm{B}/\tau d$, while the estimate from the large deviation function using $N_\mathrm{w} = 1000$ walkers and $\lambda = 10^{-4}$ is $\kappa = 34.01 \pm 0.78 k_\mathrm{B}/\tau d$.

While the average values of κ agree between the two methods, the statistical convergence varies significantly. To make a fair comparison, we set the total observation time of the trajectories to the same time as the upper limit of the Green-Kubo integral, i.e., $t_\mathrm{N} = t_M = 1500\tau$, which is much longer than the characteristic decay of the current auto-correlation function. To compensate for computational overhead of propagating N_w trajectories in parallel in the cloning algorithm, the total averaging time of the Green-Kubo method is chosen as $t_\mathrm{tot} = t_M \times N_a$, and N_a equals the walker number N_w, so that the two methods require approximately the same computational effort. Both N_a and N_w will be denoted as N_s reflecting the number of independent samples of each fluctuating quantity. We measure the statistical error by the relative error

$$\mathrm{Err}^{(\mathrm{stat})}[\kappa] = \frac{\sqrt{\langle \delta\kappa^2 \rangle}}{\kappa}\,, \tag{2.71}$$

which is plotted in Fig. 2.6 for both methods. As usual, the statistical error depends on both the relative size of observable fluctuations, and the number of independent samples. We find that as the standard deviations of both methods scale as $1/\sqrt{N_s}$ as expected, our importance sampling clearly helps to suppress the statistical error compared to the Green-Kubo method with similar computational effort, decreasing the magnitude of the error by an order of magnitude at fixed N_s. Even though we have to choose a bias small enough to guarantee a linear response, we do see that larger bias helps to yield statistically reliable results.

Jones and Mandadapu have performed a rigorous error analysis on the estimates of Green-Kubo transport coefficients with the assumption that the current fluctuations follow a Gaussian process [87]. They found that the variance of κ is a monotonically increasing function of t_M, and arrived at an upper bound for the relative error

$$\mathrm{Err}^{(\mathrm{stat})}[\kappa] < 2\sqrt{\frac{t_M}{t_\mathrm{tot}}} = 2\sqrt{\frac{1}{N_a}}\,, \tag{2.72}$$

which depends only on the number of trajectory segments of length t_M. As a consequence, the statistics become worse when the system has longer correlation times, and there are no ways of controlling the intrinsic variance of the observable. On the other hand, in the large deviation method, the relative error in the large deviation function is

$$\mathrm{Err}^{(\mathrm{stat})}[\psi(\lambda)] = \frac{1}{\psi(\lambda)}\sqrt{\frac{\psi''(\lambda)}{N_\mathrm{w}}} = \frac{1}{\lambda^2}\sqrt{\frac{2}{LN_\mathrm{w}}} \quad |\lambda| > 0\,, \tag{2.73}$$

which depends not only on the number of samples, in this case , but also has a dependence on λ and L. In general, as λ increases, the walkers will become more correlated. However,

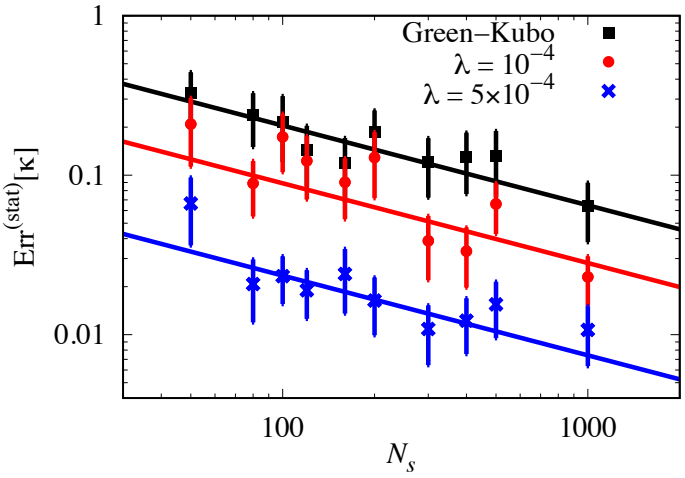

Figure 2.6: Relative statistical error in the measurement of κ, from the Green-Kubo method (black) and the large deviation function method with $\lambda = 10^{-4}$ (red) and $\lambda = 5 \times 10^{-4}$ (blue). N_s denotes the number of walkers N_{w} used in evaluating the large deviation function, or N_a, an indicator of the total averaging time in the Green-Kubo method. The solid lines are fits of function $y = a/\sqrt{N_s}$.

within the regime of linear response, or to first order in λ, the number of uncorrelated walkers should be N_{w}. Because the large deviation function, $\psi(\lambda)$, scales as λ^2 while its second derivative, $\psi''(\lambda)$, has no dependence on λ, the relative size of the fluctuations can be tuned by changing λ away from 0. This is verified in Fig. 2.6, where increased λ generates an order of magnitude reduction in the statistical error relative to the Green-Kubo calculation. This decrease in the statistical error is also confirmed for a series of λs. This tunability afforded by the large deviation function calculation is the same advantage afforded by direct simulation of transport processes where the relative size of fluctuations is determined by the size of the average current produced by driving the system away from equilibrium. Instead of evaluating κ from the large deviation function directly, we could have derived it from the change in the average current produced at a given λ. However, in such a case, the relative error would only scale as $|\lambda|$ rather than λ^2.

2.4 Summary

To summarize, our theory provides a direct relation between the classical statistical mechanical theory of irreversible processes built around correlation functions, and the modern language of large deviation theory. The connection should be obvious given Green's Fokker-Planck description of random irreversible processes, so our main contribution here is to make the

connection concrete, and derive specific expressions for different systems. We conclude this chapter by reviewing some of the advantages and limitations of our method. While our formalism is exact, it is by no means the only way, or the best possible way, to express nonlinear transport coefficients. Therefore, we will also compare our formalism with other previous developed nonlinear generalisations of the Green-Kubo relations, such as the time transient correlation function (TTCF) formalism mentioned in Section 1.2.

Firstly, the method we propose is general enough that it can be applied to stochastic systems both near and far from equilibrium, regardless of the specific type of affinity, as long as a microscopic definition of current and path action can be written down. While we have commented in Section 1.2 the difficulty in treating internal disturbances, we will show an example of heat transport generated by temperature gradients later in Chapter 4. As will be seen, our method not only describe thermal transport processes driven by boundary conditions, but also mechanical transport processes driven by a perturbing external force field.

Secondly, while we do not expect our method to replace direct measurement of transport coefficients from molecular simulations, it does provide an alternative methods to evaluate and understand higher order response functions. Nonequilibrium molecular simulations are known to be sensitive to algorithm details. For example, shear viscosity can be computed from either the system subject to a sinusoidal transverse force extrapolated to infinite wavelength [88], or planar shear with external particle reservoirs [89], or induced Couette flow using the Lees-Edwards periodic boundary condition [90]. The inhomogeneities in the thermodynamic properties of the fluid arising from the boundary conditions can cause trouble in the calculation of the shear viscosity. What's more, to maintain a nonequilibrium steady state, one needs to choose a thermostat, which in turn alters the system equation of motion, and needs to be treated carefully to not interfere with the system's intrinsic response [91–93].

While the values of the transport coefficients derived from our method does depend on simulation details through the relative stochastic action, its computation can involve only equilibrium simulations, which is much more straightforward to carry out practically. By analyzing how the time-reversal symmetric term is modified by the thermostat, we can also analyze the effect of the thermostat on the system response. As seen in Section 2.3, our method is expected to exhibit superior statistical performance compared to methods relying on TTCFs, based on a detailed study on the statistical error in the computation of linear transport coefficients by the Green-Kubo formulas and our method. Higher order transport coefficients demand a more accurate evaluation of the large deviation function. However, with the advancement of algorithms enhanced by importance sampling techniques, we expect that our method will become a standard approach to computing higher order transport coefficients. Besides, for a physically relevant range of fields, the transport behaviors of the system is often well predicted by a few lower order transport coefficients. Even restricting ourselves to the first and second-order effect, as we'll show in the examples in the following chapters, already provides us with some fruitful insights in nonlinear transport behaviors.

Thirdly, apart from a computational tool to evaluate higher order transport coefficients, our method also provides molecular interpretation for nonlinear transport behaviors. This

will be paramount in our understanding of how nonlinear behaviors arise from complex molecular interactions, and in turn provides guiding principles in the control of nonlinear behaviors. By constructing a LDF of both the time symmetric and asymmetric dynamical variables, we arrive at a function that contains all of the information about current-affinity relationship as encoded through microscopic correlations. As will be seen in the examples given in the following chapters, decoding these microscopic correlations will bring fruitful physical understanding of nonlinear transport behaviors.

As for the limitation of our method, the basic assumption of our theory is that there exists a power expansion for the nonequilibrium phase space distribution function and the current in terms of the affinity, and thus we can write down an explicit formula for the higher order transport coefficients. Critics of Kubos nonlinear response theory have pointed out that for many transport processes, such expansions do not exist [94, 95]. Indeed, a perturbative treatment breaks down when long range or long time-correlations exist in a system in the thermodynamic limit. These divergences are known as the Dorfman's Lemma, which states that all relevant fluxes are nonanalytic functions of all relevant variables [96, 97]. Such a behavior can happen in the vicinity of phase transitions, where diverging correlation lengths will cause a divergence in the correlation functions corresponding to the transport coefficients. As a result, our simple series expansion is likely to fail in describing dynamical phase transitions between nonequilibrium steady states. Additionally, constraints on dynamics can also result in long range correlations. For example, low dimensional molecular fluids are known to exhibit diverging diffusivity computed from the Green-Kubo formula, which originates from the slowly decaying correlation of hydrodynamic modes associated with conserved quantities [82, 98]. In deterministic systems, conservation of energy and momentum confines the trajectories of the system to certain manifolds of the phase space. As a consequence, currents associated with conserved quantities are often non-analytic functions of the affinity [99]. To circumvent such problems, we will restrict ourselves to Markovian stochastic systems in the present work, where ergodicity is guaranteed. In all the examples shown, correlation functions decay to zero in microscopic timescales, so that their integrals in the long time limit are well defined. With that being said, our method does exclude applications to certain interesting processes involving memory effects, which may be important in rheological and hydrodynamic phenomena.

As for some potential extensions of our work, we note that the structure of the large deviation function dictates that we are restricted to behaviors in the nonequilibrium steady state. As a result, the access to full time-dependent response is lost, unlike in the TTCF formalism. It is also unclear how to deal with time-dependent affinity, which traditionally involve complicated manipulations of the evolution propagators, similar to quantum field theory [95]. However, with the development of level 2.5 large deviation theory for inhomogeneous Markovian processes, one can imagine that at least the analysis of periodic driven system should be approachable [100]. Furthermore, the expression of transport coefficients in terms of multi-time correlation functions builds a connection between macroscopic transport processes and microscopic observables. We expect that theoretical manipulations on these multi-time correlation functions will yield useful symmetry arguments similar to the Onsager

reciprocal relations [8], and give us further insights into how nonlinear response behaviors arise from the molecular details of the system.

Chapter 3

Ion Transport: Field-dependent Conductivities in Ionic Solutions

3.1 Introduction

In the previous chapter, we derived generalized fluctuation-dissipation relationship for transport processes. Our approach is general and can be applied to any systems or transport processes where a connection between nonlinear transport behavior and underlying microscopic dynamics is desired. In this chapter, we focus on a specific nonlinear transport behavior that is of importance both from the theoretical and experimental perspective - field-dependent conductivities in ionic solutions. Due to their ubiquity and importance, electrolyte solutions have been central to the development of theoretical physical chemistry [101]. While Debye-Hückel theory provides a fundamental picture of non-ideal strong electrolyte solutions taking into account the electrostatic screening effects, Onsager further considers the dynamical correlation between ions and proposes a correction to the conductivity [102–104]. More specifically, for strong electrolytes in the presence of a finite applied field, the electric field distorts the Debye screening of charges and thus the conductivity increases. This effect is known as the Onsager-Wien effect [105], and has been well observed in both experimental and simulated systems [106–108]. Following the pioneering work by Onsager, subsequent research into the structure and dynamics of electrolyte solutions ushered in modern theoretical techniques employing pair distribution functions and linear response theories, such as the Onsager-Wilson continuum theory [109], Kubo-Kirkwood method [110–112], and stochastic density functional theory [113].

On the other hand, advances in the fabrication of nanofluidic devices have enabled the study of transport processes on small scales, where novel phenomena emerge from the interplay of confinement, fluctuations and molecular granularity [114–117]. In these systems, nonlinear transport is especially pervasive and often qualitatively sensitive to chemical composition. Some of the most striking recent observations have been in electrokinetic transport of electrolyte solutions confined to nanometer dimensions, in which large thermodynamic

gradients can be generated, driving nonlinear responses such as Coulomb blockade and current rectification [118–122]. For example, ionic mobilities have been observed to depend on the driving force of the flow, in a manner dependent on the ion pair and the confining material [115]; ionic rectification can be achieved in nanofluidic diodes or conical pores [120, 123–125]. To gain molecular insight into how these nonlinear behaviors arise from molecular interactions, and provide guidance on the design of nanofluidic devices, we in turn need theoretical and simulation tools.

In this chapter, we develop a theory and accompanying numerical technique to efficiently compute the electric field-dependent conductivity in ionic solutions across all concentration regimes. To demonstrate the generality of our method, we show results for models with both implicit (Section 3.2) and explicit solvent (Section 3.3), and compare our findings to existing analytical theories valid in dilute regimes. For both systems, by decomposing the relevant molecular correlation functions, we show how interplay between ionic relaxational effects and solvent friction give rise to nonlinear behaviors.

3.2 Implicit Solvent Model [1]

Model System Description

We consider a system of N ions composed of N_a anions and N_c cations, in a volume V and fixed temperature T. The ions' positions and velocities are denoted $\mathbf{r}^N = \{\mathbf{r}_1, \mathbf{r}_2, \ldots, \mathbf{r}_N\}$ and $\mathbf{v}^N = \{\mathbf{v}_1, \mathbf{v}_2, \ldots, \mathbf{v}_N\}$, respectively. These variables evolve according to an underdamped Langevin equation,

$$\dot{\mathbf{x}}_i = \mathbf{v}_i\,, \quad m_i\dot{\mathbf{v}}_i = -\zeta_i\mathbf{v}_i + \mathbf{F}_i\left(\mathbf{r}^N\right) + z_i\mathbf{E} + \boldsymbol{\eta}_i\,, \tag{3.1}$$

where m_i and z_i are the ith particle's mass and charge, ζ_i is the friction from the implicit solvent, and $\mathbf{F}_i(\mathbf{r}^N)$ is the interparticle force on ion i derived from an interaction potential, which will be specified below. Each Cartesian component of the random force, $\eta_{i\alpha}$, obeys Gaussian statistics with mean $\langle\eta_{i\alpha}\rangle = 0$ and variance $\langle\eta_{i\alpha}(t)\eta_{j\beta}(t')\rangle = 2k_BT\zeta_i\delta_{ij}\delta_{\alpha\beta}\delta(t-t')$, where k_B is Boltzmann's constant. Finally, $\mathbf{E}$ denotes an applied electric field, with magnitude E, which drives an ionic current through the periodically replicated system. This equation of motion does not conserve momentum, and thus hydrodynamic effects are explicitly neglected throughout.

We will consider two specific model systems, the NaCl electrolyte solution, and a molten salt. For the model of NaCl solution, the interaction potential is a pairwise sum of screened Coulumb potential with dielectric constant ϵ_s, and the Lennard-Jones (LJ) potential,

$$U_{ij}^{LJ} = 4\epsilon_{ij}\left[\left(\frac{\sigma_{ij}}{r_{ij}}\right)^{12} - \left(\frac{\sigma_{ij}}{r_{ij}}\right)^{6}\right]. \tag{3.2}$$

[1] Most of the content of this section was originally written by the author for the following publication: D. Lesnicki, C. Y. Gao, B. Rotenberg and D. T. Limmer, "Field-dependent Ionic Conductivities from Generalized Fluctuation-dissipation Relations", *Physical Review Letters* **2020**, 124 (20).

The LJ parameters for each species are taken from [126] and listed in Table 3.1. Frictions are taken to be $\zeta_i = m_i/\tau_i$ with relaxation times $\tau_c = 0.11$ps for the cations and $\tau_a = 0.25$ps for the anions. We consider 0.1M and 1.0M electrolyte solutions at room temperature and system sizes corresponding to 100 ion pairs.

Table 3.1: Lennard-Jones parameters for each species of NaCl. Lorentz-Berthelot mixing rules are used to compute the cation-anion cross interaction.

	σ_{ii} (Å)	ϵ_{ii} (kJ.mol^{-1})
Na^+	2.58	0.4184
Cl^-	4.4	0.4184

For the molten salt, we consider a model of NaCl at $T = 1200$K with Coulumb and Born-Huggins-Mayer interactions,

$$U_{ij}^{BHM} = A_{ij} \exp(\frac{\sigma_{ij} - r_{ij}}{\rho}) - \frac{C_{ij}}{r_{ij}^6} - \frac{D_{ij}}{r_{ij}^8} \,. \tag{3.3}$$

The Born-Huggins-Mayer parameters are taken from [127] (see Table 3.2). We take the same friction relaxation time $\tau_c = \tau_a = 2$ps for the cations and anions. We consider a density of 1.398g.cm^{-3} and a system size corresponding to 2500 ion pairs.

Table 3.2: Born-Huggins-Mayer parameters for NaCl.

	A_{ij} (kcal.mol^{-1})	ρ (Å)	σ_{ij}(Å)	C (Å^6.kcal.mol^{-1})	D (Å^8.kcal.mol^{-1})
Na^+-Na^+	6.08	0.317	2.340	24.18	11.51
Na^+-Cl^-	4.86	0.317	2.755	161.2	200.07
Cl^--Cl^-	3.65	0.317	3.170	1669.6	3353.63

Reweighting Formalism

To compute the ionic conductivity as a function of electric field, we aim to relate dynamic quantities of the system at a reference field, to those of a system perturbed by an additional applied field. Given the equation of motion in Eq. 3.1, the probability of observing a trajectory $\tilde{x}(t_{\rm N})$, or a sequence of positions and velocities over an observation time $t_{\rm N}$, with an applied field, is

$$P_{\mathbf{E}}[\tilde{x}(t_{\rm N})] \propto e^{-\beta \mathcal{U}_{\mathbf{E}}[\tilde{x}(t_{\rm N})]} \,. \tag{3.4}$$

For uncorrelated Gaussian noises, we have an Onsager-Machlup stochastic action of the form [128]

$$\mathcal{U}_{\mathbf{E}}[\tilde{x}(t_{\rm N})] = \sum_{i=1}^{N} \int_0^{t_{\rm N}} dt \frac{\left[m_i \dot{\mathbf{v}}_i + \zeta_i \mathbf{v}_i - \mathbf{F}_i(\mathbf{r}^N) - z_i \mathbf{E}\right]^2}{4\zeta_i} \,, \tag{3.5}$$

where the stochastic calculus is interpreted in the Itô sense. We will consider trajectories in the limit that $t_{\rm N}$ is large so that only time extensive quantities are relevant.

A perturbing field on the system adds an extra drift to the Gaussian action. As a consequence, we can write down the ratio of the probability to observe a trajectory in the presence of the field, $\mathbf{E} = \mathbf{E}_r + \Delta\mathbf{E}$, relative to the probability to observe the same trajectory with $\mathbf{E}_r$,

$$\frac{P_{\mathbf{E}_r+\Delta\mathbf{E}}[\tilde{x}(t_{\rm N})]}{P_{\mathbf{E}_r}[\tilde{x}(t_{\rm N})]} = e^{\beta\Delta\mathcal{U}_{\Delta\mathbf{E}}[\tilde{x}(t_{\rm N})]}\,, \tag{3.6}$$

where the dimensionless relative action, $\beta\Delta\mathcal{U}_{\Delta\mathbf{E}}[\tilde{x}(t_{\rm N})]$, can be expressed compactly as a sum of three terms, depending on their symmetry under time reversal,

$$\frac{\Delta\mathcal{U}_{\Delta\mathbf{E}}}{t_{\rm N}} = [J + Q - E_r\sigma_{\rm id}V]\,\frac{\Delta E}{2} - \sigma_{\rm id}V\frac{\Delta E^2}{4}\,, \tag{3.7}$$

where for simplicity we take the field along one Cartesian direction so that the relative action depends only on its magnitude.

The first term is asymmetric under time reversal and identified as the excess entropy production due to the increased nonequilibrium driving. It is given by the product of the total, time averaged ionic current in the direction of the field,

$$J[\tilde{x}(t_{\rm N})] = \frac{1}{t_{\rm N}}\int_0^{t_{\rm N}} dt\, j(t)\,, \quad j(t) = \sum_{i=1}^{N} z_i v_i(t)\,, \tag{3.8}$$

and the extra field $\Delta E/2$. The second term in Eq. 3.7 is symmetric under time reversal and referred to as the excess frenesy [22]

$$Q[\tilde{x}(t_{\rm N})] = \frac{1}{t_{\rm N}}\int_0^{t_{\rm N}} dt\, q(t)\,, \quad q(t) = \sum_{i=1}^{N}\frac{z_i}{\zeta_i}\left[m_i\dot{v}_i(t) - F_i(\mathbf{r}^N)\right]\,, \tag{3.9}$$

which includes the total time integrated force in the direction of the field weighted by z_i/ζ_i, and a boundary term resulting in a difference in velocities at times 0 and $t_{\rm N}$, times the extra field. The remaining terms are trajectory independent constants, proportional to the Nernst-Einstein conductivity of the solution

$$\beta V\sigma_{\rm id} = N_c z_c^2 D_c + N_a z_a^2 D_a\,, \tag{3.10}$$

where $D_i = k_B T/\zeta_i$ is the diffusion coefficient for an isolated ion of type i. This decomposition of the relative action admits particularly simple, physically transparent, nonlinear response relations.

With the relative measure between trajectory ensembles defined in Eq. 3.6, we can relate nonequilibrium trajectory averages in the presence of the field, to equilibrium trajectory averages without the field. We do this by setting the reference field, $E_r = 0$, so that $E = \Delta E$. For a trajectory observable $O[\tilde{x}(t_{\rm N})]$, this relation is

$$\langle O\rangle_E = \left\langle O e^{\beta\Delta\mathcal{U}_{\mathbf{E}}[\tilde{x}(t_{\rm N})]}\right\rangle_0\,, \tag{3.11}$$

where trajectory averages over the measure in Eq. 3.4, with field value E, are denoted $\langle \dots \rangle_E$. Setting O to 1, we find a sum rule inherited from the underlying Gaussian process that is quadratic in the field,

$$\left\langle e^{\beta t_{\rm N}(J[\tilde{x}(t_{\rm N})]+Q[\tilde{x}(t_{\rm N})])E/2} \right\rangle_0 = e^{\beta t_{\rm N}\sigma_{\rm id}VE^2/4}\,, \tag{3.12}$$

which is interpretable as the ratio of nonequilibrium to equilibrium trajectory partition functions.

Identifying the joint probability of observing a value of the current and frenesy as $p_E(J,Q) = \langle \delta(J - J[\tilde{x}(t_{\rm N})], Q - Q[\tilde{x}(t_{\rm N})]) \rangle_E$, we can relate $p_E(J,Q)$ to its equilibrium counterpart using Eq. 3.11,

$$\frac{\ln p_0(J,Q)}{t_{\rm N}} = \frac{\ln p_E(J,Q)}{t_{\rm N}} - \beta(J+Q)\frac{E}{2} + \beta\sigma_{\rm id}V\frac{E^2}{4}\,, \tag{3.13}$$

where we find that the nonequilbrium driving acts to reweight the joint distribution linearly in $J+Q$, demonstrating a thermodynamic-like relationship between this sum and its conjugate quantity E. Note that such linearity is not in general valid for the marginal distribution of just the current, $p_0(J) = \int dQ\, p_0(J,Q)$, due to correlations between J and Q. Equation 3.13 provides a route to numerically probe the tails of nonequilibrium probability distributions using generalizations of histogram reweighing techniques, such as those developed for equilibrium systems, like multicanonical sampling [67].

From the joint distribution, $p_0(J,Q)$, we can compute the relationship between the mean current and the applied field arbitrarily far from equilibrium, as encoded in the electric field dependent conductivity $\sigma(E) = (d\langle J \rangle_E/dE)/V$. Using Eq. 3.11 to first write the average current density, and then differentiating with respect to the field, we find

$$\sigma(E) = \lim_{t_{\rm N}\to\infty} \frac{\beta t_{\rm N}}{2V} \left\langle \left(\delta J^2 + \delta J \delta Q\right) e^{\beta \Delta \mathcal{U}_{\mathbf{E}}[\tilde{x}]} \right\rangle_0\,, \tag{3.14}$$

where $\delta O = O - \langle O \rangle$, demonstrating that $\sigma(E)$ is given by a sum of the variance of the current and the current-frenesy correlations, reweighted by the factor that relates the equilibrium average to the nonequilibrium ensemble at fixed E. Near equilibrium ($E \approx 0$), the weight ≈ 1, and fluctuations in J and Q are uncorrelated due to the time reversal invariance of detailed balance dynamics, $\langle \delta J \delta Q \rangle_0 = 0$. In this limit, Eq. 3.14 reduces to a standard Einstein-Helfand relationship. For small values of E, we can expand the weight, and the first non-vanishing term emerges at second order in the field and vanishes for uncorrelated Gaussian random variables.[2]

We have used these formal relationships to study the electric field-dependent conductivity of both NaCl electrolyte solutions, and the molten salt. The results for the NaCl systems are shown in Fig. 3.1 and 3.2, with concentrations of 1M, 0.1M, and dielectric constants

[2]The conductivity to second order in the field is $\sigma(E)/\sigma(0) \approx 1 + \frac{\beta^2 t_{\rm N}^2 E^2}{8\langle J^2 \rangle_0}\left(\langle J^4 \rangle_0 - 3\langle J^2 \rangle_0^2 + 3\langle J^2 Q^2 \rangle_0 - 3\langle J^2 \rangle_0 \langle Q^2 \rangle_0\right)$.

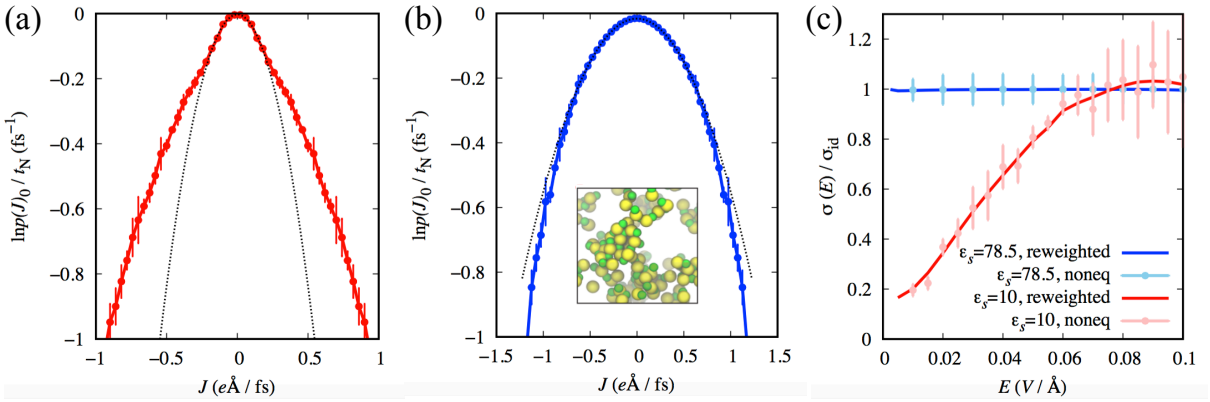

Figure 3.1: Fluctuations and response of the 1M NaCl solution. Log-probability of the time averaged current as computed from histogram reweighting are shown for (a) $\epsilon_s = 10$ and (b) $\epsilon_s = 78.5$. Errorbars are one standard deviation of the mean as computed from bootstrapping analysis. The dashed lines represent Gaussian distributions fitted using the data $|J| \leq 0.4e\text{Å/fs}$. (*Inset*) Characteristic snapshots of the simulated system, with green and yellow spheres representing Na^+ and Cl^- respectively. (c) Field-dependent ionic conductivities relative to the Nernst-Einstein value. Lines are computed from reweighting $p(J, Q)$ and symbols are computed from finite differences of $\langle J \rangle_E$ versus E. Errorbars are one standard deviation of the mean.

of $\epsilon_s = 10$ and 78.5. We find $t_N = 0.2$ps sufficient to converge the conductivity for the electrolyte systems. Shown in Fig. 3.1(a)(b) are the current distributions computed from nonequilibrium molecular dynamics simulations for E between 0 and 0.1 V/Å in steps of 0.01 V/Å combined using Eq. 3.13, followed by marginalization over Q. For the 1M solution of NaCl with $\epsilon_s = 78.5$, the current distribution is mostly Gaussian. The Gaussian statistics follow from the largely dissociated nature of the strong electrolyte in the polar, implicit solvent, which enables ions to move free of correlations from their surrounding environment. Gaussian fluctuations are found for 0.1M NaCl with $\epsilon_s = 78.5$ as well. This is in contrast to calculations with $\epsilon_s = 10$, where ionic correlations depress motions, leading to smaller characteristic current fluctuations, as computed by its variance, $t_N \langle J^2 \rangle_0$. Weaker electrolyte systems exhibit marked deviations from Gaussian statistics with enhanced probability at large values of J. Similar behavior is found for 1M NaCl with $\epsilon_s = 10$.

Shown in Fig. 3.1(c) and Fig. 3.2 are the conductivities computed from $p_0(J, Q)$ continuously as a function of the applied field. We have additionally computed the conductivity from a numerical derivative of the average current versus applied field and find quantitative agreement between both estimates, although the statistical errors are much larger from the finite difference approach at fixed computational cost. For strong electrolytes that exhibit small deviations from Gaussian current fluctuations, we find a conductivity largely independent of the field, while the weak electrolytes exhibiting strong non-Gaussian current fluctuations have

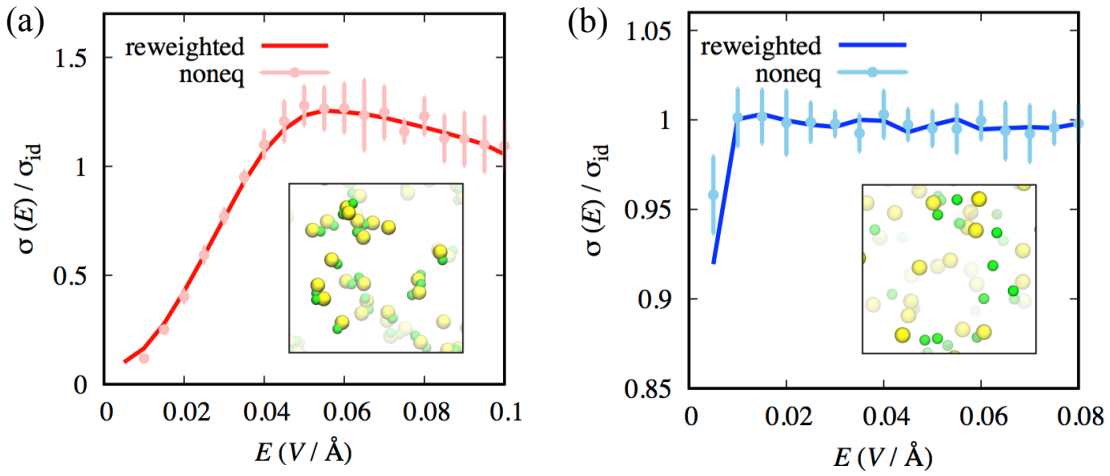

Figure 3.2: Field-dependent conductivities of the 0.1M NaCl solution for (a) $\epsilon_s = 10$ and (b) $\epsilon = 78.5$. Lines and symbols are computed in the same way as Fig. 3.1. (*Insets*) Characteristic snapshots of the system.

conductivities that increase with applied field. The increase is initially quadratic, as observed experimentally [101] for dilute solutions and necessitated by time reversal symmetry, and plateaus at large fields. For both concentrations, the conductivity plateaus to the same value as the strong electrolytes at higher fields. At intermediate fields, the 0.1M solution exhibits a slight maxima in conductivity as has been noted in colloids [129] and low dimensional systems [130]. However, we don't observe the peak in conductivity for the 1M system, likely because velocity correlations break up more easily through interactions among ions in the more dense system.

In Fig. 3.3 we show similar results for the molten salt system at a concentration of 25.3M. We find $t_{\mathrm{N}} = 0.05$ps sufficient for the molten salt. The molten salt also exhibits deviations from Gaussian statistics but with narrow tails, signifying that fluctuations are much rarer than would be expected from its large variance and reflecting the packing constraints that inhibit large currents. The molten salt conductivity also increases and plateaus at a larger field to a value far below σ_{id}. This field dependence of the conductivity is phenomenologically known as the Onsager-Wien effect in the dilute limit [105, 109].

Decoding Molecular Correlations

In order to understand the nonlinear behaviors, we can unpack the relevant correlations using a generalized fluctuation-dissipation relationship. Specifically, we rewrite the field-dependent conductivity as an average within a nonequilibrium steady state, using the same procedure by which we arrived at Eq. 3.14, only now within a trajectory ensemble at fixed E. In this

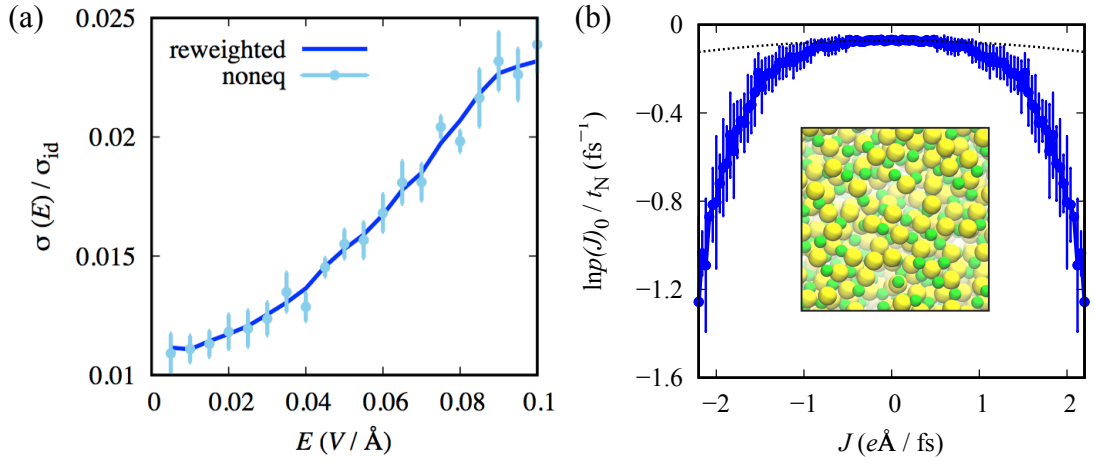

Figure 3.3: Fluctuations and response of the molten salt. (a) Field-dependent ionic conductivities relative to the Nernst-Einstein value. Lines are computed from reweighting $p(J,Q)$, and symbols are computed from finite differences of $\langle J\rangle_E$ versus E. Errorbars are one standard deviation of the mean. (b) Log-probability of the time averaged current computed from histogram reweighting. Errorbars are one standard deviation of the mean as computed from bootstrapping analysis. The dashed lines represent Gaussian distributions fitted using the data $|J| \leq 1e\mathring{A}$/fs. (Inset) Snapshot of the simulated system, with green and yellow spheres representing Na^+ and Cl^- respectively.

case, the differential response of the current to an applied field is

$$\sigma(E) = \lim_{t_N\to\infty} \frac{\beta t_N}{2V} \left\langle (\delta J)^2 + \delta J \delta Q \right\rangle_E = \frac{\beta}{V} \int_0^\infty dt\, G_E(t)\,, \tag{3.15}$$

where $G_E(t) = C_{jj}(t) + C_{jq}(t)$, $C_{jj}(t) = \langle \delta j(0)\delta j(t)\rangle_E$, $C_{jq}(t) = \frac{1}{2}\langle \delta j(0)\delta q(t) + \delta j(0)\delta q(-t)\rangle_E$. The conductivity away from equilibrium is a sum of the integrated microscopic current-current correlation function and the integrated microscopic current-frenesy correlation function.

Fig. 3.4(a) shows the total time-correlation functions for the conductivity, for both the electrolytes and the molten salt with and without an applied field. In the absence of an applied field, the only nonvanishing contribution to $G_E(t)$ is the current-current correlation function. For all systems, current correlations decay within 1ps, and exhibit recoil effects evident in transient negative correlations, which are spread over a broader range of timescales for the molten salt. The negative correlations are ionic relaxation effects that result from ion displacements that transiently distort the local electrostatic environment and generate a restoring force on the displaced ion from the compensating ionic cloud left behind [113, 131, 132]. At high fields, this negative correlation is suppressed, resulting in a larger integrated value of the correlation function, hence larger conductivity. While the time-correlation functions in principle depend on the frictions in the Langevin thermostat, for the small values

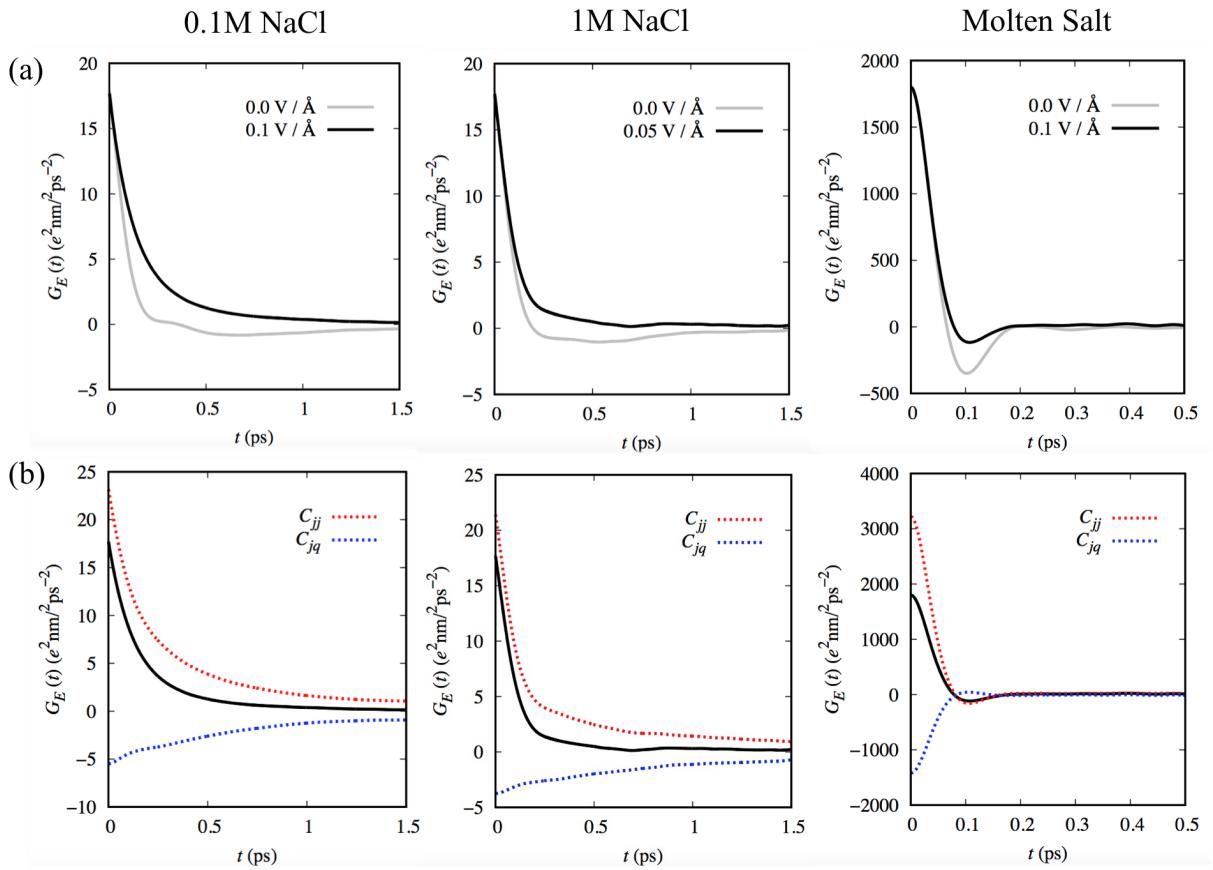

Figure 3.4: Time-correlation functions $G_E(t) = C_{jj}(t) + C_{jq}(t)$ for the field-dependent conductivity of 0.1M NaCl with $\epsilon_s = 10$ (left), 1M NaCl with $\epsilon_s = 10$ (middle), and molten salt (right). (a) Correlation functions for zero and finite fields. (b) Decomposition of $G_E(t)$ into current-current $C_{jj}(t)$ and current-frenesy $C_{jq}(t)$ correlations at $E = 0.1$V/Å for 0.1M NaCl and molten salt, and $E = 0.05$V/Å for 1M NaCl. The solid lines in (b) are $G_E(t)$.

employed here, the current is independent of the friction and the frenesy depends on the friction only though the explicit factors of ζ_i in Eq. 3.9.

In Fig. 3.4(b) we show the decomposition of $G_E(t)$ into the current-current and current-frenesy correlation functions under finite applied fields. For all systems, the former decays slower at high fields than at $E = 0$ and accounts for the largest contribution to the $G_E(t)$ integrand. For the electrolytes, positive contributions to the current-current correlation function between unlike charges give rise to the shallow maximum at intermediate fields. These correlations are expected to be quenched out by momentum transfer to an explicit solvent. The current-frenesy correlations are negative and the dominant contribution to the frenesy is the total charge weighted force, which directly manifests the depression of the

conductivity due to ionic correlations. The magnitude of the correlations in the molten salt are larger than the more dilute electrolytes, reflecting its size extensive definition. The decay in the correlation function for the molten salt is nearly ten times faster, manifesting the higher density. For higher dielectric constant systems, the current-frenesy correlations are negligible, signifying the lack of ion correlations, and as a result, time-correlation functions are independent of fields.

In the dilute solution limit, Onsager provided a theory for the field-dependent conductivity that relies on approximating the distortion of the pair correlation functions in the presence of an applied field [105]. In order to understand the structural origins of these dynamical effects and make contact with the previous work by Onsager, we can relate the field-dependent conductivity to the change in the static ion correlations. Within the steady state, we can rearrange the equation of motion in Eq. 3.1 and insert it into Eq. 3.8. This yields the average current density in the direction of the field,

$$\frac{\langle J \rangle_E}{V} = \sigma_{\rm id} E + \sum_{i=c,a} \frac{N_i}{V} \frac{z_i}{\zeta_i} \left\langle F_i \left(\mathbf{r}^N \right) \right\rangle_E \,, \tag{3.16}$$

which is given by a sum of the Nernst-Einstein conductivity times the applied field, and a correlated contribution from the sum of the average force acting on ions weighted by their charge. We can express the average force in the direction of the finite field, with unit vector $\hat{\mathbf{x}}$, as

$$\left\langle F_i \left(\mathbf{r}^N \right) \right\rangle_E = \sum_{j=c,a} \int d\mathbf{r} \, \rho_j g_{i,j}(\mathbf{r}|E) \, \hat{\mathbf{x}} \cdot \mathbf{F}^{(2)}_{i,j}(\mathbf{r}) \,, \tag{3.17}$$

where ρ_j is the number density of the jth ion type, and we have introduced the pair distribution functions $g_{i,j}(\mathbf{r}|E)$ and the pairwise decomposable force, $\mathbf{F}^{(2)}_{i,j}$, between ions of type i and j. The pair distribution function is defined as an average within the nonequilibrium steady state

$$g_{i,j}(\mathbf{r}|E) = \frac{1}{\rho_i \rho_j} \left\langle \sum_{k \in N_i, l \in N_j} \delta(\mathbf{r}_k) \delta(\mathbf{r} - \mathbf{r}_l) \right\rangle_E \,, \tag{3.18}$$

normalized by the product of the densities of i and j. In the original Onsager treatment, Eq. 3.16 is assumed to have the form, $\langle J \rangle_E / V = [\sigma_{\rm id} + \Delta\sigma(E)]E$, where $\Delta\sigma(E)$ is the correlated contribution to the conductivity computable from the knowledge of how the pair distribution function changes with applied field.

Shown in Fig. 3.5(a) are the pair distribution functions between Na^+ and Cl^- for 0.1M and $\epsilon_s = 10$, and in Fig. 3.5(b) for the molten salt, as a function of increasing applied field. In the presence of the field, the correlations deviate from spherical symmetry. As a consequence, we plot $g_{i,j}(\mathbf{r}|E)$ as a function of distance in direction of the applied field x, and orthogonal radial coordinate r, as the correlations do retain cylindrical symmetry. With increasing field, the correlations distort away from spherical symmetry, polarizing in the direction of the applied field. This is more evident in the dilute solution compared to the molten salt. At

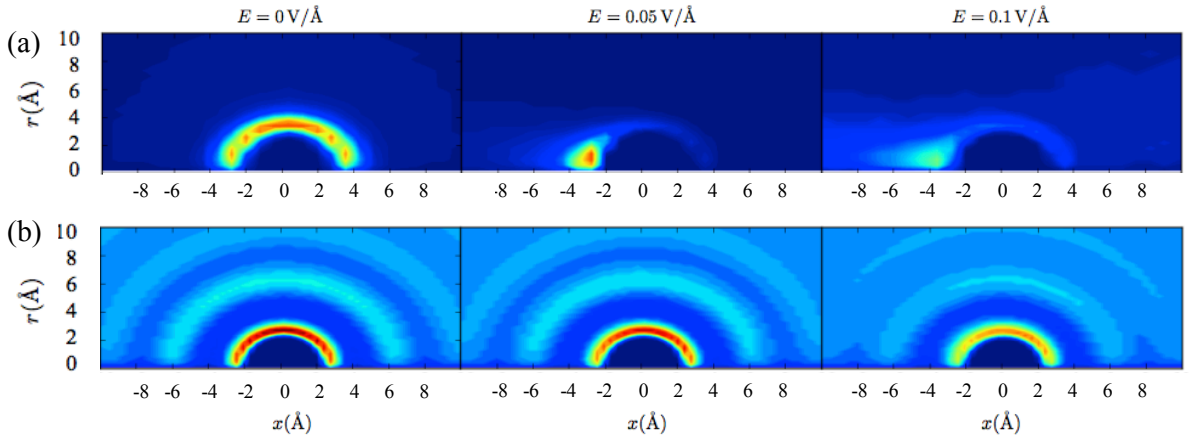

Figure 3.5: Pair distribution functions $g_{a,c}(\mathbf{r}|E)$, between Cl^- and Na^+ with increasing field, in the cylindrical coordinates for the (a) dilute solution at 0.1M, $\epsilon_s = 10$ and (b) molten salt.

large applied fields, the amplitude of the correlations decrease dramatically for the dilute solution, clarifying the limit of uncorrelated motion noted in Fig. 3.5(b). Within the molten salt correlations persist as even large fields are insufficient to mitigate packing constraints. From Eq. 3.16, these persistent density correlations result in a non-vanishing friction that depress the conductivity below σ_{id}.

3.3 Explicit Solvent Model [3]

While we have illustrated how to construct the reweighting and interpret nonlinear behaviors for an implicit model of NaCl solution, we focus on an explicit model in this section, where water molecules are represented explicitly. We highlight the subtlety arised in the reweighting procedure, and discuss the differences in the physical behaviors of the model.

Model System Description

Consider an electrolyte solution of NaCl of N species, composed of N_a anions, N_c cations and N_w water molecules in a volume V and fixed temperature $T = 300$K. As before, he species' positions and velocities are denoted $\mathbf{r}^N = \{\mathbf{r}_1, \mathbf{r}_2, \ldots, \mathbf{r}_N\}$ and $\mathbf{v}^N = \{\mathbf{v}_1, \mathbf{v}_2, \ldots, \mathbf{v}_N\}$, respectively. These variables evolve according to the same underdamped Langevin equation as in Eq. 3.1, where the first $N_{\text{i}} = N_a + N_c$ labels $i = 1, \cdots, N_{\text{i}}$ correspond to the ions, and the rest $i = N_{\text{i}} + 1, \cdots, N$ are reserved for the water molecules. The relaxation time is

[3]Most of the content of this section was originally written by the author for the following publication: D. Lesnicki, C. Y. Gao, D. T. Limmer and B. Rotenberg, "On the Molecular Correlations that Result in Field-dependent Conductivities in Electrolyte Solutions", *arXiv: 2103.13907*.

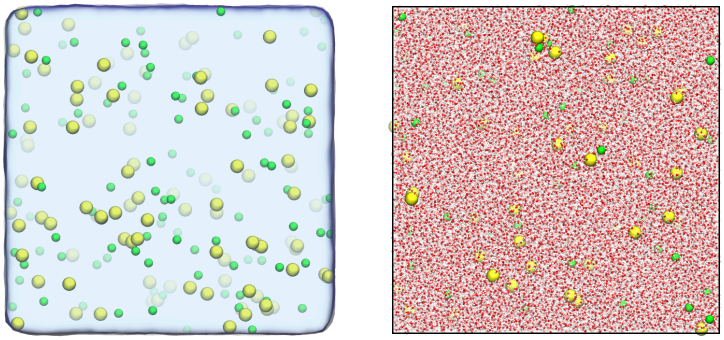

Figure 3.6: Characteristic snapshots of NaCl solutions from the molecular dynamics simulations with implicit (left) and explicit (right) solvent.

$\tau = 1000$fs for all species. The pairwise interaction potential U_{ij} consists LJ plus electrostatic terms such that

$$U_{ij} = 4\epsilon_{ij}\left[\left(\frac{\sigma_{ij}}{r_{ij}}\right)^{12} - \left(\frac{\sigma_{ij}}{r_{ij}}\right)^{6}\right] + \frac{1}{4\pi\epsilon_0}\frac{q_i q_j}{r_{ij}}\,, \tag{3.19}$$

where q_i and q_j are the charges on sites i and j, r_{ij} is the site-site separation, σ_{ij} and ϵ_{ij} are the LJ length and energy parameters, and ϵ_0 is the permittivity of free space. The LJ parameters for Na^+ and Cl^- are chosen the same as in the implicit model, while the water molecules are modeled with q-TIP4P/F model [133]. The usual Lorenz-Berthelot combining rules, $\sigma_{ij} = (\sigma_i + \sigma_j)/2$ and $\epsilon_{ij} = (\epsilon_i \epsilon_j)^{1/2}$, were used to calculate the LJ interactions.

In order to compare the solvent conditions, we also considered a system with an implicit solvent as in Section 3.2 with dielectric constants $\epsilon_s = 60$ of the corresponding water model. The frictions corresponding to the diffusion coefficients calculated for the ions at infinite dilution in the explicit solution are $\zeta_i = m_i/\tau_i$ with relaxation times $\tau_c = 10.1$fs and $\tau_a = 21.3$fs, for the cations and anions with masses $m_c = 22.99$ a.m.u. and $m_a = 35.45$ a.m.u., respectively.

Simulations are performed for 100 ion pairs and 55508 (5540) water molecules for the 0.1M (1M) solution, using the LAMMPS code [134] with a modified Langevin thermostat to ensure a Gaussian distribution of the noise. Snapshots of the systems are shown in Fig. 3.6. Results for the conductivity are obtained from a series of 1ns nonequilibrium simulations for finite fields between 0 and 0.1V/Å, in steps of 0.01V/Å, with statistical error estimated from bootstrapping, while those for temporal correlations are obtained from 10 independent 10ns trajectories.

Reweighting Formalism

As in the implicit model, the stochastic action can be constructed by comparing the ratio of the probability to observe a trajectory with and without a perturbing field. The flexible water model employed allows for independent noises to act on each atom in the water molecule,

while a rigid model would color the noise due to the imposed geometric constraint. For generality and for utility in subsequent analysis, we consider different perturbing fields with magnitudes, $\mathbf{E} = \{E_{\rm i}, E_{\rm w}\}$ for the ions and water, respectively. As before, we take the field along one Cartesian direction so that the relative action depends only on these magnitudes. We further introduce the notation $\mathbf{E}^{(\mathbf{2})} = \{E_{\rm i}^2, E_{\rm w}^2\}$. The stochastic action, decomposed according to symmetry under time reversal, is then

$$\frac{\Delta \mathcal{U}_{\mathbf{E}}}{t_{\rm N}} = \frac{1}{2}[\mathbf{J} + \mathbf{Q}] \cdot \mathbf{E} - \frac{1}{4} \boldsymbol{N\lambda} \cdot \mathbf{E}^{(2)} \,, \tag{3.20}$$

which now depends on components of the currents $\mathbf{J} = \{J_{\rm i}, J_{\rm w}\}$, and excess frenesy $\mathbf{Q} = \{Q_{\rm i}, Q_{\rm w}\}$, and vector $\boldsymbol{N\lambda} = \{N_{\rm a}\lambda_a + N_{\rm c}\lambda_c, N_{\rm w}\lambda_{\rm w}\}$ from the ions and the water, respectively. The definition of the dynamical variables are similar to the implicit model, while the subscripts indicate which species are included in the definition. For example, for the time reversal asymmetric part,

$$\begin{aligned} J_{\rm i}[\tilde{x}(t_{\rm N})] &= \frac{1}{t_{\rm N}} \int_0^{t_{\rm N}} dt\, j_{\rm i}(t) \,, \quad j_{\rm i}(t) = \sum_{i=1}^{N_{\rm i}} z_i v_i(t) \,, \\ J_{\rm w}[\tilde{x}(t_{\rm N})] &= \frac{1}{t_{\rm N} N} \int_0^{t_{\rm N}} dt\, j_{\rm w}(t) \,, \quad j_{\rm w}(t) = \sum_{i=N_{\rm i}+1}^{N} z_i v_i(t) \,, \end{aligned} \tag{3.21}$$

and similarly for the symmetric part $Q_{\rm i}$ and $Q_{\rm w}$.

With the relative measure between trajectory ensembles defined in Eq. 3.6, we can relate nonequilibrium trajectory averages in the presence of the field, to equilibrium trajectory averages without the field. Following the derivation in Chapter 2 (Eq. 2.33), the ionic current can be expressed as

$$\langle J_{\rm i} \rangle_E = \frac{\left\langle J_{\rm i} e^{\beta t_{\rm N} [\mathbf{J}+\mathbf{Q}]\cdot\mathbf{E}/2} \right\rangle_0}{\left\langle e^{\beta t_{\rm N} [\mathbf{J}+\mathbf{Q}]\cdot\mathbf{E}/2} \right\rangle_0} \,, \tag{3.22}$$

where the joint equilibrium distribution can be obtained by reweighting the nonequilibrium counterpart $p_E(\mathbf{J}, \mathbf{Q}) = \langle \delta(J_{\rm i} - J_{\rm i}[\tilde{x}(t_{\rm N})], Q_{\rm i} - Q_{\rm i}[\tilde{x}(t_{\rm N})], J_{\rm w} - J_{\rm w}[\tilde{x}(t_{\rm N})], Q_{\rm w} - Q_{\rm w}[\tilde{x}(t_{\rm N})]) \rangle_E$ according to the equation

$$\frac{\ln p_0(\mathbf{J}, \mathbf{Q})}{t_{\rm N}} = \frac{\ln p_E(\mathbf{J}, \mathbf{Q})}{t_{\rm N}} - \beta(\mathbf{J} + \mathbf{Q}) \cdot \frac{\mathbf{E}}{2} + \frac{\beta}{4} \boldsymbol{N\lambda} \cdot \mathbf{E}^{(2)} \,. \tag{3.23}$$

Note that in Eq. 3.22, the dynamical quantities of water are coupled with the ions through the relative action. Even for observables that depend only on a subset of degrees of freedom, like those of the ions, the exponential bias correlates them with the entire set of degrees of freedom in the system.

A practical difficulty arises in applying Eq. 3.23 straightforwardly. As $\mathbf{J}$ and $\mathbf{Q}$ are both extensive variables in particle number and observation time, when both are large, $p_E(\mathbf{J}, \mathbf{Q})$ becomes exponentially peaked about its most typical values, and the reweighting factors

become large enough that it is difficult to represent them numerically. This makes performing the reweighting cumbersome. A solution is found for observables that depend only on the ion degrees of freedom, by treating the contribution to the reweighting factor from the water approximately. An accurate approximation can be found by first writing the joint distribution using Bayes theorem,

$$\begin{aligned} p_E(\mathbf{J},\mathbf{Q}) &= p_E(J_\mathrm{i},Q_\mathrm{i}|J_\mathrm{w},Q_\mathrm{w})p_E(J_\mathrm{w},Q_\mathrm{w}) \\ &= p_E(J_\mathrm{i},Q_\mathrm{i}|J_\mathrm{w},Q_\mathrm{w})\exp[-t_\mathrm{N}N_\mathrm{w}I_E(\bar{j}_\mathrm{w},\bar{q}_\mathrm{w})]\,, \end{aligned} \tag{3.24}$$

where the first term on the right hand side is a conditional probability, and in the second line $I_E(\bar{j}_\mathrm{w},\bar{q}_\mathrm{w})$ is the rate function for intensive variables $\bar{j}_\mathrm{w} = J_\mathrm{w}/N_\mathrm{w}$ and $\bar{q}_\mathrm{w} = Q_\mathrm{w}/N_\mathrm{w}$. The form of the marginal distribution of the water variables is known as a large deviation form, and holds in the limit of large number of particles and observation time. Under the assumption that the joint distribution $I_E(\bar{j}_\mathrm{w},\bar{q}_\mathrm{w})$ is peaked in $(\bar{j}_\mathrm{w},\bar{q}_\mathrm{w})$, we use a saddle point approximation to evaluate their contribution to the reweighting factors in Eq. 3.22. For the marginal distribution of the ion variables $p_0(J_\mathrm{i},Q_\mathrm{i})$ this leads to an approximate reweighting,

$$\ln p_0(J_\mathrm{i},Q_\mathrm{i}) \approx \ln p_E[J_\mathrm{i},Q_\mathrm{i}|j^*_\mathrm{w}(E_\mathrm{w}),q^*_\mathrm{w}(E_\mathrm{w})] - \beta t_\mathrm{N}(J_\mathrm{i}+Q_\mathrm{i})\frac{E_\mathrm{i}}{2} - \mathcal{N}(E_\mathrm{i},E_\mathrm{w})\,, \tag{3.25}$$

where $[j^*_\mathrm{w}(E),q^*_\mathrm{w}(E)]$ denotes the maximizer

$$[j^*_\mathrm{w}(E),q^*_\mathrm{w}(E)] = \underset{(\bar{j}_\mathrm{w},\bar{q}_\mathrm{w})}{\mathrm{argmin}}\left\{\, I_E(\bar{j}_\mathrm{w},\bar{q}_\mathrm{w}) + \beta(\bar{j}_\mathrm{w}+\bar{q}_\mathrm{w})E/2\right\}\,, \tag{3.26}$$

and the normalization constant $\mathcal{N}(E_\mathrm{i},E_\mathrm{w})$ becomes

$$\mathcal{N} = N_\mathrm{w}I_{E_\mathrm{w}}(j^*_\mathrm{w},q^*_\mathrm{w}) + \frac{\beta}{2}N_\mathrm{w}t_\mathrm{N}(j^*_\mathrm{w}+q^*_\mathrm{w})E_\mathrm{w} - \frac{\beta}{4}t_\mathrm{N}\boldsymbol{\mathcal{N}\lambda}\cdot\mathbf{E}^{(2)}\,, \tag{3.27}$$

which depends only on the applied external fields, not on any fluctuating variables.

We use this approximate expression for the reweighting procedure in the results presented below. As the extensive dynamical variables related to water molecules are usually larger in magnitude compared to the ions by an order of magnitude, due to $N_\mathrm{w} \gg N_\mathrm{i}$, this expression greatly reduces numerical issues in dealing with the exponential of very large numbers. Note that when the rate function $I_E(\bar{j}_\mathrm{w},\bar{q}_\mathrm{w})$ is quadratic, or the ions and water are uncorrelated, this approximation is exact. Outside of those regimes, we still find it admits a faithful approximation to the exact reweighting relation in Eq. 3.23, especially when using additional fields to reconstruct $\ln p_0(J_\mathrm{i},Q_\mathrm{i})$ far into the tails of the distribution.

To compute the ionic conductivity, one simply needs to perform a differentiation. We first consider the physical condition where the same field $E_i = E_w = E$ is applied on the whole system. The ionic conductivity defined as $\sigma(E) = (1/V)d\langle J_\mathrm{i}\rangle_E/dE$ can be rewritten as

$$\sigma(E) = \lim_{t_\mathrm{N}\to\infty}\frac{\beta t_\mathrm{N}}{2V}\left\langle\left((\delta J_\mathrm{i})^2 + \delta J_\mathrm{i}\delta Q_\mathrm{i} + \delta J_\mathrm{i}\delta J_\mathrm{w} + \delta J_\mathrm{i}\delta Q_\mathrm{w}\right)e^{\beta\Delta\mathcal{U}_\mathbf{E}[\mathbf{X}(t_\mathrm{N})]}\right\rangle_0\,, \tag{3.28}$$

which includes both the self-correlations among the ions, and the cross-correlations between ions and water molecules. This becomes evident upon a Taylor expansion on Eq. 3.28,

$$\begin{aligned}\sigma(E) = \frac{\beta t_{\mathrm{N}}}{2V}\left(\left\langle J_{\mathrm{i}}^2\right\rangle_0 + \langle J_{\mathrm{i}} J_{\mathrm{w}}\rangle_0\right) + \frac{3\beta^3 t_{\mathrm{N}}^3}{8V}\Bigg(&\frac{1}{6}\left\langle J_{\mathrm{i}}^4\right\rangle_0 - \frac{1}{2}\left\langle J_{\mathrm{i}}^2\right\rangle_0^2 + \frac{1}{2}\left\langle \delta(J_{\mathrm{i}}^2)\delta(Q_{\mathrm{i}}^2)\right\rangle_0 \\ &+ \frac{1}{2}\left\langle J_{\mathrm{i}}^3 J_{\mathrm{w}}\right\rangle_0 - \frac{3}{2}\langle J_{\mathrm{i}} J_{\mathrm{w}}\rangle_0\left\langle J_{\mathrm{i}}^2\right\rangle_0 + \left\langle \delta(J_{\mathrm{i}}^2)\delta(Q_{\mathrm{i}} Q_{\mathrm{w}})\right\rangle_0 \\ &+ \frac{1}{2}\left\langle \delta(J_{\mathrm{i}} J_{\mathrm{w}})\delta(Q_{\mathrm{i}}^2)\right\rangle_0 + \frac{1}{2}\left\langle \delta(J_{\mathrm{i}}^2)\delta(J_{\mathrm{w}}^2)\right)\right\rangle_0 - \langle J_{\mathrm{i}} J_{\mathrm{w}}\rangle_0^2 \\ &+ \frac{1}{2}\left\langle \delta(J_{\mathrm{i}}^2)\delta(Q_{\mathrm{w}}^2)\right\rangle_0 + \langle \delta(J_{\mathrm{i}} J_{\mathrm{w}})\delta(Q_{\mathrm{i}} Q_{\mathrm{w}})\rangle_0 + \frac{1}{6}\left\langle J_{\mathrm{i}} J_{\mathrm{w}}^3\right\rangle_0 \\ &- \frac{1}{2}\langle J_{\mathrm{i}} J_{\mathrm{w}}\rangle_0\left\langle J_{\mathrm{i}}^2\right\rangle_0 + \frac{1}{2}\left\langle \delta(J_{\mathrm{i}} J_{\mathrm{w}})\delta(Q_{\mathrm{w}}^2)\right\rangle_0\Bigg) E^2 + O(E^4)\,,\end{aligned} \tag{3.29}$$

where time reversal and spatial symmetry are invoked to eliminate terms of zero value.

Alternatively, one can construct an artificial perturbation where $E_i = E$, $E_w = 0$, i.e. the external field is only applied to the ions. While this condition is not physical, its utility is illustrated in the expression for ionic conductivity,

$$\tilde{\sigma}(E) = \lim_{t_{\mathrm{N}}\to\infty} \frac{\beta t_{\mathrm{N}}}{2V}\left\langle \left((\delta J_{\mathrm{i}})^2 + \delta J_{\mathrm{i}}\delta Q_{\mathrm{i}}\right) e^{\beta\Delta\mathcal{U}_{\mathbf{E}}[\mathbf{X}(t_{\mathrm{N}})]}\right\rangle_0\,, \tag{3.30}$$

where compared to Eq. 3.28, all the cross-correlations between the ions and the water disappear in the Taylor expansion,

$$\tilde{\sigma}(E) = \frac{\beta t_{\mathrm{N}}}{2V}\left\langle J_{\mathrm{i}}^2\right\rangle_0 + \frac{3\beta^3 t_{\mathrm{N}}^3}{8V}\left(\frac{1}{6}\left\langle J_{\mathrm{i}}^4\right\rangle_0 - \frac{1}{2}\left\langle J_{\mathrm{i}}^2\right\rangle_0^2 + \frac{1}{2}\left\langle \delta(J_{\mathrm{i}}^2)\delta(Q_{\mathrm{i}}^2)\right\rangle_0\right) E^2 + O(E^4)\,. \tag{3.31}$$

Thus by comparing the conductivity under the two scenarios, we can obtain an estimate of the contribution from ion-water correlation, which is not readily extracted from the implicit model.

Shown in Fig. 3.7 are the field-dependent conductivities of the explicit solvent system at two concentrations, 0.1M and 1M. The reweighted results for both are computed from Eq. 3.25 using $t_{\mathrm{N}} = 10$fs, which is long enough to justify the saddle point approximation and converge the mean reweighted current. Specifically, we first constructed $p_0(J_{\mathrm{i}}, Q_{\mathrm{i}})$ using a series of simulations at finite fields at the locations of the direct estimate in Fig. 3.7, and then use the generalized version of WHAM to stitch joint histograms of J_{i} and Q_{i} together. Additionally, we have computed the conductivity from a numerical derivative of the average current directly from a set of simulations at fixed field. While the two estimates are in good quantitative agreement, the statistical errors are much smaller for the reweighted results, as data across the whole fields are supplemented in each estimate. We also compare the explicit model with the implicit model with corresponding parameters in Fig. 3.7(a), where the conductivity agrees with the Nernst-Einstein limit, consistent with the results shown in Section 3.2 for the high dielectric system.

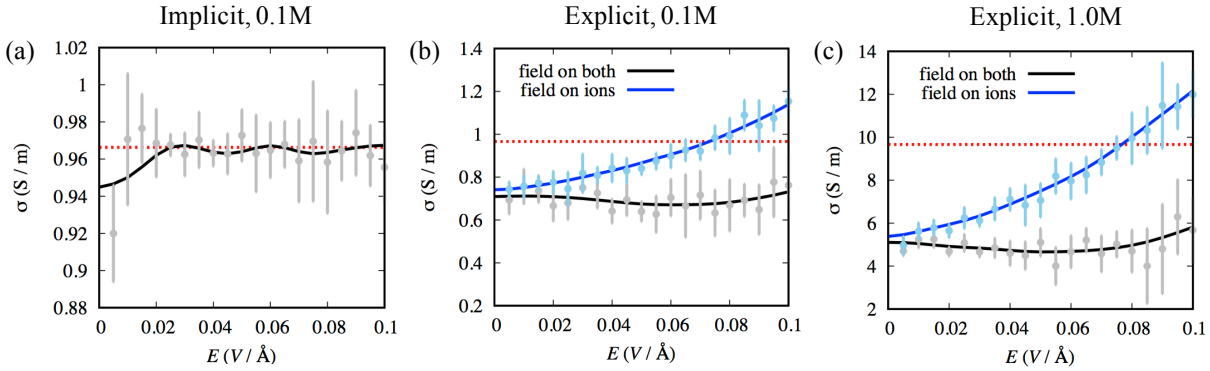

Figure 3.7: Field-dependent ionic conductivities for the implicit model at (a) 0.1M, explicit model at (b) 0.1M and (c) 1M. Lines are computed from reweighting $p(J, Q)$, and symbols are computed from finite differences of $\langle J \rangle_E$ versus E. Errorbars are one standard deviation of the mean. In the explicit models we compare the case where an external field is applied on both the ions and water (black), and only applied on the ions (blue). The red dashed lines correspond to the Nernst-Einstein conductivities σ_{id} (Eq. 3.10).

We find that the conductivity in the explicit models is only weakly dependent on the field and the curve is well fitted by a polynomial with a positive fourth order and a negative second order term. The curves for the two different concentrations, 0.1M and 1M are remarkably similar, though the latter exhibits a consistently lower conductivity. The conductivity at zero field for both concentrations is suppressed relative to its value at infinite dilution, or compared to its implicit solvent value.

From the ensemble reweighting theory presented earlier, we have a means of decoupling the contributions to the field-dependent conductivity from the solvent and those from the ions. Specifically, we can use a generalized ensemble where only a field is applied to the ions, not the water, to deduce which correlations suppress the field dependence that result directly from the water. When the field is only applied on the ions for both concentrations, the conductivity grows quadratically with a large positive second order term. This is shown in Fig. 3.7. The drastic difference between these two sets of results can be unravelled by a comparison between the generalized fluctuation-dissipation relationships in Eq. 3.29 and Eq. 3.31, where all cross-correlations between the ions and water are absent from the latter expression. More specifically, the lower conductivity at zero field when the field is applied on both the ions and water is a direct result of negative correlations in $\langle J_{\text{i}} J_{\text{w}} \rangle_0$ at equilibrium. The negative second order coefficient results from the negative fourth order correlations between ions and water, among which the dominant term is $\langle \delta(J_{\text{i}}^2) \delta(Q_{\text{w}}^2) \rangle_0$ due to the larger number of water molecules and subsequently larger fluctuations in Q_{w}.

While the ionic conductivity under the moderate field considered in Fig. 3.7 is weakly field-dependent, it does eventually grow quadratically under very high fields as shown in Fig. 3.8. The conductivity is found to exceed the Nernst-Einstein limit for free ions. However, this

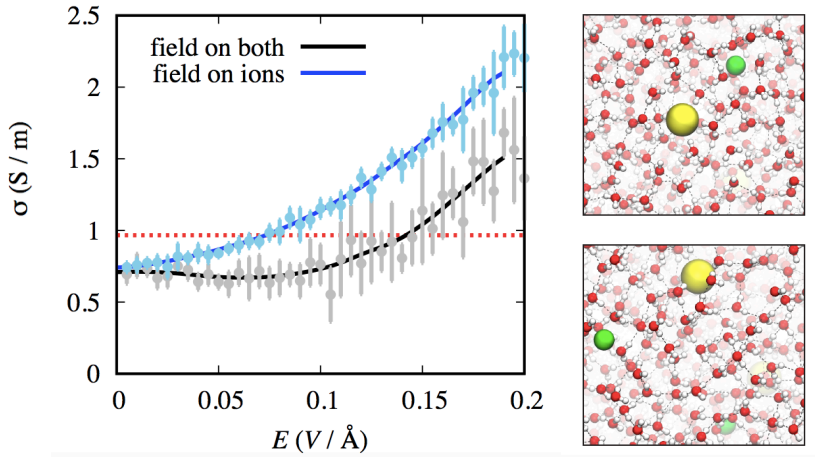

Figure 3.8: (left) High field behavior of 0.1M, explicit solvent system in an ensemble with the field on both the water and the ions, $E_{\rm i} = E_{\rm w} = E$ (black) or just on the ions $E_{\rm i} = E$ and $E_{\rm w} = 0$ (blue). Lines are computed from reweighting $p_0(J, Q)$, and symbols are computed from finite differences of $\langle J \rangle_E$ versus E. Errorbars are one standard deviation of the mean. The red dashed line corresponds to the Nernst-Einstein conductivity $\sigma_{\rm id}$. (right) Charactoristic snapshots from the molecular dynamics simulations at $E = 0$ (top) and $E = 0.15$V/Å (bottom).

behavior is unphysical. Under fields higher than $E = 0.1$V/Å in our molecular simulations, we find that the dipoles of the water molecule all align with the high field, restraining dipole fluctuations, and leading to dielectric breakdown. Further, water molecules will start to spontaneously dissociate at such high fields [135], which is not allowed due to the constraints on water molecules in our model.

Decoding Molecular Correlations

To gain more physical insight into the relevant correlations, we rewrite the equation for the conductivity using time integrated correlation functions

$$\begin{aligned}\sigma(E) &= \lim_{t_{\rm N}\to\infty} \frac{\beta t_{\rm N}}{2V} \left\langle (\delta J_{\rm i})^2 + \delta J_{\rm i}\delta J_{\rm w} + \delta J_{\rm i}\delta Q_{\rm i} + \delta J_{\rm i}\delta Q_{\rm w} \right\rangle_E \\ &= \frac{\beta}{V}\int_0^\infty dt\ \left[G_J(t) + G_Q(t)\right] ,\end{aligned} \tag{3.32}$$

where $G_J(t) = C_{j_{\rm i}j_{\rm i}}(t) + C_{j_{\rm i}j_{\rm w}}(t)$, with

$$\begin{aligned}C_{j_{\rm i}j_{\rm i}}(t) &= \langle \delta j_{\rm i}(0)\delta j_{\rm i}(t)\rangle_E \ , \\ C_{j_{\rm i}j_{\rm w}}(t) &= \frac{1}{2}\left\langle \delta j_{\rm i}(0)\delta j_{\rm w}(t) + \delta j_{\rm i}(0)\delta j_{\rm w}(-t)\right\rangle_E \ ,\end{aligned} \tag{3.33}$$

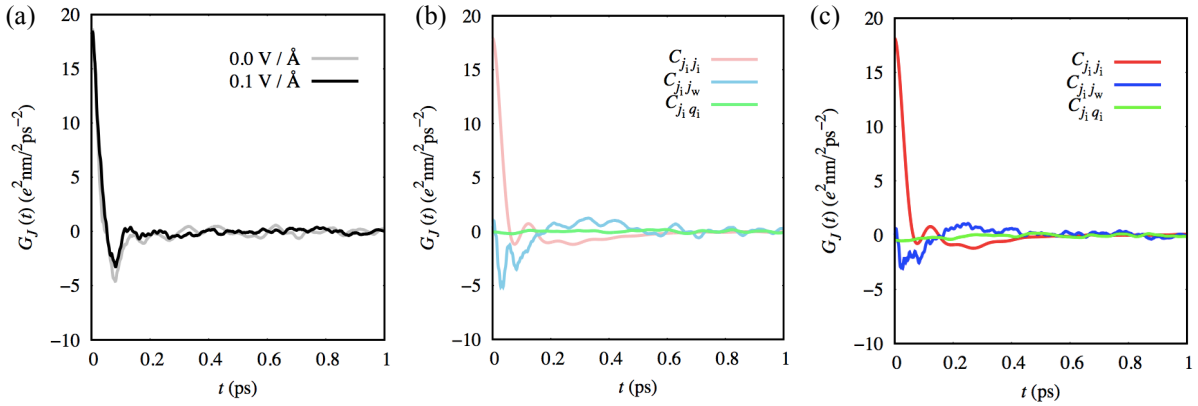

Figure 3.9: Time-correlation functions for field-dependent conductivities of 0.1M explicit solvent solution. (a) Time-correlation functions $G_J(t) = C_{j_i j_i}(t) + C_{j_i j_w}(t)$ for $E = 0$ and $E = 0.1\mathrm{V/Å}$. (b) Contributions to the conductivity from current-current and current-frenesy for $E = 0\mathrm{V/Å}$. (c) Contributions to the conductivity from current-current and current-frenesy for $E = 0.1\mathrm{V/Å}$.

and $G_Q(t) = C_{j_i q_i}(t) + C_{j_i q_w}(t)$, with

$$\begin{aligned} C_{j_i q_i}(t) &= \frac{1}{2}\left\langle \delta j_i(0)\delta q_i(t) + \delta j_i(0)\delta q_i(-t)\right\rangle_E , \\ C_{j_i q_w}(t) &= \frac{1}{2}\left\langle \delta j_i(0)\delta q_w(t) + \delta j_i(0)\delta q_w(-t)\right\rangle_E . \end{aligned} \tag{3.34}$$

The conductivity away from equilibrium is a sum of the integrated current-current correlation function, denoted by G_J, and integrated current-frenesy correlation function, denoted by G_Q. At zero field, G_Q is zero due to time reversal symmetry, leaving G_J as the only contribution to the zero-field conductivity. At finite fields when G_Q should contribute to the conductivity as well, for the concentrations studied, we find that the contribution from $C_{j_i q_i}(t)$ negligible compared to the other three terms. This is due to the screening effect of the explicit water molecules that results in the ions being largely dissociated, so that the effect of ion-ion interactions arises mainly from the relaxation of the ionic cloud rather than from ion pairing and is thus weaker than short-range ion-water interactions. The $C_{j_i q_w}(t)$ term exhibits large statistical fluctuations due to the larger number and stronger intramolecular forces of the water molecules, and is thus much more difficult to converge by brute force calculations. We have to infer its contribution from the measured conductivities using the generalized fluctuation-dissipation relationships.

Fig. 3.9 shows the current-current contribution to the response function for the 0.1M explicit system at equilibrium $E = 0$ and at a finite field $E = 0.1\mathrm{V/Å}$. Also in Fig. 3.9, the total correlation function for $E = 0$ and $E = 0.1\mathrm{V/Å}$ are decomposed into their various pieces. At zero field, both the ion-ion current self-correlation and the ion-water current cross-correlation exhibit noticeable recoil effects evident in transient negative correlations. The

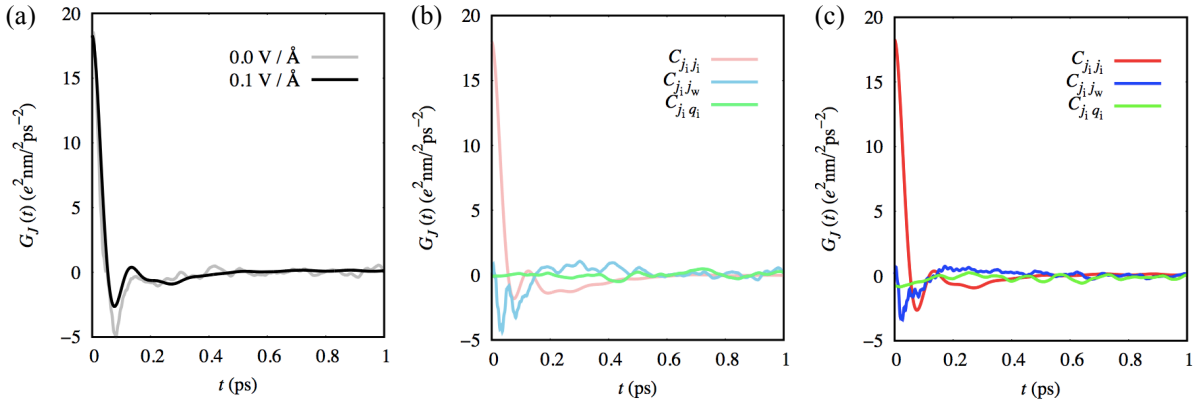

Figure 3.10: Time-correlation functions for field-dependent conductivities of 1.0M explicit solvent solution. (a) Time-correlation functions $G_J(t) = C_{j_i j_i}(t) + C_{j_i j_w}(t)$ for $E = 0$ and $E = 0.1\mathrm{V/Å}$. (b) Contributions to the conductivity from current-current and current-frenesy for $E = 0\mathrm{V/Å}$. (c) Contributions to the conductivity from current-current and current-frenesy for $E = 0.1\mathrm{V/Å}$. Throughout errorbars are one standard deviation from the mean.

former (ion-ion), which spreads over longer timescales, integrates to a positive contribution, and is the only term responsible for the zero-field conductivity when the field is only applied to the ions. The latter (ion-water) integrates to a much smaller negative contribution, which accounts for the difference between the zero-field conductivities between the two sets in Fig. 3.7. At a higher field $E = 0.1\mathrm{V/Å}$, the recoil effect in both correlations is reduced, resulting in a larger integrated value of both current-current correlation functions, and a more positive $G_J(t)$.

We can infer the large contribution from $C_{j_i q_w}(t)$ at finite field by contrasting the behavior of $\sigma(E)$ and $\tilde{\sigma}(E)$. In the case where the field is applied only on the ions, the correlation function $C_{j_i j_i}(t)$ integrates to a similarly large contribution as in the case when the field is applied to both ions and water, and one that is larger than its zero field value. As $C_{j_i j_w}(t)$ and $C_{j_i q_i}(t)$ are persistently small at $E = 0.1\mathrm{V/Å}$, the large difference between $\sigma(E)$ and $\tilde{\sigma}(E)$ must result from significant negative contributions in the current-frenesy correlation function $C_{j_i q_w}(t)$ between the ions and the water. The physical origin of this negative correlation is the relaxation effects that result from ion displacements that transiently distort the local dielectric environment and generate a restoring force on the water molecules from the compensating ionic cloud left behind. This term dominates the total correlation function and compensates the increase in the current-current correlation functions, yielding a weak dependence on field of the conductivity. Thus while the current-frenesy correlation function is difficult to compute explicitly, from the above analysis we are able to infer its effect using the decomposition of time-correlation functions.

Fig. 3.10 shows the correlation functions for the 1.0M system. Qualitatively, they are very

similar to those for the 0.1M solution. Both systems exhibit noticeable recoil effects in the current-current function due to ion-ion terms. In the 1.0M solution, the transient negative correlation is larger than in the 0.1M solution. This is also true for the current-current function due to ion-water terms. The combination of these negative correlations results in the reduced conductivity at $E = 0\text{V/Å}$. As for the small concentration, the currrent-frenesy correlations from ion-ion terms are negligible even at 0.1V/Å, and the suppressed field-dependence results from the currrent-frenesy correlations from ion-water terms.

3.4 Conclusion

In conclusion, we have leveraged recent developments in the theory of nonequilibrium systems to relate ionic conductivities to microscopic correlations under arbitrarily large electric fields and solvent conditions. We have found that both the fluctuations of the ion's displacement as well as the dynamical fluctuations of the intrinsic electric fields acting on an ion, affect the response of the ionic current to an additional external field. Considering the field-dependence of the ionic conductivity, we have shown how nonlinear relationships between an ionic current and applied electric field can emerge in weak electrolytes as ion correlations are reduced, and how they are mitigated in strong electrolytes due to persistent solvent friction. Our method works not only for strong electrolytes at low concentrations, for which approximate theories [109, 136] can accurately predict the conductivity and its field-dependence, but also for weak electrolytes or elevated concentrations where these theories break down.

This approach of reweighting nonequilibrium trajectories is general, and we expect will find use more broadly in other cases of molecular transport. It will be particularly interesting to apply these new statistical tools to investigate the nonlinear response of ionic liquids [137, 138], as well as transport near charged interfaces, such as nonlinear electrofriction on corrugated surfaces [139]. In the explicit solvent case, the present theoretical and numerical techniques also provide new opportunities to investigate coupled transport processes, such as coupled charge and mass transport in electrolytes [140], the origin of the frequency-dependent solvent friction on the ions [136, 141, 142], and electro-osmotic response. While we have considered bulk solutions of monovalent electrolytes, our approach is straightforwardly applied for multivalent ions, where nonlinear reponses due to field-induced ion pair dissociation should be more prominent, and can be extended to instances of transport in confinement [143–146], in which case generalizations of our theory may provide insight into recent experimental observations [114].

Chapter 4

Heat Transport: Thermal Rectification in 1D Nonlinear Lattice

4.1 Introduction

Heat conduction in low-dimensional materials have attracted much attention in recent years thanks to advanced experimental techniques on nanoscale materials [147–151]. Compared to bulk materials, reduced dimensionality and conservation laws give rise to unusual relaxation and transport properties. For example, low-dimensional materials exhibit anomalous heat transport behaviors, namely the breakdown of Fourier's law of heat conduction

$$J = -\kappa \nabla T \,, \tag{4.1}$$

where J is the heat flux, and ∇T the temperature gradient, which manifiests itself as a divergence of the conductivity κ in the thermodynamic limit, where the number of particles $N \to \infty$, and a slow decay of equilibrium current correlations. The limiting behavior, however, depends on the system details. For example, for a homogeneous harmonic chain, $\kappa \propto N$, indicating perfectly ballistic transport; whereas for a disordered harmonic chain with free boundary condition, $\kappa \propto N^{1/2}$. The anomalous transport behavior is a signature that the kinetics of the energy carriers is so correlated that they are able to propagate faster than in the diffusive case. It has been studied with various theoretical approaches, including the fluctuating hydrodynamics approach [152, 153], mode-coupling theory [154, 155], and kinetic theory. However, the mechanism in specific models is not entirely clear, especially in the case of nonlinear lattices.

A specific nonlinear model of particular interest in numerical and theoretical studies is the one dimensional Fermi-Pasta-Ulam-Tsingou (FPUT) chain, where neighbouring particles interact through a quadratic plus a cubic or quartic potential. It has been well-known that the FPUT chain exhibits anomalous transfer behaviors [156], and the divergence exponent $\kappa \propto N^{\alpha}$ is reported to be between 0.3 and 0.45 numerically regardless of the boundary condition [157, 158], which does not contradict with the mode coupling theory prediction $\alpha = 0.4$, or the result form fluctuating hydrodynamics $\alpha = 1/3$ [152].

The existence of solitons in nonlinear lattices was first discovered by computer simulations in the solution of the Korteweg-deVries equation [159]. The supersonic solitons have since been both numerically observed in a wide variety of lattices, and experimentally demonstrated in crystalline solids [160]. The idea that solitons may play a role in heat conduction dates back to Toda [161]. Early results from some 1D toy models suggest that the strong inhibition of coherent solition propagation in the underlying chaotic dynamics produces a normal heat conductivity independent of length [162, 163]. Later, it has been found that the temperature dependence of the velocity of solitons agrees well with the sound velocity of energy transfers [164]. The debate about whether the energy carriers in FPUT chains are solitons or effective phonons has still not been resolved yet. In addition, other nonlinear excitations such as breathers may also contribute to the heat transport in FPUT chains [164].

Apart from the anomalous heat transfer behaviors mentioned above, another type of interesting behavior has been reported in low-dimensional nonlinear materials - thermal rectification [165]. A thermal rectifier is a type of material with intrinsic structural asymmetry so that it exhibits an asymmetric heat transport response when a temperature gradient is applied. Such functional graded materials can be potential candidates for controlling the heat flow at nanoscales. This behavior has been first observed experimentally in [147], and has been modeled by mass graded nonlinear chains [166–168]. While a couple of numerical evidences exist, the problem is far from being fully understood. Indeed, some early investigations into the disordered FPUT model revealed that the simple perturbative picture in which anharmonicity and impurities provide two independent scattering mechanisms does not hold [169]. Furthermore, to our knowledge, the role of solitons in mass graded chain has not been investigated.

In this chapter, we hope to further investigate the problem of thermal rectification in mass graded FPUT chain, and provide some molecular insights into the problem. In Section 4.2 we provide a systematic study of the phenomenological behavior of thermal rectification in a mass graded FPUT model. More specifically, we study how the chain length, mass gradient, boundary condition, and average temperature affect the rectification behavior. In Section 4.3, we apply our large deviation formalism to this nonlinear transport process, and interpret the higher order transport coefficients with correlation functions. In addition, we investigate the influcence of mass gradient to solitons using the momentum excitation method, in order to give a microscopic explanation to some of the results found in Section 4.2. We end the chapter with some comments on future directions that remain to be investigated in Section 4.4.

4.2 Thermal Rectification in Mass Graded FPUT Chain

Here we model a 1D thermal rectifier using the linearly mass graded FPUT chain, which has been shown to capture thermal rectification behavior [168]. The schematic of the simulated

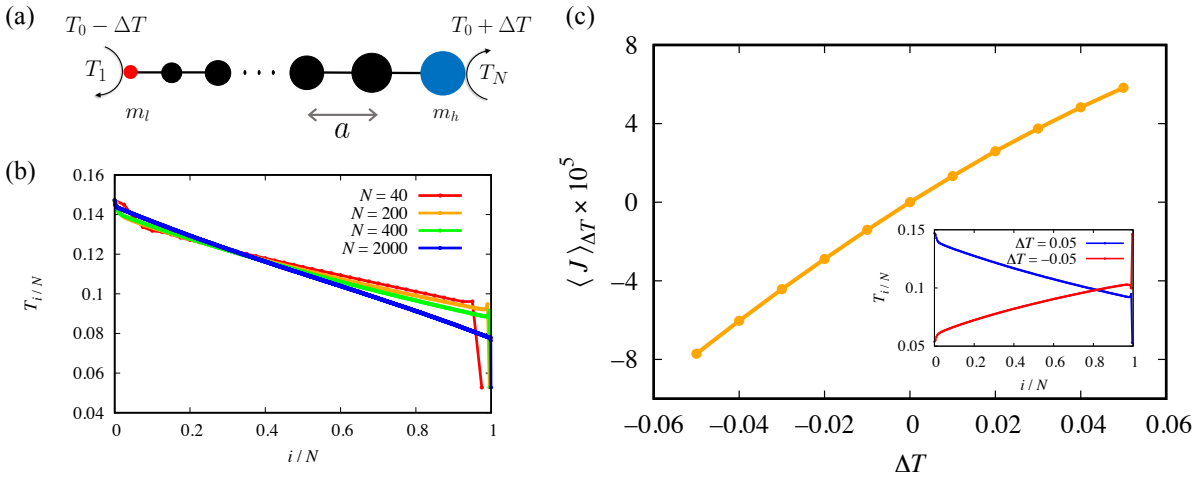

Figure 4.1: Thermal rectification behavior in a mass graded FPUT chain with $T_0 = 0.1$, $m_h/m_l = 20$, and fixed boundary condition. (a) Schematic of the simulated system. (b) Temperature profile for each particle i at $\Delta T = 0.05$ for different chain lengths. (c) Nonequilibrium current as a response to ΔT for $N = 200$. (*Inset*) Temperature profile at $\Delta T = \pm 0.05$.

system is shown in Fig. 4.1(a). The mass of the ith particle is

$$m_i = m_l + (i-1)(m_h - m_l)/(N-1), \quad i = 1, \cdots, N \tag{4.2}$$

where N is the total number of particles. The particles oscillate around their average position $b_i = ia$, while interacting with neighboring particles through the quartic FPUT potential,

$$V_{\mathrm{FPUT}}(\boldsymbol{r}) = \sum_{i=1}^{N+1} \frac{\kappa}{2}(r_i - r_{i-1} - a)^2 + \frac{c}{4}(r_i - r_{i-1} - a)^4 , \tag{4.3}$$

where κ and c are the harmonic and anharmonic coupling, and a is the lattice constant. The potential is also known as the FPUT-β potential. We differentiate between the fixed boundary condition, where two fictitious particles are fixed at b_0 and b_{N+1}, and the free boundary condition, where no such constraint is applied. We set $m_l = \kappa = a/2 = 1$, to define a dimensionless unit system, in which we also let $c = 1$. The equation of motion is integrated by the velocity Verlet algorithm with a timestep of $h = 5 \times 10^{-3}$.

To apply an external temperature gradient, we place the particles on the two ends in contact with infinitely large thermal reservoirs kept at temperatures $T_1 = T_0 + \Delta T$ and $T_N = T_0 - \Delta T$, respectively, with the average temperature T_0. This is implemented by an Andersen thermostat [67] on each of the two end particles, where the time interval Δt between successive collisions are distributed as $P(\Delta t) = \Gamma e^{-\Gamma \Delta t}$ and $\Gamma = 0.8$ is the coupling strength to the bath. Fig. 4.1(b) shows the typical temperature profiles for a range of length N, as

determined from average kinetic energy. For different chain lengths, the temperature profile does not exactly follow the scaling ansatz $T_i = T(i/N)$. A temperature jump is observed at the boundaries due to the Kapitza resistance between the system and the bath, which is much larger at the higher mass end. Thus we will get rid of the first and last quarter of the profile when computing the thermal conductivity. While a linear temperature gradient is developed for small chain length, for large N the temperature profile is nonlinear, as observed in other types of nonlinear lattices and has been explained by the Levy walk model [170, 171].

In the steady state limit, the heat current from the two ends must be same in magnitude but opposite in direction, so we define the heat current as

$$j(\tilde{x}_t) = \frac{T_0}{4}\left(m_1\dot{v}_1 v_1 - v_1 F_1^{\mathrm{FPUT}} - m_N\dot{v}_N v_N + v_N F_N^{\mathrm{FPUT}}\right) , \tag{4.4}$$

where $F_i^{\mathrm{FPUT}} = -\partial V_{\mathrm{FPUT}}(\boldsymbol{r})/\partial r_i$. This can be interpreted as the rate of change in the kinetic and potential energy, averaged over contributions from particle 1 and N, scaled by a factor of $T_0/2$. This constant factor will be convenient when we define the stochastic action in the next section. Fig. 4.1(c) shows the time averaged nonequilibrium current at different temperature gradients, which clearly exhibits asymmetric behavior due to the mass asymmetry. More specifically, under the same magnitude of the affinity, the current flowing against the mass gradient is weaker than the current flowing along the gradient. While this is partially due to the boundary effect, as seen in the temperature profiles in the inset of Fig. 4.1(c), it cannot be fully attributed to the temperature dependence of conductivity, as the average temperature is higher in the case of $\Delta T > 0$. We will explore the origin of this asymmetry in the rest of this chapter.

Length Scaling of Conductivity

Due to the jump at the boundary and the nonlinear temperature profile described above, there is some ambiguity in the definition of temperature gradient and thermal conductivity. This may not come as a surprise, as the very definition of a temperature gradient relies on the local equilibrium hypothesis, i.e. defining a local temperature for a macroscopically small but microscopically large volume at each location in space. Following conventions in the literature [172], we define the thermal gradient as $\nabla T = 2\Delta T'/aN$, where $\Delta T'$ is the temperature difference between particle $i = N/4$ and $i = 3/4N$. The conductivity obtained is thus the bulk conductivity and does not include boundary resistances, which depend on the properties of the thermostat.

In Fig. 4.2 we show a systematic study on the bulk heat conductivity at different system lengths N, average temperatures T_0, and boundary conditions. The largest system size we have studied is $N = 8000$, which is higher than most of the results reported in the literature. While for the homogeneous mass FPUT chain, the scaling exponent $\alpha \approx 0.4$ regardless of the boundary condition or the average temperature, we see that the scaling behavior seems to be sensitive to such conditions in the mass graded FPUT chain. This may not come as a surprise, as it is well known that the scaling of the conductivity depends on the boundary

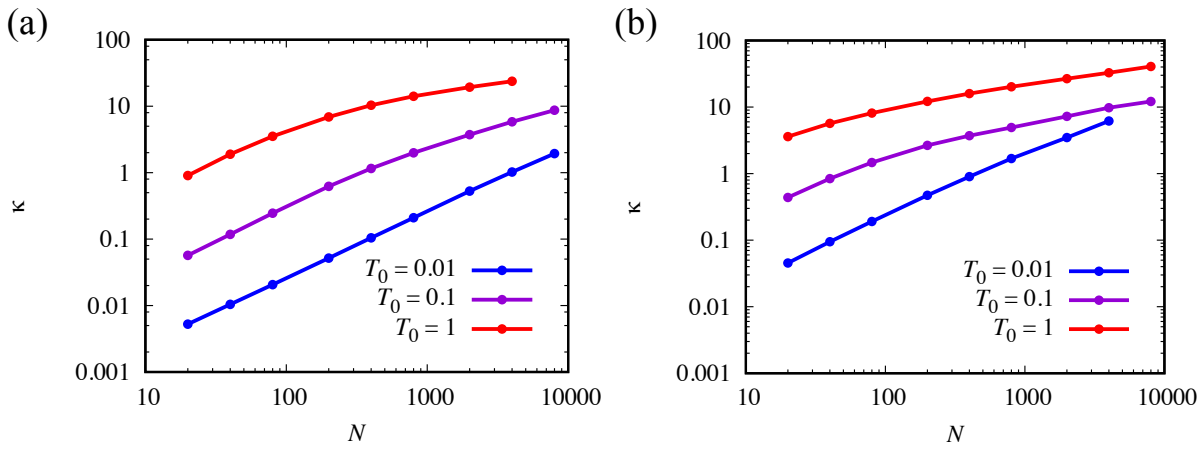

Figure 4.2: Length scaling of the bulk heat conductivity at different temperatures for the (a) fixed boundary condition, and (b) free boundary condition, with $m_h/m_l = 20$.

condition even for inhomogeneous harmonic chains. For example, in disordered harmonic chain, $\kappa \propto N^{1/2}$ for free boundaries, while with fixed boundaries $\kappa \propto N^{-1/2}$, behaving as an insulator in the thermodynamic limit. Furthermore, the value of the thermal conductivity is consistently lower for the fixed boundary case while keeping other parameters fixed, because of the constraint on thermal modes.

At the lowest temperature $T_0 = 0.01$, we observe a scaling behavior close to $\alpha = 1$ for both boundary conditions, which is quite different from the behavior at higher temperatures. This is further evidence to the fact that many anharmonic models exhibit very slow relaxation to equilibrium below a typical energy density, or temperature [173]. Indeed, it is well known from the effective phonon theory that the dependence of thermal conductivity on temperature exhibits two regimes: $\kappa(T) \propto T^{-1}$ at low temperature region and $\kappa(T) \propto T^{1/4}$ at high temperature region [174]. At a temperature as low as $T_0 = 0.01$, the anharmonicity is rarely explored by thermal fluctuations, and thus the system behaves similarly to a mass graded harmonic chain, with a transport mechanism close to ballistic [1]. However, the system must deviate from truly ballistic transport due to the mass gradient scattering. This is confirmed by the decrease in the scaling exponent at higher chain length, which is measured to be around 0.9 for fixed boundary, and 0.8 for free boundary chain, at the largest system size that we studied. Even larger system sizes need to be investigated to confirm whether the scaling exponent will further decrease and converge with the results at higher temperatures, as the mean free path of renormalized phonons is on the order of 10^5 for low frequencies ($\omega < 0.1$) at such a low temperature [175].

For the higher temperature $T_0 = 0.1$, we observe a scaling exponent $\alpha = 0.31$ for the free

[1] Note here even in the harmonic case, how the mass graded chain behaves drastically differently from the disordered chain in the scaling behavior. The effect of mass profile on thermal modes remains to be studied.

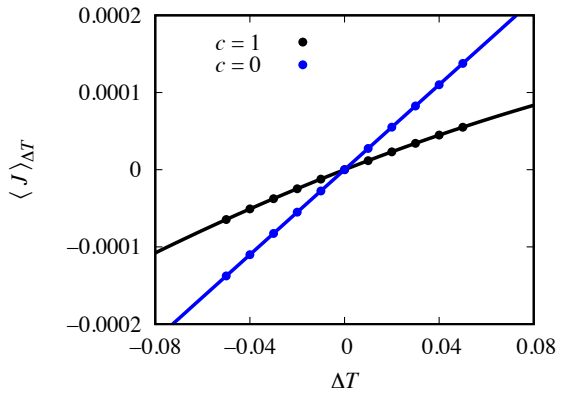

Figure 4.3: Comparison between the heat current in the mass graded nonlinear chain with $c = 1$ (black) and the harmonic chain with $c = 0$ (blue). Both chains are operating at $N = 20$, $T_0 = 0.1$, $m_h/m_l = 20$ and fixed boundary condition.

boundary condition, while the scaling exponent is $\alpha = 0.57$ for the fixed boundary condition but clearly has not converged with length yet. These results are consistent with the reported value for the uniform mass FPUT chain. At an even higher temperature $T_0 = 1$, The scaling exponent converges to $\alpha = 0.3$ for both the free and fixed boundary condition, which is consistent with the results reported in [168] even for infinitely high temperature. The faster convergence behavior is due to the higher nonlinearity strength at higher temperature, and as a result the mean free path of renormalized phonons is on the order of 10^4 ($\omega = 0.1$) for $T_0 = 0.1$, and 10^3 ($\omega = 0.1$) for $T_0 = 1$[175].

To summarize, our results suggest that while the length scaling exponent of the bulk thermal conductivity in mass graded FPUT chain may not be sensitive to boundary conditions, it is dependent on the average temperature of the chain, especially at the low temperature regime. While the exponent agrees with theoretical predictions in the high temperature limit, the results at the low temperature regime is more complicated and not conclusive yet. Our result needs to be confirmed with computations at even larger system size, especially for the fixed boundary case where the exponent converges slower with N. However, such study will of course be computationally costly, as the time required to reach the stationary state grows exponentially with N.

Effect of System Parameters

It has been reported in the literature that the thermal rectification behavior in the simulated model is very sensitive to specific parameters [168]. Indeed, it is only observable in an intermediate range of temperatures with the fixed boundary condition. Here we study these effects systematically, which is the first step to truly understand the nonlinear transport

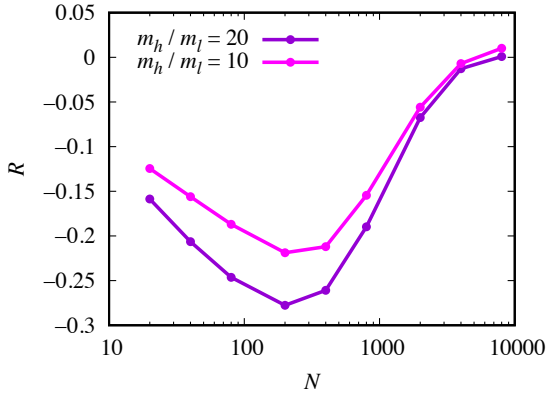

Figure 4.4: Comparison of the rectification ratio between different mass gradients, with $T_0 = 0.1$ and fixed boundary condition.

mechanism. We define the transport coefficients as

$$\langle J \rangle_{\Delta T} = L_1 \Delta T + L_2 \Delta T^2 + O(\Delta T^3)\,, \tag{4.5}$$

where L_1 is the thermal conductivity. Unlike the bulk conductivity shown in Fig. 4.2, L_1 includes both the bulk and boundary resistance. To characterize the rectification effect, we define $R = L_2 T_0 / L_1$ as the rectification ratio, as this is related to the percentage modulation of the heat current in the forward and backward direction.

One of the necessary conditions for rectification to arise is the nonlinearality of the lattice. For example, we compare the heat current in the mass graded FPUT and harmonic chain at $N = 20$, $T_0 = 0.1$, $m_h/m_l = 20$ in Fig. 4.3. While the harmonic chain has a higher thermal conductivity due to the absence of scattering from anharmonicity, it exhibits no thermal rectification behavior despite of the mass gradient.

Secondly, the mass gradient plays a crucial role as well, without which thermal rectification is absent due to the spatial symmetry. As seen in Fig. 4.4, increased mass gradients generally induces a higher rectification ratio. The presence of inhomogeneous mass generally induces localization of the normal modes of the chain, especially in high-frequency modes, as shown in disordered harmonic systems. Even in the case of generic disordered chain, while the dynamics is statistically invariant under spatial symmetry, the same does not hold true for each individual eigenvector [172]. The modulation of thermal modes in the presence of mass gradient remains to be studied though.

The third parameter that influence rectification is the average temperature T_0, as shown in Fig. 4.5, where rectification ratio is plotted as a function of N at different temperatures. Note that in the $N \to \infty$ limit, the mass gradient vanishes and thus the rectification ratio should also decay to zero. Therefore, the rectification ratio exhibits a peak when plotted as a function of N, while the location of the peak shifts to lower N at higher temperatures. For

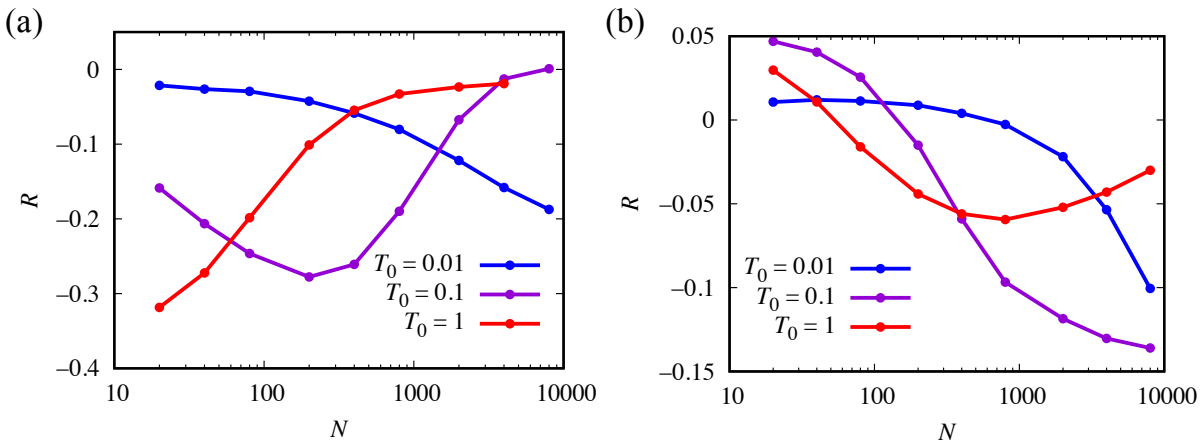

Figure 4.5: Rectification ratio at different temperatures for the (a) fixed boundary condition, and (b) free boundary condition, with $m_h/m_l = 20$.

the low temperature limit $T_0 = 0.01$, the location of the peak is at a higher N than the range plotted, which is similar to the slow convergence of the scaling exponent seen in Fig. 4.2. It is worth noting that the conclusion arrived at in [168] that rectification only happens at $T_0 = 0.1$ is based on the data for $N = 200$. This is clearly not the case taken into account the change in the system size as well. Indeed, given that the mass gradient decreases with N as well, one might say that the rectification is indeed the strongest at the lower temperature limit. Therefore, the explanation arrived there based on the mismatch of the vibrational spectra needs to be reconsidered. In particular, more investigation into the low temperature regime needs to be done to properly explain the rectification behavior.

Lastly, the boundary condition has a huge influence on the rectification, as seen in Fig. 4.5 as well. While for the free boundary condition, extended eigenmodes are allowed to exist, all eigenmodes must vanish at the boundary under fixed boundary condition. The rectification ratio for the fixed boundary condition is consistently higher than that of the free boundary condition. In the case of fixed boundary condition, all rectification ratio is negative, while for the free boundary condition, rectification ratios are positive for small chain lengths, which is most likely a boundary effect. This suggests that the major contributor to rectificaiton behavior may be very different depending on the boundary condition.

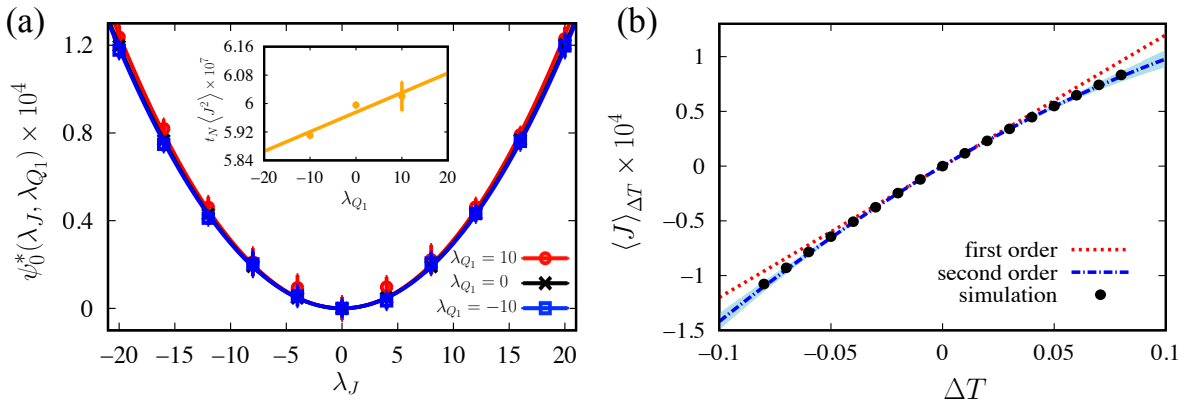

Figure 4.6: Computation of the transport coefficients from the large deviation function in a mass graded FPUT chain with $N = 20$, $T_0 = 0.1$, $m_h/m_l = 20$, and fixed boundary condition. (a) The shifted LDF $\psi_0^*(\lambda_J, \lambda_{Q_1})$ at $\lambda_{Q_1} = 10$ (red), 0 (black) and -10 (blue). Solid lines are quadratic fits. (*Inset*) Variance of the current as a function of λ_{Q_1}, measured from the curvature of the LDFs. (b) Nonequilibrium current (black dots) and the prediction from Eq. 4.8 approximated to the first (dotted red) and second order (dotted dashed blue), where the shaded area represents the statistical error in the second order coefficient.

4.3 Microscopic Interpretation of Rectification

Nonlinear Response from the Large Deviation Formalism [2]

To apply the large deviation formalism, we start by recognizing that the affinity for the heat transfer process is $X = 1/(T_0 - \Delta T) - 1/(T_0 + \Delta T) \approx 2\Delta T/T_0^2$. For the Andersen thermostat, the path probability can be written as

$$P_{\Delta T}[\tilde{x}] \propto \prod_k \sqrt{\frac{m_1}{2\pi T_1}} \exp[-\frac{m_1 v_1(t_k)^2}{2T_1}] \times \prod_l \sqrt{\frac{m_N}{2\pi T_N}} \exp[-\frac{m_N v_N(t_l)^2}{2T_N}], \tag{4.6}$$

where $t_k(t_l)$ are times at which the first(last) particle collides with the bath. From this we can derive the relative path action, and the time-symmetric part follows as

$$Q_1[\tilde{x}] = \frac{T_0}{4t_N} \left(\sum_k m_1 v_1^2(t_k) - \sum_l m_N v_N^2(t_l) \right) - J[\tilde{x}]. \tag{4.7}$$

Note that since we have chosen to express the action in terms a Taylor expansion of ΔT, we have an infinite series of time symmetric parts; however, we could have formulated in terms

[2] Most of the content of this subsection was originally written by the author for the following publication: C. Y. Gao and D. T. Limmer, "Nonlinear Transport Coefficients from Large Deviation Functions", *The Journal of Chemical Physics* **2019**, 151 (1).

of $\Delta(1/T)$, in which case there will only be one single term Q_1. The average current as a function of ΔT becomes

$$\langle J\rangle_{\Delta T} = \beta t_{\rm N}\left\langle J^2\right\rangle_0 \frac{2\Delta T}{T_0^2} + \beta^2 t_{\rm N}^2\left\langle J^2 Q_1\right\rangle_0 \left(\frac{2\Delta T}{T_0^2}\right)^2 + O(\Delta T^3)\,. \tag{4.8}$$

The first term is the standard Green-Kubo result for the thermal conductivity in terms of an integrated heat flux autocorrelation function. The second term correlates the squared heat flux with the instantaneous temperature difference, and results in an asymmetric response of the current. Since the masses of the two ends are different, the time dependent temperature fluctuations on either side of the chain need not be the same. This expression illustrates that thermal current rectification is a product of microscopic correlations between instantaneous temperature gradients and heat fluxes.

The evaluation of $\psi_0(\boldsymbol{\lambda})$ from diffusion Monte Carlo is shown in Fig. 4.6(a), while the nonequilibrium simulation results of the current is shown in Fig. 4.6(b). Both the LDFs and the nonequilibrium simulation results averaged over 9600 realizations are calculated for trajectories with $t_{\rm N} = 2\times 10^5$. The LDFs are evaluated at $\lambda_J \in [-32, 32]$ for $\lambda_{Q_1} = 10$, and $\lambda_J \in [-20, 20]$ for $\lambda_{Q_1} = 0, -10$. Eight independent samples are calculated at each combination of $\boldsymbol{\lambda}$, and standard deviations are plotted as error bars in Fig. 4.6(a). For each set of samples at a specific λ_{Q_1}, a parabola is fit, and the error bars in inset of Fig. 4.6(a) are the standard deviation among the 8 curvatures. To estimate the statistical error in the second order transport coefficient, the fitted slope in the inset of Fig. 4.6(a) is evaluated individually for each of the 8 sample sets, and standard error of the mean is reported in Fig. 4.6(b). While $t_{\rm N}\left\langle J^2\right\rangle_0$ is measured by the curvature of ψ_0 with $\lambda_{Q_1} = 0$, $t_{\rm N}^2\left\langle J^2 Q_1\right\rangle_0$ is measured by how the curvature changes as we change λ_{Q_1}. Given the definition of Q_1, the change of the curvature with λ_{Q_1} directly reports the change in the thermal conductivity with a temperature gradient. To make a better comparison, we plot the shifted LDFs $\psi_0^*(\lambda_J, \lambda_{Q_1}) = \psi_0(\lambda_J, \lambda_{Q_1}) - \psi_0(\lambda_J, \lambda_{Q_1} = 0)$ so that all the curves have the same minimum value at $\lambda_J = 0$. Our method correctly predicts the rectification behavior with high accuracy.

To demonstrate the statistical efficiency of our approach, in Fig. 4.7 we compare the statistical error in the evaluation of $t_{\rm N}^2\left\langle J^2 Q_1\right\rangle_0$ by direct evaluation and using the cloning algorithm. The direct evaluation, plotted as $\lambda_J = 0$ in Fig. 4.7, is evaluated by computing the triple correlation function by brute force averaged among 1.2×10^5 independent trajectories. In the cloning algorithm, we evaluate $\psi(\lambda_J, \lambda_{Q_1} = 10)$ for various λ_J's with the same number of walkers $N_{\rm w} = 1.2\times 10^5$, and compute the correlation function by $t_{\rm N}^2\left\langle J^2 Q_1\right\rangle_0 = 2[\psi_0(\lambda_J, \lambda_{Q_1}) - \psi_0(\lambda_J, 0) - \psi_0(0, \lambda_{Q_1})]/(\lambda_J^2\lambda_{Q_1})$. Statistical errors are estimated by the standard deviation from 9 independent simulations. We have chosen the same number of walkers and independent trajectories to ensure that the computational effort in terms of number of integration steps is the same. For equal computational effort evaluating $\left\langle J^2 Q_1\right\rangle_0$ from the large deviation function exhibits smaller statistical error for sufficiently large λ_J's, as shown in Fig. 4.7. For a fixed λ_{Q_1}, the error in the curvature of ψ_0 with respect to λ_J should scale as $\propto \sqrt{\psi_0''(\lambda_J)/\tilde{N}_w}/\psi_0(\lambda_J) = 1/(\lambda_J^2\sqrt{\tilde{N}_{\rm w}})$, where $\tilde{N}_{\rm w}$ is the number of uncorrelated walkers.

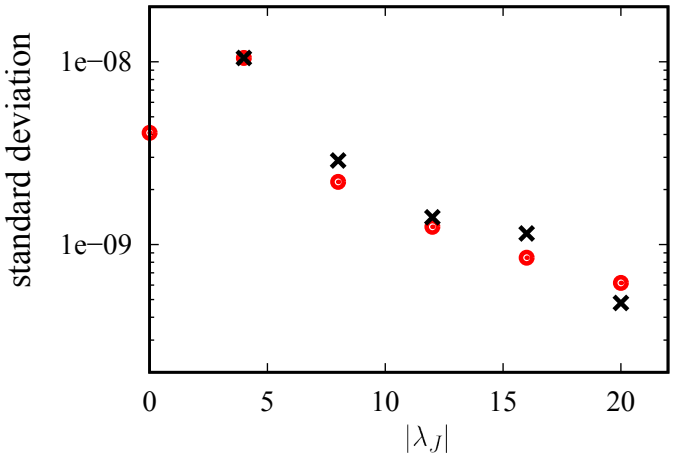

Figure 4.7: Comparison of statistical error in $t_{\rm N}^2 \langle J^2 Q_1 \rangle_0$ from direct evaluation (plotted as $\lambda_J = 0$) and the cloning algorithm for different λ_J's while fixing $\lambda_{Q_1} = 10$. Red dots are for positive λ_J's while black crosses are for negative ones.

Even though the correlation between the walkers as λ_J increases brings in a non-trivial dependence of $\tilde{N}_{\rm w}$ on λ_J, overall the cloning algorithm still out-performs the direct evaluation for $|\lambda_J| > 8$ by about an order of magnitude.

Alternatively, one can compute the first order coefficients as a function of ΔT by

$$L_1(\Delta T) = \frac{2\beta t_{\rm N}}{T_0^2} \left(\left\langle (\delta J)^2 \right\rangle_{\Delta T} + \langle \delta J \delta Q_1 \rangle_{\Delta T} \right) , \tag{4.9}$$

where two integrated correlation functions evaluated in nonequilibrium steady states contribute to the thermal transport - the heat current auto-corelation function, and the current-activity cross correlation function. This result is shown in Fig. 4.8 for a few different scenarios, all of which agree with direct nonequilibrium simulations within statistical uncertainty. The thermal conductivity increases or decreases with ΔT linearly, which is a clear sign of thermal rectification. We can further decompose the contributions from the two correlation functions in Fig. 4.8. Interestingly, both terms respond asymmetrically with ΔT, while the auto-correlation function is the main contributor to the rectification behavior. For example, in Fig. 4.8(a) where the rectification ratio is negative, both correlation functions increase in magnitude at negative ΔT, while staying plateaued at positive ΔT. At negative ΔT, the increasing current auto-correlation function contributes most to the higher thermal conductivity, indicating increasing density of energy carriers when the temperature at the lower mass end is increased. At positive ΔT, the decreasing cross correlation function contributes most to the lower thermal conductivity, which can be interpreted as a boundary effect. Similar behavior can be found in Fig. 4.8(c) for the free boundary chain, though the asymmetry is less evident. In the scenario in Fig. 4.8(b) where the rectification ratio is positive, the correlation functions behave oppositely to the other two scenarios - the autoco-rrelation function increases in magnitude

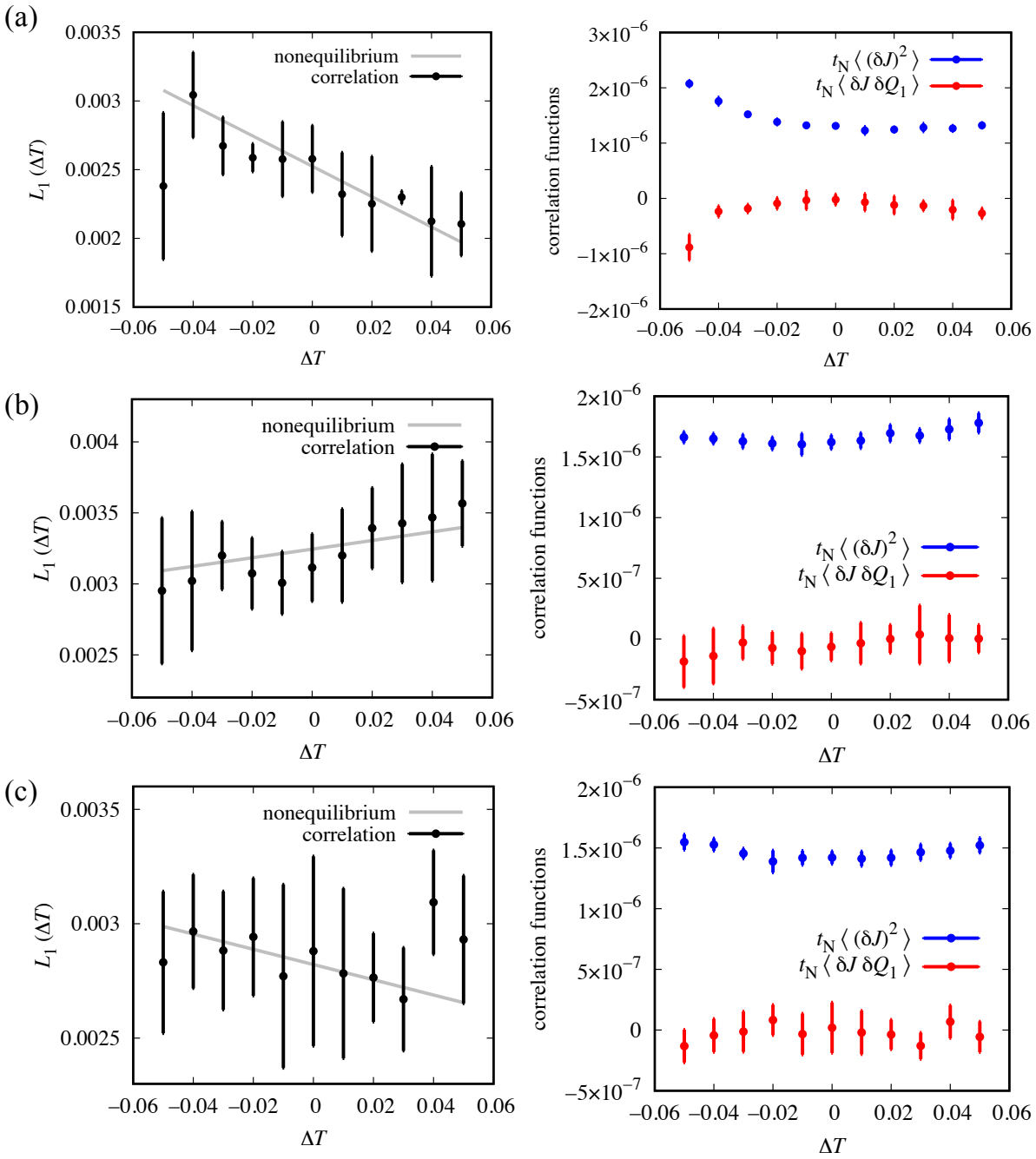

Figure 4.8: Computation of the thermal conductivity from nonequilibrium correlation functions in a mass graded FPUT chain at $T_0 = 0.1$ with (a) $N = 200$, $m_h/m_l = 10$, and fixed boundary condition; (b) $N = 20$, $m_h/m_l = 20$, and free boundary condition; (c) $N = 400$, $m_h/m_l = 20$, and free boundary condition. (Left) Comparison between results from nonequilibrium simulations (grey) and Eq. 4.9 (black) with one standard deviation. (Right) Integrated correlation functions $t_N \langle (\delta J)^2 \rangle_{\Delta T}$ (blue) and $t_N \langle \delta J \delta Q_1 \rangle_{\Delta T}$ (red).

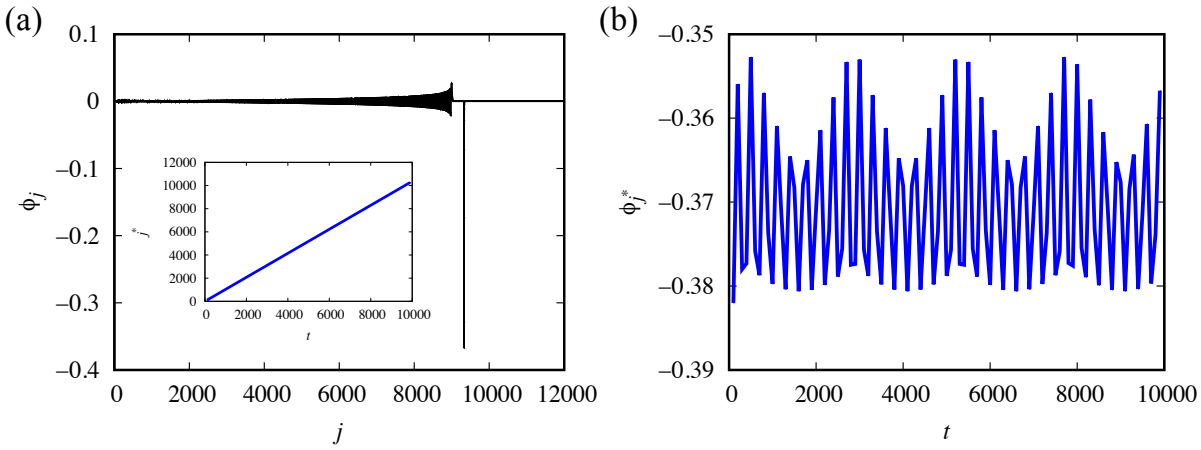

Figure 4.9: Soliton dynamics in the uniform mass FPUT chain with $m_h = m_l = 1$, free boundary condition, and an initial excitation of $v_0 = 1$. (a) Snapshot of the relative displacements at $t = 9000$, with the compressional soliton at $j = 9331$. (*Inset*) Soliton position as a function of time. (b) The relative displacement of the soliton as a function of time.

at positive ΔT, and the cross correlation function increases in magnitude at negative ΔT. Both correlation functions contribute equally to the rectification behavior, indicating a more significant role played by the boundary effects.

Momentum Excitation Method

Solitons are promising candidates for energy carriers in FPUT chains. A typical method used to investigate solitons numerically is the momentum excitation method. In the momentum excitation method, an initial perturbation is applied on the first particle

$$\dot{x}_j = v_0 \delta_{j,1}\,, \quad x_j = ja\,, \quad (j = 1, \cdots, N) \tag{4.10}$$

while the rest of the particles start at their equilibrium position with zero velocity. The displacement of particle j from its equilibrium position at subsequent times is measured by $u_j = x_j - ja$. When $|v_0|$ is higher than a certain threshold, a supersonic soliton can be observed separated from the phonon wave front, as seen in Fig. 4.9(a), where $\phi_j = u_j - u_{j-1}$ denotes the relative displacement between the adjacent particles. While the position of the soliton changes linear with time, its magnitude oscillates periodically with time, the pattern of which depends on the initial excitation v_0. Tracing the position and the magnitude of the soliton with time gives us a measurement of its velocity v_s and activation energy ϵ_a, the latter of which is defined as the average kinetic energy per site of a soliton.

In Fig. 4.10 we plot the relationship between the soliton velocity, its activation energy, and the excitation energy defined as $\epsilon_e = m_1 v_0^2/2$ for FPUT chains with uniform mass $m = 1$

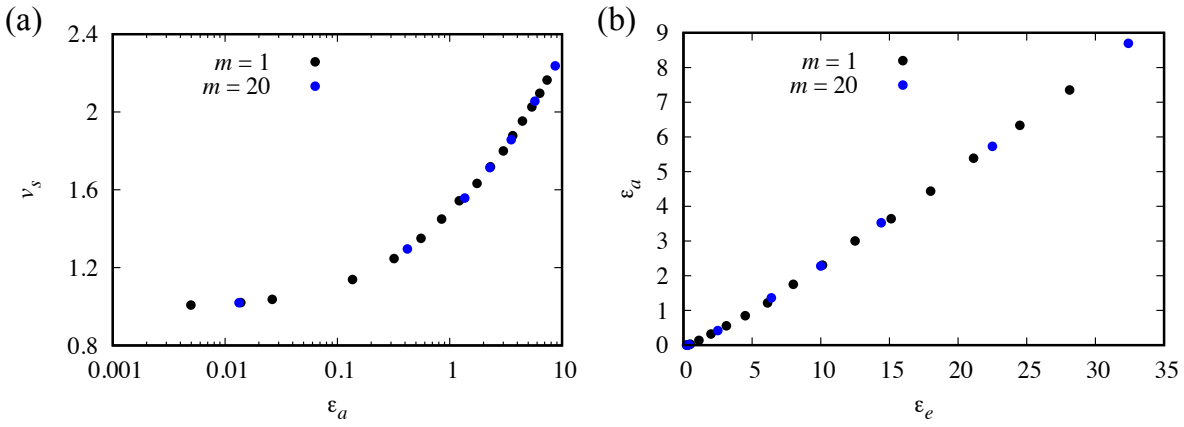

Figure 4.10: (a) Soliton velocity v_s as a function of its activation energy ϵ_a. (b) Activation energy ϵ_a as a function of excitation energy ϵ_e.

and $m = 20$. For the higher mass, we scale the soliton velocity by $\sqrt{m}$ and find perfect agreement between the two curves. This simple scaling relationship is evident from the equation of motion for the FPUT chain. The soliton velocity v_s scales as $\epsilon_a^{1/4}$ in the high energy limit, which is in agreement with the prediction of sound velocity from nonlinear fluctuating hydrodynamics. Assuming a Boltzmann distribution of solitons at the temperature ϵ_a/k_B, this indicates that the temperature dependence of the soliton agrees with that of the sound velocity of energy transfer, which is seen as evidence that solitons are promising candidates for energy carriers in FPUT chains [176]. While the activation energy increases with the excitation energy, its dependence is different in the low and high energy regime. In the low energy limit, the activation energy grows quadratically with the excitation energy; in the high energy limit, the two changes in a linear fashion. This indicates different soliton dynamics dependent on the temperature regime, which is similar to the results we have seen for the rectification behavior. It is worth mentioning that there is a threshold in the excitation energy $\epsilon_e \approx 0.3$, below which the velocity of the soliton is lower than the phonon front, so that an isolated soliton peak cannot be observed.

To investigate the effect of mass gradient in the soliton dynamics, we next use momentum excitation method to generate solitons in a mass graded FPUT chain. To observe the soliton against the mass gradient, the mass along the chain is defined as in Eq. 4.2 with $m_l = 1$. To observe the soliton following the mass gradient, we again impose a momentum excitation at the first particle, but we set $m_h = 1$ and vary the value of m_l in Eq. 4.2 instead. In Fig. 4.11(a) we again plot the relative displacements along the chain for a soliton against the mass gradient with $N = 20000$, $m_h/m_l = 200$, and free boundary condition. Compared with the uniform mass chain in Fig. 4.9(a), we observe a clear difference in the configurations, especially at the left end of the chain, where chaotic behaviors arise in the mass graded chain. The velocity of the soliton decreases with the increasing mass, as seen in the inset of

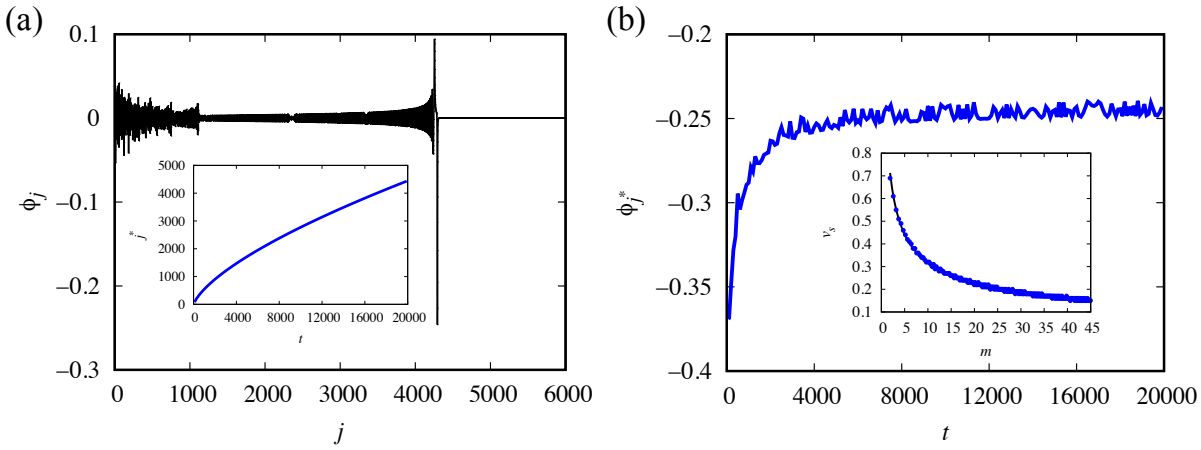

Figure 4.11: Soliton dynamics in the mass graded FPUT chain with $N = 20000$, $m_h/m_l = 200$, free boundary condition, and an initial excitation of $v_0 = 1$. (a) Snapshot of the relative displacements at $t = 19000$, with the compressional soliton at $j = 4294$. (*Inset*) Soliton position as a function of time. (b) The relative displacement of the soliton as a function of time. (*Inset*) Soliton velocity v_s as a function of mass. The black curve is the power law fit $v_s = 0.9849\, m^{-0.492}$.

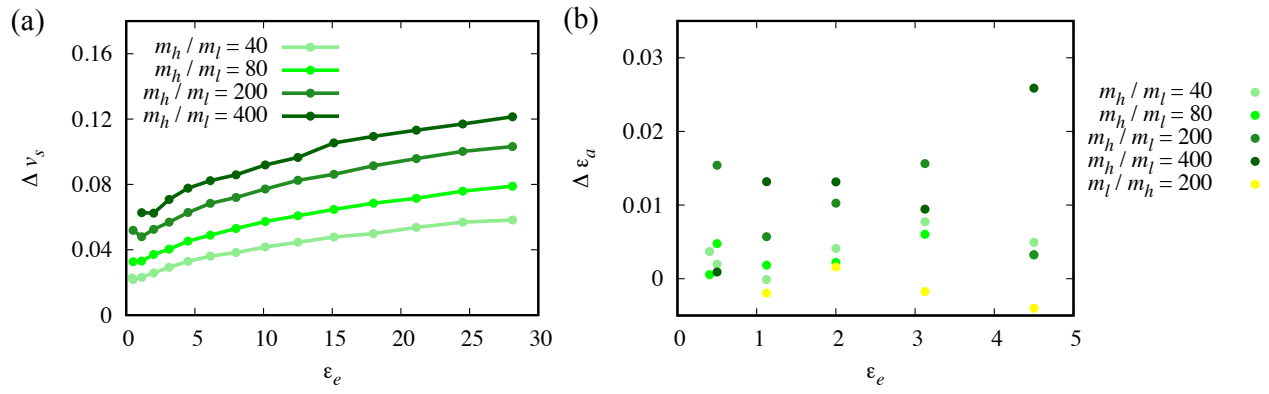

Figure 4.12: Comparison between soliton dynamics in the uniform and mass graded FPUT chain with free boundary condition, at different excitation energies. (a) The difference in the soliton velocity. (b) The difference in the activation energy.

Fig. 4.11(a). The difference is even more striking when we plot the height of the soliton peak with time in Fig. 4.11(b). While the magnitude starts at a similar value as in the uniform chain, it decays dramatically with time until plateauing to a smaller value. The periodic oscillation seen in the uniform chain is replaced by a more chaotic behavior, which is a result of the mass scattering effect. This behavior is seen at higher excitation energy as well, though the decay of the magnitude is less dramatic.

To quantify the effect of the mass scattering, we plot the soliton velocity as a function of its mass in the inset of Fig. 4.11(b) and fit a power law function $v_s = A\, m^{-B}$. Naively the velocity should scale as $m^{-0.5}$ as explained earlier. The result we obtain is $B = -0.492$, which is in good agreement, while $A = 0.9849$ is interpreted as the velocity extrapolated to $m = 1$. We compare this extrapolated soliton velocity with the velocity in the uniform chain with $m = 1$, and plot the difference $\Delta v_s = v_s(m = 1) - A$ for a series of mass gradients in Fig. 4.12(a). Alternatively, one can compare the difference in the activation energy of the soliton, defined similarly as $\Delta\epsilon_a$, as it is positively correlated with v_s. This result is shown in Fig. 4.12(b) for both positive and negative mass gradients. While both results are prone to statistical uncertainties, their positivity in the case of positive mass gradients confirms the fact that solitons traveling against the mass gradient has a smaller velocity and activation energy due to the mass scattering. The effect becomes more evident at higher mass gradients, while it seems absent in the case of negative mass gradient. The decrease in activation energy also indicates that the threshold of excitation energy to generate an isolated soliton is higher against a higher mass gradient. Given that this threshold is quite low at $\epsilon_e \approx 0.3$, one might explain the weaker rectification behavior seen in higher temperatures with the fact that soliton generation is relatively insensitive to the mass gradient at such high temperatures. This asymmetric effect also partially explains the fact that increasing the temperature at the lower mass end facilitates the generation of solitons against the mass gradient, and thus increases the heat conductivity, while increasing the temperature at the higher mass end has a smaller effect on the density of the energy carriers generated at the boundary.

The results we have shown so far are all concerned with the free boundary condition. In the case of fixed boundary condition, the momentum excitation method illustrates a far more complicated picture of heat transport. As seen in Fig. 4.13, multiple nonlinear excitations, including soliton, kink, and breather, arise and interact with each other in the mass graded FPUT chain. While the different behaviors against and following the mass gradient is evident, a more systematic study on their statistics is needed to interpret their role in heat transport.

4.4 Conclusion

In this chapter, we have presented a systematic study on the anomalous transport and thermal rectification behavior in FPUT chain, and explored the microscopic origin of nonlinear behaviors using correlation functions and momentum excitation method. Our result suggests that the heat transfer mechanism is different in the low temperature and high temperature regimes, and the energy carriers are of different nature in fixed and free boundary chains.

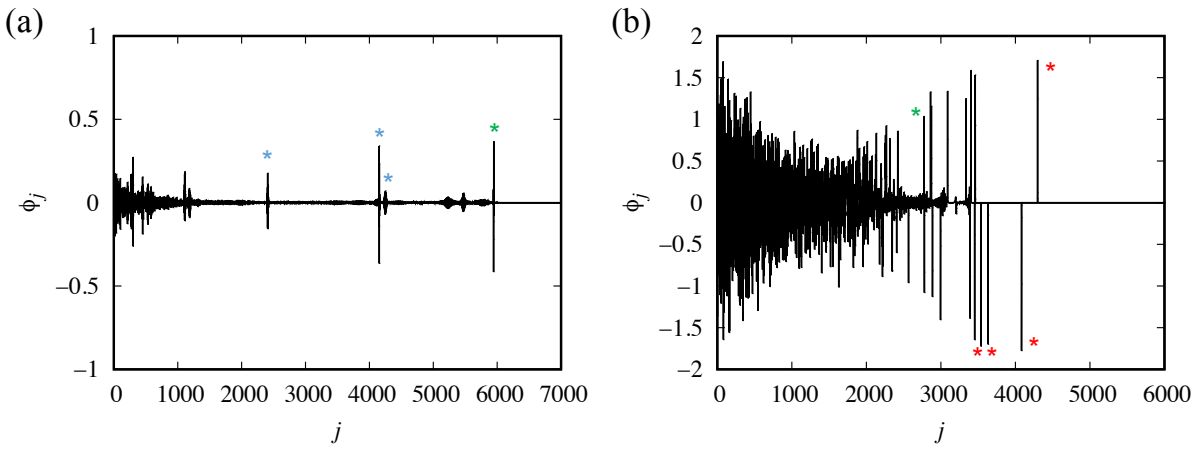

Figure 4.13: (a) Snapshot of the relative displacements at $t = 15000$ with an initial excitation of $v_0 = 8$, for a FPUT chain with $m_h/m_l = 20$. Multiple breathers (blue star) and a kink soliton (green star) are observed. (b) Snapshot of the relative displacements at $t = 9000$ with an initial excitation of $v_0 = 8$, for a FPUT chain with $m_l/m_h = 20$. Multiple solitons (red star) and a kink soliton (green star) are observed.

While we have only studied the dynamics of isolated solitons based on the method of momentum excitation, more investigations into soliton-soliton interactions, and solitons with thermal fluctuations need to be done. The right approach to use on this problem is not entirely clear, though a few recent work in this direction have shed light on the behavior of solitons in thermal environments. For example, a study on the scattering of solitons in nonlinear lattice models suggests that solitons can have only a relatively short survival time when exposed in a thermal environment [177]. Another study on the Korteweg-de Vries equation with noise and damping suggests a normal diffusion behavior for solitons with very low energy [178].

More broadly speaking, the interplay between anharmonicity and mass gradient can lead to unexpected results, and are still far from being fully understood. Despite the already heavy numerical efforts devoted to the problem, much longer time scales and system sizes have to be explored in order to fully appreciate the role of nonlinear terms.

Chapter 5

Electron Transport: Nonlinear Transport in Computing Circuits

5.1 Introduction [1]

The last decade has seen an exponential growth in energy consumption associated with information, communications, and computing technologies. Such resource demands are not sustainable, and thus there is a need to design devices with reduced energetic costs. While the problem of computing efficiency dates back to Landauer [179, 180], with modern developments in stochastic thermodynamics, this problem is actively being revisited [181, 182]. The main goal of this chapter is to bridge the gap between developments in nonequilibrium statistical physics and circuit engineering by proposing a model for stochastic logic circuits that is thermodynamically consistent, and thus amenable to physical analysis and constraints, but simple enough to be extendable to complex computing tasks. By treating thermal fluctuations in electron transport explicitly at a mesoscopic scale, our model reproduces the behavior of a robust circuit in the low noise limit, but describes errors accurately away from this limit. With this model we explore the consequences of carrying out computations at low thermodynamic costs and finite time, and provide design principles for low dissipation computing devices.

State-of-the-art semiconductor devices are typically built from metal-oxide-semiconductor field effect transistors on the scale of a few nanometers, enabling billions of transistors to be packed on a single chip. In order to mitigate heating and large energy consumption burdens, it would be advantageous to operate such small devices with small bias voltages, however as biases approach thermal scales, fluctuations increase, which necessitates a careful treatment of thermal noise [183, 184]. The conventional treatment of thermal noise is largely phenomenological and involves either a correction to the power spectral density [185], or transformation of the internal noise into external independent sources [186, 187]. Such models

[1] Most of the content of this chapter was originally written by the author for the following publication: C. Y. Gao and D. T. Limmer, "Principles of Low Dissipation Computing from a Stochastic Circuit Model", *arXiv: 2102.13067*.

are typically valid only near equilibrium where the fluctuation-dissipation theorem can be invoked to constrain their functional form [188], whereas higher order correlations are needed in general to determine the full response [21, 189, 190]. While these models can provide insight into how thermal noise may put a physical limit on the density of transistors [191], their validity in non-linear electrical networks operating far from equilibrium is uncertain.

Stochastic thermodynamics provides a theoretical way to move beyond an equilibrium description of thermal noise and its impact on information processing [192]. While information theory provides limits on the accuracy of typical communication [193, 194], stochastic thermodynamics provides generalized fluctuation-dissipation relationships, and places limits on the work required to implement a physical process in finite time and the spectrum of its fluctuations [13–15, 195]. The link between information theory and stochastic thermodynamics has generated a wealth of expressions relating precision, speed and dissipation, including the thermodynamic uncertainty relationships, speed limits, and fluctuation theorems. For example, dissipation bounds the rate at which a system transforms between different states [196–200]. Dissipation also provides an upper bound for the precision of a current [17, 201, 202]. A universal tradeoff between power, precision and speed has been proposed for communication systems as well [203]. These theoretical results have found application in many biological processes that natively operate near thermal energy scales [16, 204–208]. Placed in the context of artificial computing, these relationships have shed light on fundamental constraints on the design of computing devices to minimize thermodynamic costs [181, 182, 209–212].

While such theoretical results are general, to apply them to the problem of computing design requires a realistic physical representation of information processing, such as bit storage, measurement, and erasure. Some success has been made with non-linear single electron devices and Coulomb blockade systems [213–215], where the logical states are represented by the presence of a few electrons. More recently, thermodynamically consistent stochastic models have been proposed for transistors and non-linear electronic circuits [216–218]. Even though such models are capable of describing a broad range of nonlinear devices at a macroscopic level, they are based on continuum descriptions and therefore model parameters are chosen phenomenologically. Here we adopt a different approach where single logic gates are described by a tunnel junction model on the mesoscopic scale, combined with a capacitive circuit model for the charging and manipulation of the device. Such an approach is able to describe electron transport processes consistent with the fluctuation theorems [219, 220], but also consistent with the complementary metal-oxide-semiconductor (CMOS) circuit platform used widely in modern computing devices. Therefore, it provides an ideal platform to study circuit behaviors with the tool of stochastic thermodynamics.

In the chapter that follows, we demonstrate principles for low dissipation computing by constructing a stochastic model for logic circuits from a bottom-up approach. By working with elementary linear components, we can build nonlinear circuits that are thermodynamically consistent. We first introduce a mesoscopic model for transistor based on the Landauer-Büttiker formalism in Section 5.2. In Section 5.3 we introduce a model for single gates, including the NOT gate and the NAND gate, and discuss their physical properties. We then study in

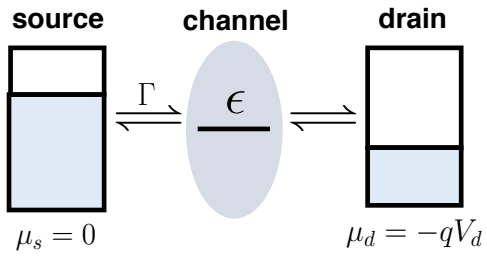

Figure 5.1: Kinetic diagram of the mesoscopic model for a transistor.

Section 5.4 the collective behaviors of these basic components, including spatial correlations within combinational circuits, and temporal correlations within sequential circuits, where the emphasis will be on circuit design principles. The logic circuits are finally modularized and scaled up to a computing device to illustrate how multiple components are synchronized to complete a computing task in Section 5.5. Throughout, the thermodynamically consistent model enables a description of errors and dissipation.

5.2 Tunnel Junction Model for Transistors

The Landauer-Büttiker formalism provides an atomistic view of electrical resistance, and has been used to study mesoscopic physics in Aharonov-Bohm ring, and the quantum dot. Here we build a mesoscopic model for a single transistor based on the Landauer-Büttiker formalism [221], the kinetic diagram of which is provided in Fig. 5.1. The electrodes are modeled by electron reservoirs with chemical potential μ_j, with $j = s, d$ denoting the source and drain respectively, and follows the Fermi distribution of electron density

$$f_j(x) = \frac{1}{e^{\beta(x-\mu_j)} + 1}\,, \tag{5.1}$$

where $\beta = 1/k_{\rm B}T$, $k_{\rm B}$ is the Boltzmann constant, T the temperature of the device, and x the electron energy. The source is kept at $\mu_s = 0k_BT$ as the reference, and the drain is kept at voltage V_d so that $\mu_d = -qV_d$. The channel, denoted by c, is modeled with a single electron level with energy ϵ. Electron can jump between the reservoirs and the channel ballistically with an escape rate Γ from any site (s, d or c). If we denote p_1 as the probability that the channel is occupied, and $p_0 = 1 - p_1$ as the probability that the channel is empty, we can then write down a master equation for the occupation of the channel

$$\dot{p}_1 = (k_{cs}p_0 - k_{sc}p_1) - (k_{dc}p_1 - k_{cd}p_0)\,, \tag{5.2}$$

where the transistion rates k_{ji} that describe the exchange rate of an electron from site i to j are given by

$$\begin{aligned} k_{cs} &= \Gamma f_s(\epsilon)\,, \quad & k_{sc} &= \Gamma[1 - f_s(\epsilon)]\,, \\ k_{cd} &= \Gamma f_d(\epsilon)\,, \quad & k_{dc} &= \Gamma[1 - f_d(\epsilon)]\,. \end{aligned} \tag{5.3}$$

The steady state solution of Eq. 5.2 gives the electron current across the source and the drain

$$J = \frac{\Gamma}{2}[f_s(\epsilon) - f_d(\epsilon)]\,. \tag{5.4}$$

In other words, it is only when the energy level ϵ lies within a few k_BT of the potentials μ_s and μ_d that we have $f_s(\epsilon) \neq f_d(\epsilon)$ and a current flows.

To model a transistor, we need to a mechanism to tune the channel energy ϵ by some input voltage, which plays the role of the gate voltage in a field-effect transistor. It is worth mentioning here that there are typically two types of transistors used in modern CMOS circuits, the N-type and P-type transistors. They are differentiated by their major charge carriers - electrons for N-type and holes for P-type. In the N-type transistor, a positive gate voltage applied to the gate lowers the energy levels in the channel, which makes the channel more conductive and turns the transistor on. In the P-type transistor, on the other hand, a negative gate voltage increases the number of holes in the channel, and thus induces a on state in the transistor. To model the effect of the gate voltage accurately requires solving the electrostatic equations to determine the electron density in the channel. In our model, for simplicity, we let the channel energy level ϵ_i with $i = \mathrm{N}, \mathrm{P}$ for the N-type and P-type transistors change linearly with an input voltage V_{in}, which is a good approximation in the limit of high gate capacitance [221],

$$\epsilon_{\mathrm{P}} = \epsilon^0_{\mathrm{P}} + qV_{\mathrm{in}}\,, \quad \epsilon_{\mathrm{N}} = \epsilon^0_{\mathrm{N}} - qV_{\mathrm{in}}\,, \tag{5.5}$$

where $\epsilon^0_{i=\mathrm{N,P}}$ are reference energies and q is the unit of electric charge. The sign of the slope differentiates the N and P-type transistors with different charge carriers. Fig. 5.2 shows the current flowing across the transistors with reference energy $\epsilon^0_{\mathrm{P}} = \epsilon^0_{\mathrm{N}} = 0k_BT$ at different V_{in}. As can be seen, with V_{in} tuning the energy level of the channel, we can reproduce the switching behavior observed in the transistor.

5.3 Model for Single Gates

Modern CMOS circuits implement logic functions in an energy efficient manner by integrating N-type and P-type transistors. Based on the model introduced in the last section, we again choose a mesoscopic tunnel junction model to describe electron transport in a single gate [221]. As before, the transistors are modeled by two single electron levels of energy ϵ_i with $i = \mathrm{N}, \mathrm{P}$ for the N-type and P-type transistors. The electrodes are modeled by electron reservoirs with chemical potential μ_j with $j = s, d, g$ denoting the source, drain, and gate respectively. Electron transfer among them is described by a Markovian master equation, parametrized by transition rates k_{ji}. The transition rates are chosen to satisfy a local detailed balance condition, and thus guaranteeing thermodynamical consistency,

$$\frac{k_{ji}}{k_{ij}} = e^{-\beta(E_j - E_i)}\,. \tag{5.6}$$

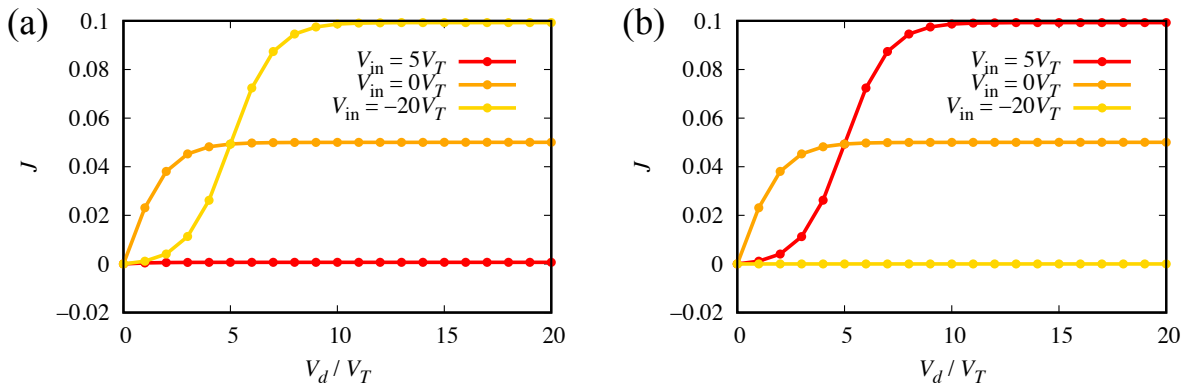

Figure 5.2: Current as a function of drain voltage in the mesoscopic model for a (a) P-type and (b) N-type transistor. $V_T = k_B T/q$ denotes the thermal voltage. The escape rate is chosen as $\beta\hbar\Gamma = 0.2$, and the reference energy $\epsilon_{\mathrm{P}}^0 = \epsilon_{\mathrm{N}}^0 = 0k_BT$.

The energy is described by either the band energy for an electron in the transistor ϵ_i, or a chemical potential μ_j, for an electron in an electrode. The condition of local detailed balance is a prerequisite for the application of stochastic thermodynamics, as it ensures a correct description of dissipation away from equilibrium, and relaxation to a Boltzmann distribution at equilibrium. While local detailed balance models each microscopic transition as being thermally mediated, emergent nonlinear behaviors resulting from collections of transitions can take the system arbitrarily far from equilibrium [222].

The energy levels of the transistors are controlled by an input voltage denoted V_{in} as in Eq. 5.5. In the case of a field-effect transistor, V_{in} refers to the gate voltage that switches the transistor on and off. In our model, a voltage also uniquely determines the energetics of the electrodes by modulating their chemical potentials, $\mu_j = -qV_j$. Throughout, we will differentiate between two different types of electrodes. The first type, including the source and drain electrodes, are kept at fixed potentials, V_s and V_d, respectively. The second type, the gate electrode, satisfies a capacitive charging model with a fluctuating voltage V_g for reading out a gate. This is justified by the fact that in CMOS circuits, the output of a single gate is usually used as the input of another gate, in which case the two are connected through a capacitor. The dynamics of V_g is described by the equation of motion

$$C_g \frac{dV_g}{dt} = -J_g(t)\,, \tag{5.7}$$

where C_g is the capacitance and J_g is the electron current flowing into the electrode from the transistors. The constant capacitance implies a quadratic energy for charging the electrode, $E = C_g V_g^2/2$.

We adopt a semi-classical ballistic transport model for the rate of transfer of an electron from an electrode into or out of a transistor [223–225]. Such a description is valid in the weak

coupling limit between a transistor and an electrode relative to the thermal energy, and for transistors that are small in scale relative to the mean free path of the electron. We restrict our analysis to single energy level transistors, for which the corresponding transition rates between transistor i and electrode j are

$$k_{ij} = \Gamma f_j(\epsilon_i)\,, \quad k_{ji} = \Gamma[1 - f_j(\epsilon_i)]\,, \tag{5.8}$$

where $f_j(x)$ is the Fermi distribution defined in Eq. 5.1. The prefactor Γ is related to contact resistances and is chosen so that the timescale of electron transitions is longer than the timescale of thermal fluctuation, and thus the broadening of energy levels due to the coupling is smaller than thermal fluctuations. In making these assumptions to simplify our model, we have neglected effects such as scattering within the transistor, delocalization between the electrode and the transistor, and electron correlations, each of which can be incorporated into our model as long as thermodynamical consistency is retained.

Since we will be considering energy scales on the order of thermal fluctuations at the room temperature, we use $V_T = k_B T/q \approx 26\text{me}\text{V}$ and $\beta\hbar \approx 25\text{fs}$ as our units of voltage and time, where $\hbar$ is Planck's constant. The voltage signal to noise ratio V_d/V_T in our model will be on the order of 10, which is the prerequisite of low dissipation in the computing process since the two are closely related. While this ratio is two orders of magnitude lower than the current industry level, and requires delicate operation of the device, it can be experimentally achieved by designs such as the single-electron box [226, 227].

We reference potentials relative to the source voltage so that $V_s = 0V_T$, and take $\epsilon_{\text{P}}^0 = 0k_BT$ and $\epsilon_{\text{N}}^0 = 1.5qV_d$ so that there exists only one independent energy parameter V_d. The transition rate constant is chosen as $\beta\hbar\Gamma = 0.2$ to ensure the weak coupling assumption is valid [228]. To study the dynamics of the gates, we use both the exact steady state solution of master equation when possible, and Gillespie simulations [229] to sample individual trajectories. We set $C_g = 200q/V_T$ in order to separate the timescales of capacitor charging from individual electron transfer events, simplifying the Gillespie simulations. Details of the numerical methods and the justification of the parameters will be specified in the following subsections.

NOT Gate

The NOT gate, also known as the inverter, takes a single binary input X, and generates its complement as the output Y. The circuit diagram of the NOT gate, composed of two transistors, is shown in Fig. 5.3(a). The N-type transistor is connected to a lower source voltage $V_s = 0V_T$ on its left, while the P-type transistor is connected to a higher drain voltage V_d to its right. Both transistors are controlled by an input voltage V_{in} as in Eq. 5.5, which is treated as fixed in a single gate, while the output voltage V_{out} is measured between the two transistors from the capacitor voltage V_g, which evolves according to Eq. 5.7. The kinetic diagram for our Markovian model is also shown in Fig. 5.3(a). Electrons can move ballistically between adjacent sites in the kinetic diagram according to a master equation. The Markovian system is described by the occupation number of the two single electron

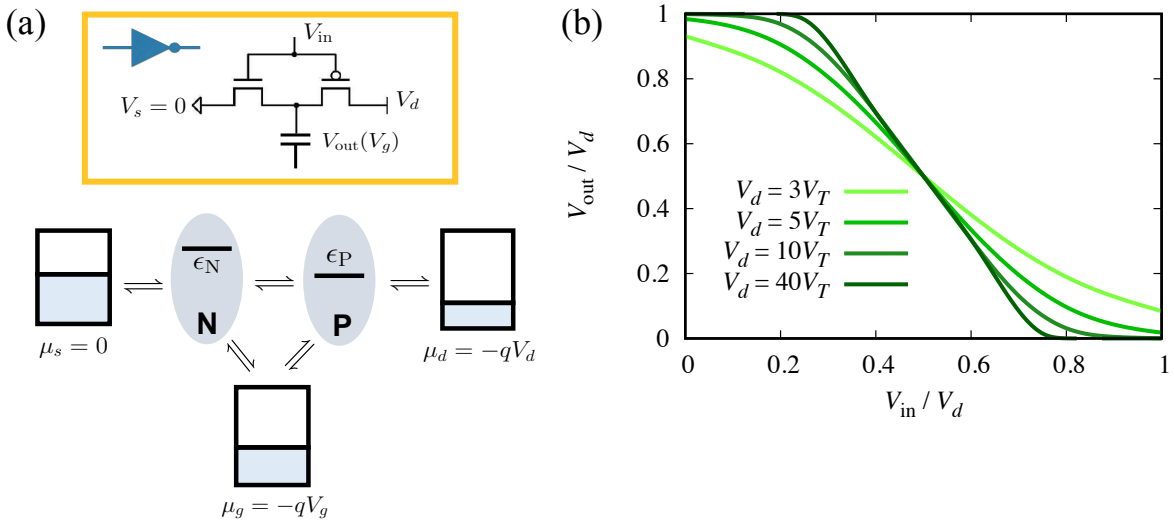

Figure 5.3: (a) Circuit diagram (above) and kinetic diagram (below) of a NOT gate, which is composed of a N-type (left) and a P-type transistor (right). (b) Voltage transfer curve of a NOT gate.

levels $n_{\rm N}$, $n_{\rm P} = 0/1$, and the gate voltage V_g. Electrons can jump between the transistors and the reservoirs only if the target site is empty. The rate describing the exchange of electrons between the transistors and the reservoirs are given by

$$\begin{aligned} k_{{\rm N}s} &= \Gamma f_s(\epsilon_{\rm N})\,, \quad & k_{s{\rm N}} &= \Gamma[1 - f_s(\epsilon_{\rm N})]\,, \\ k_{{\rm P}d} &= \Gamma f_d(\epsilon_{\rm P})\,, \quad & k_{d{\rm P}} &= \Gamma[1 - f_d(\epsilon_{\rm P})]\,, \\ k_{{\rm N}g} &= \Gamma f_g(\epsilon_{\rm N})\,, \quad & k_{g{\rm N}} &= \Gamma[1 - f_g(\epsilon_{\rm N})]\,, \\ k_{{\rm P}g} &= \Gamma f_g(\epsilon_{\rm P})\,, \quad & k_{g{\rm P}} &= \Gamma[1 - f_g(\epsilon_{\rm P})]\,. \end{aligned} \tag{5.9}$$

The transition rate between the two transistors depends on their relative energy levels, for example in the case of $\epsilon_{\rm P} > \epsilon_{\rm N}$,

$$k_{\rm PN} = \Gamma n(\epsilon_{\rm P} - \epsilon_{\rm N})\,, \quad k_{\rm NP} = \Gamma[1 + n(\epsilon_{\rm P} - \epsilon_{\rm N})]\,, \tag{5.10}$$

where $n(x) = [e^{\beta x} - 1]^{-1}$ is the Bose-Einstein distribution. The rate constant $\Gamma = 0.2/\beta\hbar \sim$ ps^{-1} is chosen so that electron transitions happen on a longer timescale than quantum tunneling, and the broadening of energy levels due to the coupling to electrodes is smaller than thermal fluctuations.

The dynamics of the capacitor is solved by the equation of motion

$$dV_g = -\frac{1}{C_g}\int_0^{t_{\rm int}} J_g(t)dt\,, \tag{5.11}$$

where C_g is the capacitance and J_g is the electron current flowing into the electrode from the transistors. While the transfer of electrons changes V_g, the capacitor is treated as an electron reservoir at constant chemical potential $\mu_g = -qV_g$ within each time interval $t_{\rm int}$. Thus the assumption made here is that the electron transfer within each $t_{\rm int}$ is small compared to $C_g V_T$, and the electron relaxation within the capacitor is fast compared to $t_{\rm int}$. We have chosen $C_g = 200q/V_T$, $t_{\rm int} = 10\beta\hbar$ in order to justify these assumptions.

Simulations were done with both an iterative, numerically exact diagonalization of the master equation as well as Gillespie simulations [229]. In both, we employ a separation of timescales for electron transfer to or from a transistor and gate charging, afforded by the large gate capacitance. Specifically, the large capacitance means we can update V_g every discrete $t_{\rm int}$, and compute rates at fixed V_g in between these dynamical updates. To obtain a numerically exact solution to the Markovian dynamics, for each interval $t_{\rm int}$, we solve for the average occupation number $\langle n_{\rm N}\rangle$, $\langle n_{\rm P}\rangle$ from the stationary solution of the master equation, which describes how the probability of the configuration $p_{n_{\rm N},n_{\rm P}} = (p_{0,0}, p_{0,1}, p_{1,0}, p_{1,1})$ evolves with time

$$\begin{aligned} \dot{p}_{n_{\rm N},n_{\rm P}} &= W p_{n_{\rm N},n_{\rm P}}\,, \\ W &= \begin{bmatrix} -S_1 & k_{r\rm P}+k_{g\rm P} & k_{l\rm N}+k_{g\rm N} & 0 \\ k_{\rm Pr}+k_{\rm Pg} & -S_2 & k_{\rm PN} & k_{l\rm N}+k_{g\rm N} \\ k_{\rm Nl}+k_{\rm Ng} & k_{\rm NP} & -S_3 & k_{r\rm P}+k_{g\rm P} \\ 0 & k_{\rm Nl}+k_{\rm Ng} & k_{\rm Pr}+k_{\rm Pg} & -S_4 \end{bmatrix}, \end{aligned} \tag{5.12}$$

where $S_j = \sum_{i\neq j} W_{ij}$ for a matrix W. The current J_g flowing into the capacitor is then computed by the sum of two terms

$$\begin{aligned} J_{\rm N\to g}/q &= k_{g\rm N}\langle n_{\rm N}\rangle - k_{\rm Ng}(1-\langle n_{\rm N}\rangle)\,, \\ J_{\rm P\to g}/q &= k_{g\rm P}\langle n_{\rm P}\rangle - k_{\rm Pg}(1-\langle n_{\rm P}\rangle)\,. \end{aligned} \tag{5.13}$$

In the Gillespie simulation, the electron jumping processes are modeled explicitly as chemical reactions, with $M = 10$ reaction rates

$$\begin{aligned} w_1 &= k_{\rm Ns}(1-n_{\rm N})\,, & w_2 &= k_{s\rm N} n_{\rm N}\,, \\ w_3 &= k_{\rm Pd}(1-n_{\rm P})\,, & w_4 &= k_{d\rm P} n_{\rm P}\,, \\ w_5 &= k_{\rm Ng}(1-n_{\rm N})\,, & w_6 &= k_{g\rm N} n_{\rm N}\,, \\ w_7 &= k_{\rm Pg}(1-n_{\rm P})\,, & w_8 &= k_{g\rm P} n_{\rm P}\,, \\ w_9 &= k_{\rm PN} n_{\rm N}(1-n_{\rm P})\,, & w_{10} &= k_{\rm NP} n_{\rm P}(1-n_{\rm N})\,. \end{aligned} \tag{5.14}$$

We use Monte Carlo method to simulate the probability that reaction i will happen after time t,

$$P(t,i) = w_i \exp[-\sum_{i=1}^{M} w_i t]\,, \tag{5.15}$$

and the currents between two sites are calculated as the discrete number of jumps between the two sites. The discretization error in voltages between the average protocol and the Gillespie simulation is on the order of $q/C_g = 0.005V_T$.

A NOT gate is typically characterized by its voltage transfer curve (VTC), shown in Fig. 5.3(b). The VTC reports on the average V_{out} in response to V_{in} in the long time limit. Generically, we find increasing V_{in} results in a decrease in V_{out} in agreement with the expected response of an inverter. However, its behavior is dependent on the scale of the thermal noise relative to V_d. The limiting values of V_{out} approach 0 and V_d for $V_{\text{in}} = V_d$ and $0V_T$, respectively, and sharpens between these limits with increasing V_d. Both features result from tuning the band energies of the two transistors in or out of resonance with their respective electrodes, as the transistor band energies depend on V_d through Eq. 5.5. Increasing V_d with $V_{\text{in}} = 0V_T$ or V_d, increasingly suppresses current into the gate capacitor from V_d or V_s. In the limit that current flows from only one electrode with fixed voltage, the gate electrode would reach an equilibrium state with that same voltage. The approach to this limiting behavior is exponential, for example for increasing $V_d \gg V_T$ and $V_{\text{in}} = 0V_T$, $|V_{\text{out}} - V_d| \sim \exp[-V_d/2V_T]$. The VTC is also symmetric around $V_{\text{in}} = V_{\text{out}} = V_d/2$, under which condition the difference between the energy level of the transistors and its connecting reservoirs is roughly the same for the N-type and P-type transistors.

Performance as a computing unit

When used as a computing unit, our first concern is whether our model generates the correct output with high probability. We define a perfect gate or device as one that generates a deterministic output according to the truth table, e.g. Y should be the complement of X for a perfect NOT gate. However in the presence of noise, the deterministic output becomes stochastic and subject to finite error rates. As can be anticipated from the behavior of the VTC, in the limit of high V_d/V_T, or the low noise limit, the performance of our model approaches that of a perfect NOT gate, whereas the behavior is nontrivial at smaller V_d.

The input and output signals are given as voltages in this model, so we map them to binaries by

$$X = \begin{cases} 0, & V_{\text{in}} = 0V_T \\ 1, & V_{\text{in}} = V_d \end{cases} \qquad Y = \begin{cases} 0, & V_{\text{out}} \leq \alpha V_d \\ 1, & V_{\text{out}} \geq (1-\alpha)V_d \\ \varnothing, & \text{otherwise} \end{cases} \tag{5.16}$$

where $\varnothing$ represents an invalid result that cannot be designated and α represents an error tolerance with $0 < \alpha \ll 1$. We choose $\alpha = 0.02$ so that the resultant error is below 10^{-10} for $V_d = 40V_T$ as comparable to current technologies, but our qualitative results are insensitive to this choice.

To characterize the accuracy of the gate, we define the error rate ξ as the probability of observing an output different from the perfect gate in a single shot. For the NOT gate, we observe in Fig. 5.4(a) Gaussian distributions in V_{out} in the steady state regardless of V_d, with the same variance $1/(\beta C_g)$. This is expected from a Boltzmann distribution, reflecting a proximity to equilibrium despite the presence of persistent currents. Under the Gaussian assumption, the error rate is uniquely determined by the average output voltage V_{out}. For

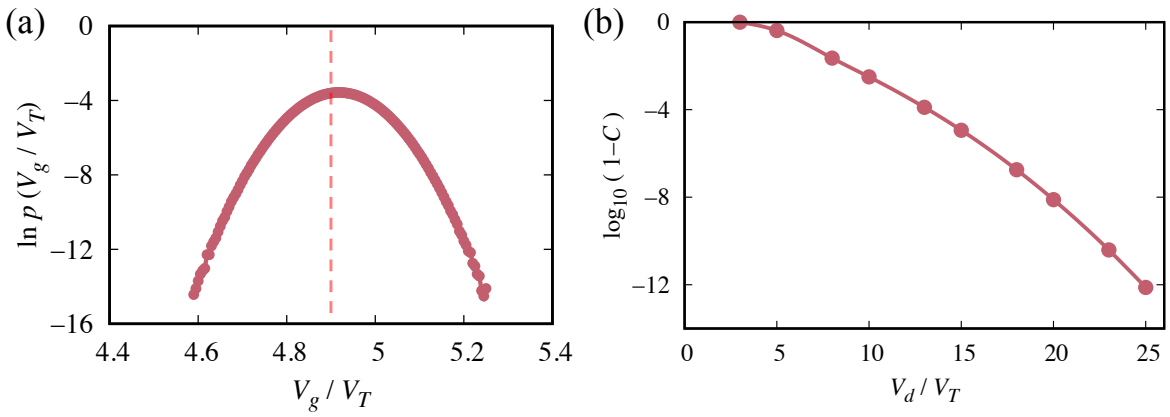

Figure 5.4: Static properties of a single NOT gate. (a) Steady state distribution of V_g at $t = 5 \times 10^6 \beta\hbar$, where the red dashed line labels the threshold voltage for $Y = 1$. (b) Channel capacity improves with increasing drain voltage V_d.

example, the accuracy rate for $X = 0$ is determined by the conditional probability

$$p(Y = 1|X = 0) = \int_{0.98V_d}^{\infty} dV \sqrt{\frac{\beta C_g}{2\pi}} \exp\left[-\frac{\beta C_g (V - V_{\text{out}})^2}{2}\right] . \tag{5.17}$$

In the case of $V_d = 5V_T$, the error rate is calculated as $\xi(X = 0) = p[V_{\text{out}} < (1 - \alpha)V_d|V_{\text{in}} = 0] = 0.36$.

A comprehensive characterization of the accuracy that takes into account the error rate for both cases of $X = 0/1$ is the channel capacity

$$C = \max_{p(X)} I(X;Y) , \tag{5.18}$$

which is the highest information rate that can be achieved with arbitrarily small error [194]. For a binary channel, the capacity is between 0 and 1, with 1 corresponding to a perfect gate. We compute C numerically from the mutual information $I(X;Y)$ between the input and output at steady state as a function of V_d. Marginalizing the conditional probabilities in Eq. 5.17 computed using V_{out} in the steady state, the mutual information can be computed by

$$I(X;Y) = \sum_{x=0,1} \sum_{y=0,1,\varnothing} p(x,y) \log_2 \frac{p(x,y)}{p(x)p(y)} . \tag{5.19}$$

We then numerically maximize $I(X;Y)$ over the base probability distribution $p(X)$ to compute the channel capacity. Here the capacity is computed to be $C = 0.60$ for a channel operated at $V_d = 5V_T$, given the slight difference between the error rate for $X = 0$ or 1. To reach a higher

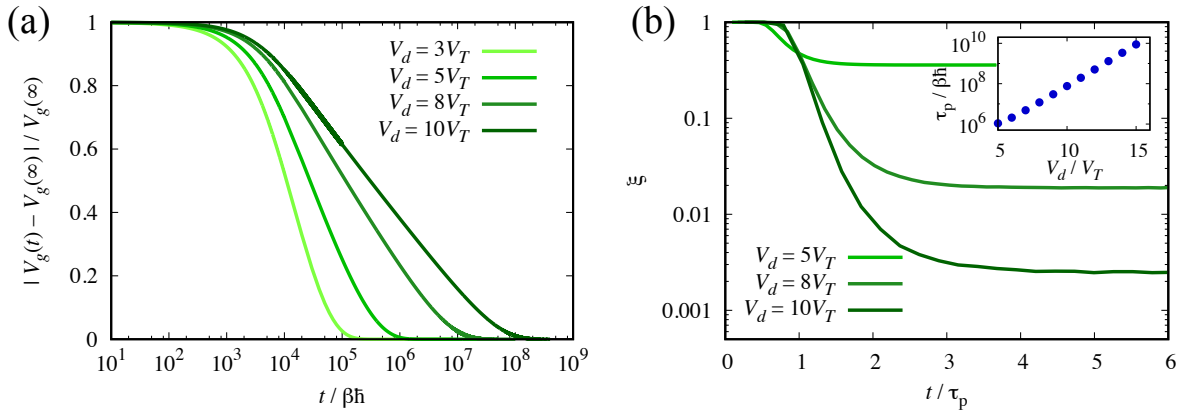

Figure 5.5: Trade-off among accuracy and speed for a single NOT gate. (a) Relaxation towards the steady state for a NOT gate initialized with $V_g = 0V_T$, and $X = 0$. (b) The decay of the error rate with time, scaled by propagation delay τ_p. (*Inset*) Propagation delay as a function of V_d.

capacity, we need the average output V_{out} to approach the limits $0V_T$ or V_d. This can be achieved by operating at a higher V_d so that the leakage current flowing through the higher energy level transistor is even smaller. Given the Gaussian statistics, asymptotically for large V_d the error scales as $\xi \sim \exp[-\beta C_g \alpha^2 V_d^2/2]\sqrt{2\pi/\beta C_g}/\alpha V_d$ and the channel capacity scales as $C \sim 1 - \xi(1 - \log_2 \xi)$, consistent with Fig. 5.4(b).

Trade-off among accuracy, speed and dissipation

While the accuracy of the gate improves dramatically for $V_d \gg V_T$, its performance is compromised by significantly increasing costs in computation time and energy consumption. Upon receiving a distinct input signal, the gate requires time to charge or discharge the capacitor to reach a steady state output signal. The average relaxation to steady state is shown in Fig. 5.5(a) for an initially discharged capacitor with input $X = 0$. The relaxation is monotonic and nearly exponential but with characteristic decay time that depends on V_d. Under this initial condition and input voltage, $\epsilon_{\text{N}} \gg \mu_s$, so that few electrons can flow between the source and the capacitor. The lower energy level ϵ_{P} facilitates electrons to transfer from the capacitor to the drain following the concentration gradient, gradually building up a higher voltage.

We define the time it takes for V_{out} to reach $(1 - \alpha)V_d$, the threshold voltage for $Y = 1$, as the propagation delay time τ_p. While the threshold voltage increases linearly with V_d, the average propagation delay τ_p grows exponentially. The propagation delay time, τ_p follows an inverse Gaussian distribution [230] with a long exponential tail (Fig. 5.6). Note that τ_p coincides with the time required for the error rate to decay below 0.5. Fig. 5.5(b) shows the decay of the error rate with time for $V_d = 5, 8, 10V_T$, scaled by the propagation delay

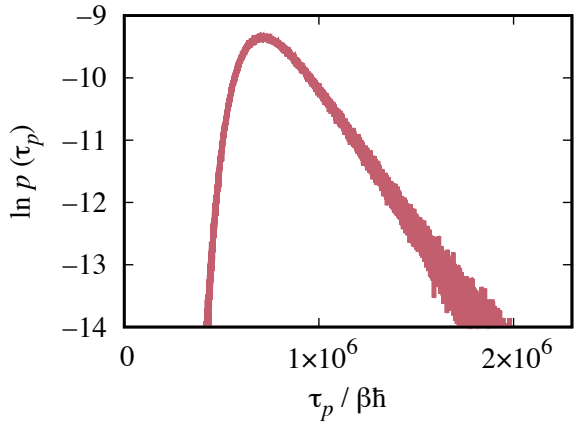

Figure 5.6: Distribution of the propagation delay τ_p for a single NOT gate with $X = 0$, $V_d = 5V_T$.

τ_p for each V_d. As the distribution of V_{out} remains Gaussian, the time dependence of the error reflects the charging of the gate capacitor, and specifically follows the evolution of the mean V_{out}. While we consider the single shot error, the exponential scaling of τ_p with V_d implies that associating an error rate with a time averaged measurement of V_{out} would yield a non-monotonic relationship between the waiting time to reach a set error threshold and V_d. For intermediate V_d, the slower decorrelation time will cause waiting times to increase with V_d, while for large V_d the suppressed fluctuations will dominate and decrease waiting times.

When the gate is used repeatedly to process a sequence of inputs $\mathbf{X} = \{X_1, X_2, \cdots, X_{N_{\text{data}}}\}$, there is no need to re-initialize the gate after each computation, and the residual charge on the capacitor may help reduce the computational cost. We call this a memory effect, which introduces temporal correlation between consecutive data transmission processes. For such an information channel with memory, the accuracy can be characterized with the average information rate per data, which is a generalization of the channel capacity [231]. The average information rate per data is defined as

$$\bar{I}(\mathbf{X};\mathbf{Y}) = \frac{1}{N_{\text{data}}} I(X_1, \cdots, X_{N_{\text{data}}}; Y_1, \cdots, Y_{N_{\text{data}}}) \,, \tag{5.20}$$

which in the limit of $N_{\text{data}} \to \infty$ and upon maximizing over the input probability distribution $p(\mathbf{X})$, is the generalization of the channel capacity. As an example, for $N_{\text{data}} = 2$, the mutual information is computed by

$$I(X_1, X_2; Y_1, Y_2) = \sum_{x_1=0,1} \sum_{x_2=0,1} \sum_{y_1=0,1,\varnothing} \sum_{y_2=0,1,\varnothing} p(x_1, x_2, y_1, y_2) \log_2 \frac{p(x_1, x_2, y_1, y_2)}{p(x_1, x_2) p(y_1, y_2)} \,. \tag{5.21}$$

To incorporate the memory effect, note that the probability distribution of the ith output Y_i is not only a function of X_i, but also the output voltage of the previous data V_{out}^{i-1}. The

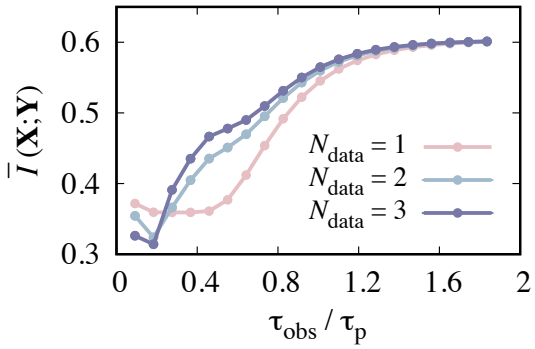

Figure 5.7: Average information rate for a repeatedly used NOT gate with $V_d = 5V_T$ as a function of the data processing time $\tau_{\rm obs}$.

dependence can be expressed with the conditional probability $p(V^i_{\rm out}|x_i, V^{i-1}_{\rm out})$, which we sample by Gillespie simulations of more than 10^7 trajectories. The dependence of I on the observation time $\tau_{\rm obs}$ thus comes from this conditional probability.

Let $V^0_{\rm out} = 0V_T$, we can write down the joint probability

$$p(x_1, x_2, V^1_{\rm out}, V^2_{\rm out}) = p(V^2_{\rm out}|x_2, V^1_{\rm out})p(V^1_{\rm out}|x_1, V^0_{\rm out} = 0V_T)p(x_2)p(x_1)\,, \tag{5.22}$$

which follows from the Markovian nature of the memory effect, and the fact that the input data x_i are independent from each other. The joint distributions can then be computed by marginalization, e.g. defining the mapping between Y and $V_{\rm out}$ in Eq. 5.16 as $Y = {\rm dig}(V_{\rm out})$,

$$p(x_1, x_2, y_1, y_2) = \sum_{y_1={\rm dig}(V^1_{\rm out})} \sum_{y_2={\rm dig}(V^2_{\rm out})} p(x_1, x_2, V^1_{\rm out}, V^2_{\rm out})\,, \tag{5.23}$$

where the sum is over all $V^i_{\rm out}$, discrete in our simulation, that correspond to y_i.

As the numerical maximization is difficult for large $N_{\rm data}$, without loss of generality, we choose as our input a sequence of independent and identically distributed Bernoulli random inputs with equal probability of being 0 or 1. We show in Fig. 5.7 the average information rate at $V_d = 5V_T$ for $N_{\rm data} = 1, 2, 3$ as a function of $\tau_{\rm obs}$, the processing time for each individual data from input to output. For $N_{\rm data} = 1$, the information rate first decreases at small $\tau_{\rm obs}$, as $\xi(X = 1)$ inevitably increases at short time due to the initialization $V_g = 0V_T$, and rises up sharply around the propagation delay τ_p, which is the time required for $\xi(X = 0)$ to decay. As we increase $N_{\rm data}$, the memory effect is expected to be especially helpful when consecutive inputs share the same value, and thus should on average improve the information rate. This effect is not evident for extremely small $\tau_{\rm obs}$, where the error rate for $X = 0$ is too high to be corrected by the memory effect. However, the memory effect plays a significant role, bringing up to 30 percent increase in the average information rate, at intermediate $\tau_{\rm obs}$. All curves eventually converge in the long time limit as the memory effect wears off for times much longer than the propagation delay.

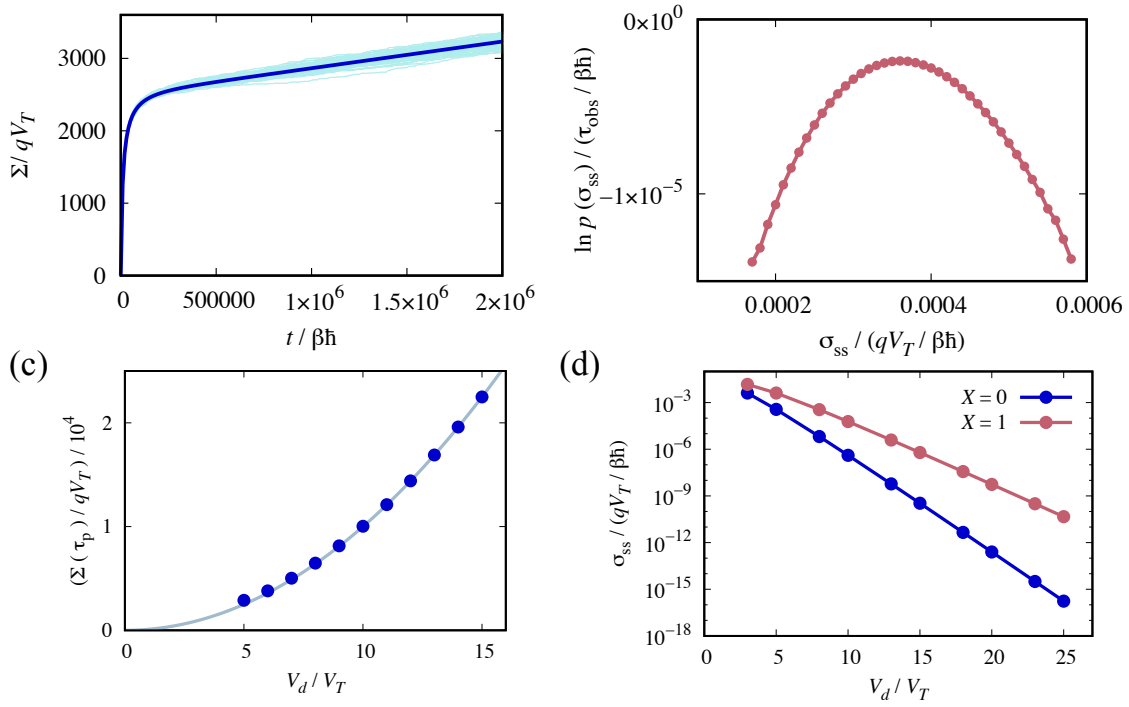

Figure 5.8: Entropy production of a NOT gate with V_g initialized to $0V_T$. (a) Evolution of the total entropy production for $V_d = 5V_T$ of 100 individual simulated trajectories (light blue) and their ensemble average (dark blue). (b) Distribution of the entropy production rate in the steady state, measured in the long time limit where $\tau_{\rm obs} = 10^6\beta\hbar$. (c) The entropy production during the propagation delay τ_p (dots) for $X = 0$, which converges to the quadratic function $C_g V_d^2/2$ (line) at high V_d. (d) The entropy production rate $\sigma_{\rm ss}$ in the steady state decreases exponentially with V_d for both $X = 0/1$.

The energy consumption for a gate can be quantified with the entropy production or the heat dissipated to the environment. From stochastic thermodynamics, the entropy production of the NOT gate during a long observation time $\tau_{\rm obs}$ can be computed by the product of electron current and its conjugate affinity from two separate pathways [217]

$$\Sigma(\tau_{\rm obs}) = \int_0^{\tau_{\rm obs}} dt\ J_{s\to \rm N}(\mu_s - \mu_g) + J_{d\to \rm P}(\mu_d - \mu_g)\,, \tag{5.24}$$

where $J_{s\to \rm N}$ is the electron current flowing from the source to the N-type transistor, and $J_{d\to \rm P}$ is the current from the drain to the P-type transistor (Eq. 5.13). In the process described in Fig. 5.5(a), the pathway through the N-type transistor is essentially blocked due to the high energy level of $\epsilon_{\rm N}$, so the main contribution in Eq. 5.24 is the second term in the sum. This second term has a similar form as the work required to quasi-statically charge the capacitor

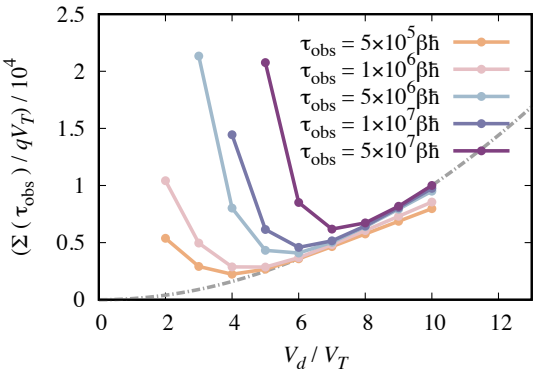

Figure 5.9: The total entropy production is a non-monotonic function of V_d for finite observation time τ_{obs}. The grey dashed line is the reversible limit $C_g V_d^2/2$.

from $V_g = 0$ to $V_g \approx V_d$, and thus is close to $C_g V_d^2/2$. This initial charging process is the dominant contribution to the total entropy production over short times, and represents the reversible limit of the NOT gate, shown in Fig. 5.8(c). Once the system reaches the steady state, there is still a steady entropy production coming from the leakage currents through both pathways, but the entropy production rate within the steady state is much smaller and decreases exponentially with V_d, seen in Fig. 5.8(d). This is because the output voltage V_{out} is very close to V_d, leaving the affinity across the drain and the output nearly zero. Further, the corresponding leakage current from the source to the output is small due to the high energy level ϵ_{N}. The contributions to $\Sigma(\tau_{\text{obs}})$ from V_d implies that for each observation time τ_{obs}, there exists an optimal V_d that minimizes $\Sigma(\tau_{\text{obs}})$, as confirmed in Fig. 5.9. The minimum V_d shifts to the right with increasing time as at higher V_d a larger contribution from the steady state flux counterbalances the higher entropy production during charging.

NAND Gate

We have presented a Markovian model for the NOT gate, which reproduces the performance of a perfect gate in the limit of high V_d and for which there is a complex interplay between energy consumption and time. Within the framework presented, it is straightforward to construct an analogous model of a NAND gate. A NAND gate takes in two binary inputs X_A, X_B, and outputs $Y = 0$ only when both inputs are 1. As shown in Fig. 5.10(a) and (b), the kinetic diagram, similar to the circuit diagram, is composed of two P-type transistors P_A, P_B, and two N-type transistors N_A and N_B. The NAND gate is described by four occupation numbers $(n_{\text{P}_A}, n_{\text{P}_B}, n_{\text{N}_A}, n_{\text{N}_B})$ and the gate voltage V_g. The energy levels of P_A and N_A depend on the first input voltage $V_{\text{in},A}$, while the energy levels of P_B and N_B are controlled

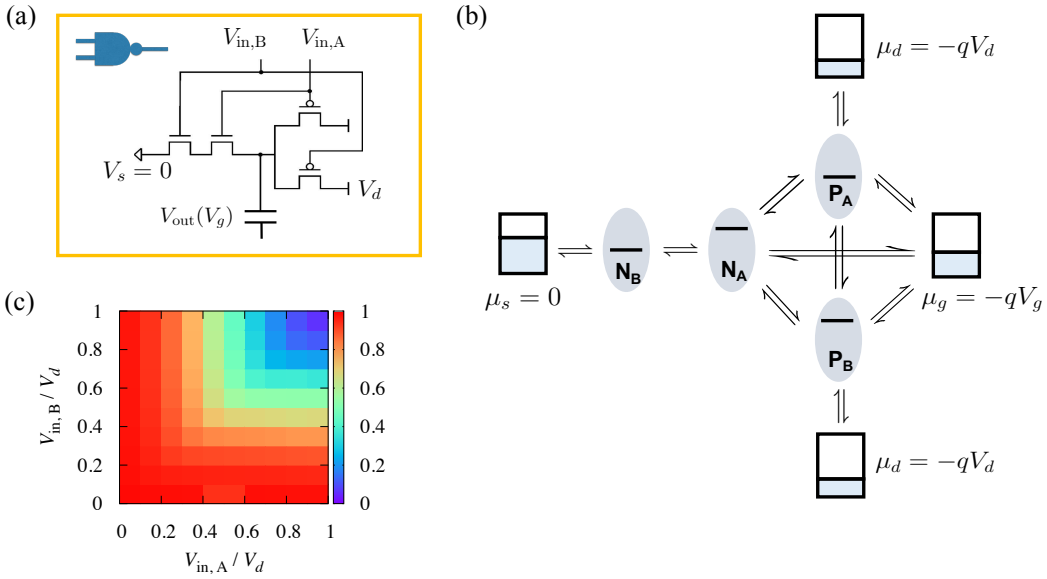

Figure 5.10: (a) Circuit diagram and (b) kinetic diagram of a NAND gate. (c) Two-dimensional voltage transfer curve at $V_d = 5V_T$.

by the second input $V_{\text{in},B}$ in the same manner as in Eq. 5.5,

$$\begin{aligned} \epsilon_{\mathrm{P}_A} &= \epsilon^0_{\mathrm{P}} + qV_{\text{in},A}\,, \quad & \epsilon_{\mathrm{N}_A} &= \epsilon^0_{\mathrm{N}} - qV_{\text{in},A}\,, \\ \epsilon_{\mathrm{P}_B} &= \epsilon^0_{\mathrm{P}} + qV_{\text{in},B}\,, \quad & \epsilon_{\mathrm{N}_B} &= \epsilon^0_{\mathrm{N}} - qV_{\text{in},B}\,. \end{aligned} \tag{5.25}$$

The transition rate between the transistors and reservoirs are described analogously to Eq. 5.9 and 5.10. To avoid numerical issues in Eq. 5.10 when the adjacent transistors have the same energy levels, we add a 10^{-3} regularizer in the denominator of the Bose-Einstein distribution $n(x)$. The output V_g is again treated as a capacitor described by Eq. 5.11, where the current J_g is the sum of $J_{\mathrm{P}_A\to g}$, $J_{\mathrm{P}_B\to g}$ and $J_{\mathrm{N}_A\to g}$, each defined as in Eq. 5.13. As in the NOT gate, both an average protocol and a Gillespie simulation consisting of 16 chemical reactions are used to study the dynamics. The entropy production during an observation time τ_{obs} is

$$\Sigma(\tau_{\text{obs}}) = \int_0^{\tau_{\text{obs}}} dt\; J_{s\to \mathrm{N}_B}(\mu_s - \mu_g) + (J_{d\to \mathrm{P}_A} + J_{d\to \mathrm{P}_B})(\mu_d - \mu_g)\,. \tag{5.26}$$

The two dimensional VTC for $V_d = 5V_T$ is shown in Fig. 5.10(c), which agrees with the truth table for a perfect NAND gate.

While the dynamical properties of the NAND gate are very similar to the NOT gate, an asymmetry arises in the NAND gate due to the different pathways in the kinetic diagram, which is a feature absent in the NOT gate. Consider the three different inputs $(X_A, X_B) = (0,0), (1,0)$ and $(0,1)$ shown in Fig. 5.11(a) for $V_d = 5V_T$. While for a perfect NAND gate,

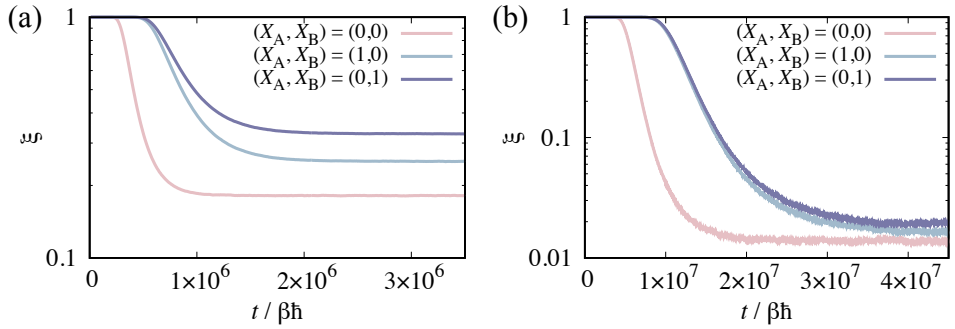

Figure 5.11: Decay of the error rate with time under three cases: $(X_{\text{in,A}}, X_{\text{in,B}}) = (0,0), (1,0)$ and $(0,1)$ for (a) $V_d = 5V_T$ and (b) $V_d = 8V_T$ for a NAND gate initialized with $V_g = 0V_T$.

these three inputs should all correspond to the output $Y = 1$, the evolution of the error rate ξ and its converged values in the steady state are not exactly the same for finite V_d. In the case of $(X_A, X_B) = (0,0)$, as both P_1 and P_2 have relatively low energy levels, there are two pathways to charge the capacitor, resulting in a faster error decay rate. For the cases $(X_A, X_B) = (0,1)$ and $(1,0)$, one of the pathways is blocked due to the high energy level of the P transistor, so the error rate decays much slower reflecting the slower charging of the capacitor. While the latter two cases also differ slightly due to the asymmetry in N_1 and N_2, such differences shrink drastically when we increase V_d to $8V_T$ in Fig. 5.11(b). The three cases now converge to similar error rates in the steady state. In fact, as we further increase V_d, all such asymmetries vanish, another example of which can be found in Fig. 5.12, where we plot the one dimensional cut of the VTC along the line $V_{\text{in},A} = V_{\text{in},B}$ for different V_d. As in the case of the NOT gate, our model behaves as a perfect NAND gate as V_d approaches $1e$V. For clarification, we define the propagation delay τ_p of a NAND gate as the time required to reach the threshold αV_d for the input $(X_A, X_B) = (0,1)$, which is close to τ_p for the NOT gate of the same V_d.

5.4 Logic Circuits

Equipped with a model for the NOT and NAND gate, we now in principle have the tools to implement arbitrary logic functions. While any logic function can be represented in multiple ways, the topology of the circuit has an influence on its accuracy, and thermodynamic costs [212]. In the following section, we first explore spatial propagation effects arising from assembling multiple gates in a combinational circuit, and then demonstrate memory effects arising from the feedback loop in a sequential circuit. Understanding the behavior of these basic computing circuits will be crucial to building up a computing device.

For each logic circuit, which is itself a computing module made up of multiple logic gates, while each gate has an intermediate output, we reserve the symbol V_{out} for the specific V_g

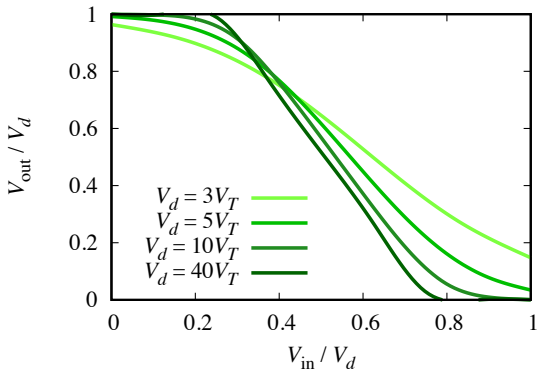

Figure 5.12: The voltage transfer curve of the NAND gate along the one dimension $V_{\text{in}} = V_{\text{in,A}} = V_{\text{in,B}}$, which becomes more symmetric as V_d increases.

that corresponds to the overall output Y of the module. Intermediate input and output voltages are not converted to binaries except for the final output V_{out}. While the output of each gate is used as the input of the ensuing gate, we neglect the back reaction on V_{out} so that the occupation of the ensuing transistors does not affect V_{out}, which is consistent with the high capacitance assumption made in Eq. 5.5. Unless specified otherwise, all gates are initialized at $V_g = 0V_T$ at the start of the computation, but no re-initialization is done afterwards. While the channel capacity is a more comprehensive characterization of the accuracy and provides the best case scenario, the much larger input space and complicated memory effects make it cumbersome to calculate in the case of logic circuits. We thus use the error rate in the final output instead, and consider the worst case scenario in choosing the inputs to provide an upper bound for the error rate whenever possible.

Combinational Circuit

A combinational circuit maps a given set of inputs to a single output using a number of gates, such as an adder that computes the sum of inputs and a XOR gate that computes their parity. As the simplest example, we study the behavior of an array of L NOT gates indexed by $i = 1, 2, \cdots, L$ connected in the way that $V_{\text{in}}^{(i)} = V_g^{(i-1)}$ for $i > 1$. A schematic of the system can be found in Fig. 5.13(a). The input of the circuit X determines $V_{\text{in}}^{(1)}$, and the output is measured from the last gate $V_{\text{out}} = V_g^{(L)}$. The spatial dimension adds complexity to the evolution of V_g, as illustrated in Fig. 5.13(b) for $V_d = 5V_T, X = 0$. In the steady state, we expect the output voltage of the odd gates close to V_d, and the even gates close to zero. For a gate to reach its steady state, its input, which depends on the dynamics of the previous gate, must first reach its expected value, thus the propagation delay should increase with the gate index i. As the odd gates are initialized far from its steady state, it will take a significant amount of time to reach its expected output. For the odd gates which have not

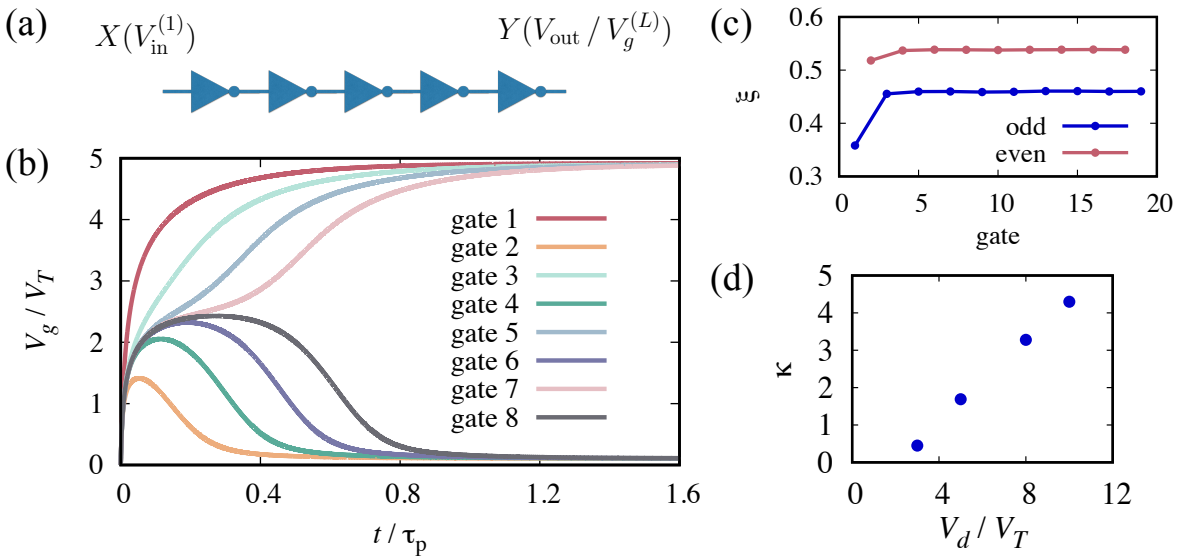

Figure 5.13: Performance of an array of NOT gates with $X = 0$, and all V_g initialized to $0V_T$. (a) Schematic of an array of NOT gates with a single input X and output Y. (b-c) Evolution of V_g (b), and the steady state error rate (c) for individual gates with $V_d = 5V_T$. (d) Spatial propagation rate κ as a function of V_d.

reached the steady state yet, the ensuing even gate will have a lower input voltage, resulting in the overshoot of voltage before eventually decaying to its expected lower output. The turn over in voltage of the even gates corresponds to the inflection point on the VTC.

A consequence of the connectivity between gates is the corruption of initial input. While the input voltage of the first gate is always $0V_T$, for finite V_d, the maximum input voltage of the second gate will be slightly lower than V_d, and thus corrupted. As the VTC of the NOT gate is a non-increasing function, a corrupted input will inevitably cause a higher error rate in the output, which will propagate along the array. This is shown in Fig. 5.13(c), where the error rate for individual gates in the steady state rises initially with gate index, before converging to a constant value after a few gates, and is always higher than that of the single gate. A similar behavior can be found in the propagation delay time shown in Fig. 5.14(a), which increases sharply for the first few gates and converges to a slower linear increase afterwards. This implies that circuit designs with deeper layered structure are unfavorable in terms of both accuracy and propagation delay.

The convergence behavior is intriguing as it implies the existence of a pair of fixed points $(V_{\rm odd}^*, V_{\rm even}^*)$ for the intermediate outputs in the steady state. Indeed, the fixed point solution corresponds to the point on the VTC $(V_{\rm in} = V_{\rm odd}^*, V_{\rm out} = V_{\rm even}^*)$ satisfying the condition that its reflection $(V_{\rm in} = V_{\rm even}^*, V_{\rm out} = V_{\rm odd}^*)$ is also on the VTC. As the fixed point is a dynamically stable solution, it does not depends on the initial input $V_{\rm in}^{(1)}$, as shown in Fig. 5.14, whereas

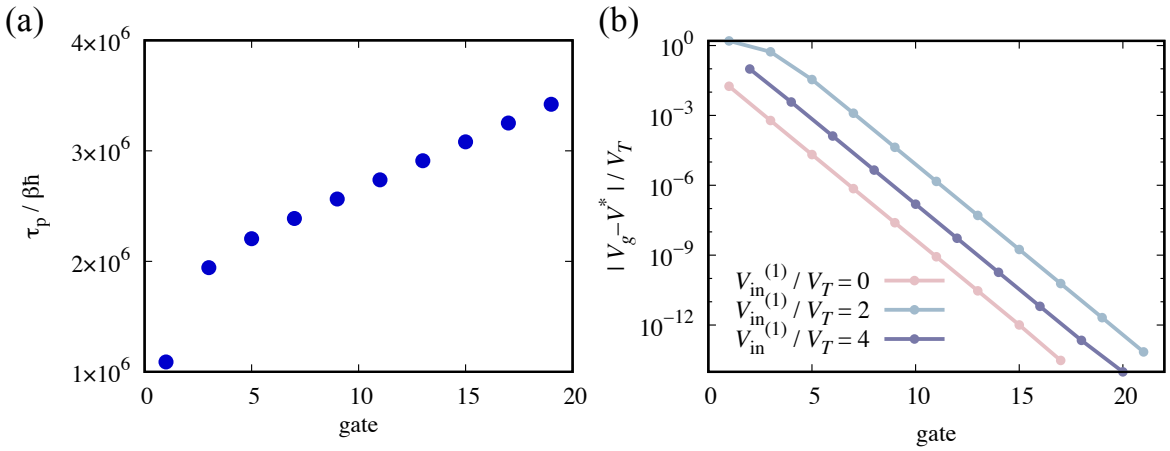

Figure 5.14: Spatial propagation in an array of NOT gates with $V_d = 5V_T$ and all V_g initialized to $0V_T$. (a) Propagation delay for the odd gates with $X = 0$. (b) Exponential decay of the distance between V_g and the fixed point. The spatial propagation rate κ is duduced from the rate of the exponential decay, which is independent of the input $V_{\text{in}}^{(1)}$.

the speed of approaching the fixed point characterizes the spatial correlation in the system. We fit the decay in $|V_g^{(i)} - V^*|/V_T$ with an exponential function $\exp[-\kappa i]$, and report the rate κ for different V_d in Fig. 5.13(d). For $V_d = 5V_T$, the spatial correlation length $1/\kappa$ is on the order of 1, which means spatial correlation exists between neighboring gates. As the VTC becomes sharper with increasing V_d, the correlation length between gates decreases. In the limit of high V_d, the fixed point solution can be found exactly at $(V_{\text{in}} = 0, V_{\text{out}} = V_d)$, which means that the input becomes uncorrupted. To summarize, the combination of gates introduces longer propagation delay and input corruption, and thus deeper layered circuit design is advised against. By operating at a higher V_d to reduce spatial correlation, the latter problem can be mitigated, but of course this is done at the cost of even longer propagation delay.

As a consequence of the spatial correlation, it is more probable to observe consecutive errors along the array, which can be illustrated by an error analysis of simulated trajectories. We simulate an array of NOT gates of length L with $V_{\text{in}}^{(1)} = 0V_T$, $V_d = 5V_T$, and generate more than 10^8 snapshots of the system. For each snapshot, we first search for regions with $d_e = 1, 2, \cdots, 16$ consecutive errors, and then count the total number of such error domains, denoted by $N(d_e)$. While counting, we do not account for the first 10 gates in each array as they have not reached the fixed point solution. To characterize spatial correlation in the system, we compare the value of $N(d_e+1)/N(d_e)$ computed in our model with the case where all gates are independent from each other. We denote the single gate error rate of the odd and even gates as $\xi_{0/1}$. Note that to make a fair comparison, this error rate corresponds to the fixed point solution of the array, instead of the error rate of a single NOT gate with $X = 0/1$. Assuming odd and even gates are observed with equal probability, it is easy to derive that

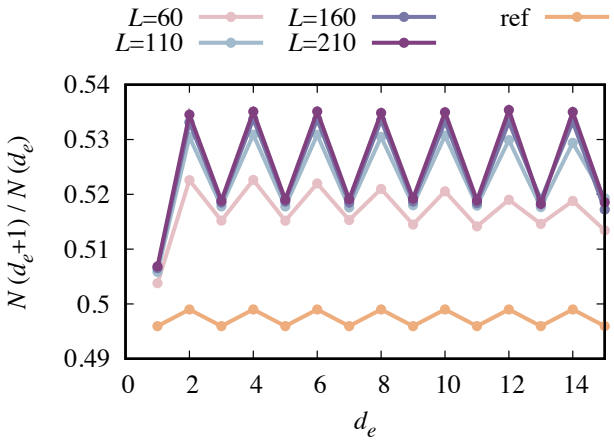

Figure 5.15: The ratio $N(d_e+1)/N(d_e)$ as a function of d_e calculated for an array of NOT gates of length $L = 60, 110, 160$ and 210 with $V_d = 5V_T$. The orange dots represent the reference where all gates are independent from each other, and alternates between $2\xi_0\xi_1/(\xi_0+\xi_1)$ and $(\xi_0+\xi_1)/2$.

$N(d_e = 1) = (\xi_0+\xi_1)/2$ and $N(d_e = 2) = \xi_0\xi_1$. One can infer from this simple calculation that for independent gates, $N(d_e+1)/N(d_e) = 2\xi_0\xi_1/(\xi_0+\xi_1)$ if d_e is odd, $(\xi_0+\xi_1)/2$ if d_e is even. This result is plotted in Fig. 5.15 as the reference, where the zigzag behavior comes from the difference between ξ_0 and ξ_1. In addition, we plot in the same figure the value $N(d_e+1)/N(d_e)$ for our model with $L = 60, 110, 160$ and 210. For smaller L, as finite size effect prevents larger error domains to emerge, the value $N(d_e+1)/N(d_e)$ is lower and decays with d_e. Such effect mitigates with increasing L, and the value of $N(d_e+1)/N(d_e)$ should not depend on the exact value of d_e other than its parity in the $L \to \infty$ limit. The converged values of $N(d_e+1)/N(d_e)$, as shown in Fig. 5.15, is clearly higher than the reference values, indicating that there exists a positive correlation in errors between adjacent gates. In other word, given that an error occurs at gate i, the probability of observing another error at its neighboring gate is enhanced due to the spatial correlation.

Sequential Circuit: RS latch

While combinational circuits are typically used to carry out arithmetic computations, modern computing devices often include another type of logic circuit to handle memory - the sequential circuit. Fig. 5.16(a) shows an example of such a circuit, known as the RS latch. The RS latch consists of two NAND gates where the output of gate 1, $V_g^{(1)}$, is sent as an input of gate 2, $V_{\text{in,A}}^{(2)}$, and similarly, the output of gate 2, $V_g^{(2)}$, is fed back as $V_{\text{in,B}}^{(1)}$. The remaining two inputs, $V_{\text{in,A}}^{(1)}$ and $V_{\text{in,B}}^{(2)}$, corresponds to the two external binary inputs X_{S} and X_{R}, respectively. The output of the circuit, V_{out}, which coincides with $V_g^{(1)}$, depends not only on the external

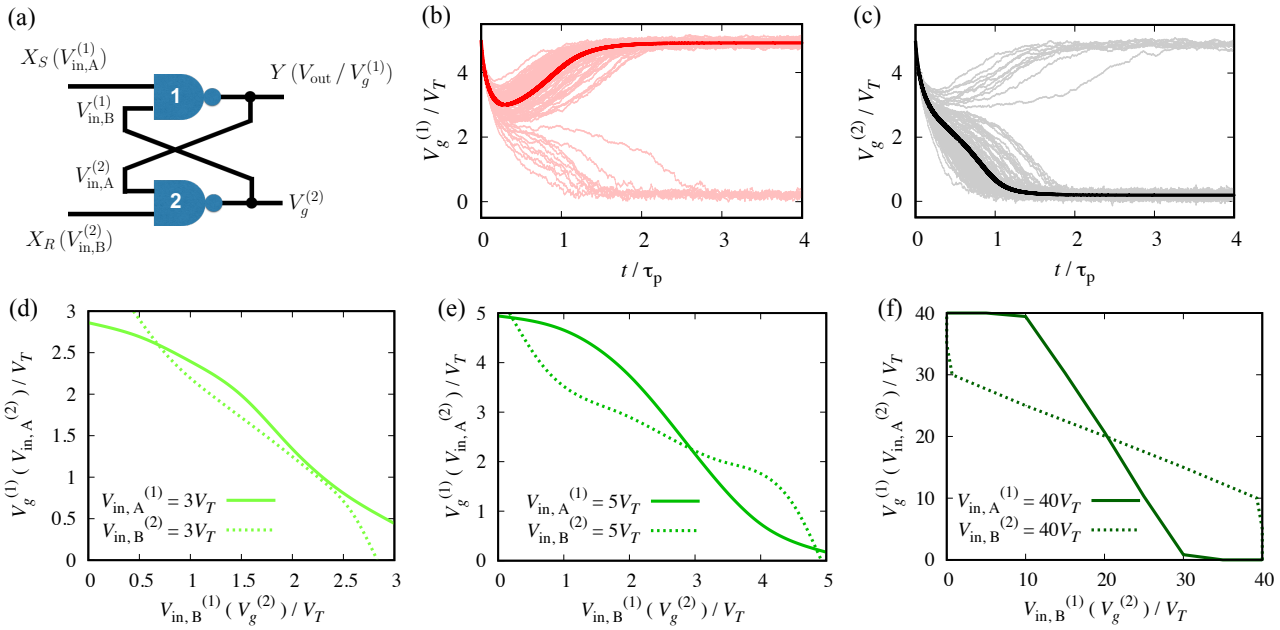

Figure 5.16: (a) Circuit diagram of the RS latch. (b-c) The evolution of the outputs $V_g^{(1)}$ and $V_g^{(2)}$ for 100 trajectories with the initialization $V_g^{(1)} = V_g^{(2)} = V_d = 5V_T$, where time is scaled by the propagation delay τ_p of the NAND gate. The dark curve represents the average relaxation behavior. (d-f) The location of the stable informational states determined by overlapping the VTC for the two NAND gates at (d) $V_d = 3V_T$, (e) $V_d = 5V_T$, and (f) $V_d = 40V_T$.

inputs $X_{\rm S}$ and $X_{\rm R}$, but also the stored information of $V_g^{(1)}$ and $V_g^{(2)}$. This is the defining characteristic of a sequential circuit, which makes it useful as a memory storage. More specifically for a perfect RS latch, in the "set" stage where the external inputs are set as $X_S = 0$, $X_R = 1$ or $X_S = 1$, $X_R = 0$, there exists only one dynamically stable state for the system, so that we can unambiguously designate the memory at $V_{\rm out}$ as 1 or 0. In the "hold" stage where $X_S = X_R = 1$, however, the system is bistable and its state depends on the initialized value of $V_g^{(1)}$ and $V_g^{(2)}$. In the vicinity of the fixed points, an effective Hamiltonian description of the RS latch is quartic in $V_{\rm out}$ with two minima and a maxima between them [232]. This emergent bistability resulting from the feedback loop allows the RS latch to function as a memory storage device.

To function as a memory storage device, a circuit must have at least two distinguishable states in which information can be stored. For our stochastic model in Fig. 5.16(a), these states correspond to the steady state solutions that satisfy the feedback condition $V_{\rm in,B}^{(1)} = V_g^{(2)}$, $V_{\rm in,A}^{(2)} = V_g^{(1)}$ under the input $V_{\rm in,A}^{(1)} = V_{\rm in,B}^{(2)} = V_d$. An intuitive way to find their location is to overlap the VTC of the two NAND gates along the cut $V_{\rm in,A}^{(1)} = V_d$ and $V_{\rm in,B}^{(2)} = V_d$, which

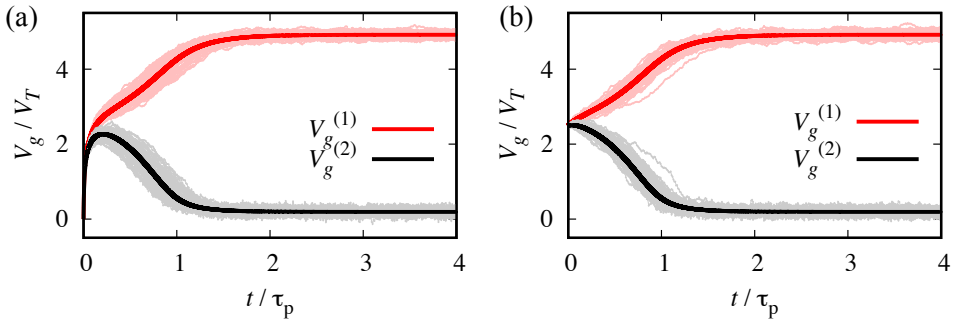

Figure 5.17: The evolution of the outputs $V_g^{(1)}$ and $V_g^{(2)}$ with the initialization (a) $V_g^{(1)} = V_g^{(2)} = 0V_T$ and (b) $V_g^{(1)} = V_g^{(2)} = 2.5V_T$ where $V_d = 5V_T$. The dark curves represent the steady state solution from the average protocol, while the lighter curves represent 100 trajectories. In both cases, the percentage of trajectories that end up in the other informational state $(V_g^{(1)}, V_g^{(2)}) = (0.20V_T, 4.89V_T)$ is less than 10^{-5} among the 2.56×10^6 trajectories simulated.

are not exactly the same due to the asymmetry in the non-perfect NAND gates. We show a couple of scenarios at different V_d in Fig. 5.16(d-f). At $V_d = 3V_T$, the highly asymmetric VTCs cross merely at $(V_{\text{in,B}}^{(1)}, V_{\text{in,A}}^{(2)}) = (0.67V_T, 2.61V_T)$, indicating that the system only has a single stable state and does not qualify as a memory storage device. As V_d increases to $5V_T$, two dynamically stable informational states start to emerge at $(V_{\text{in,B}}^{(1)}, V_{\text{in,A}}^{(2)}) = (0.19V_T, 4.92V_T)$ and $(4.89V_T, 0.20V_T)$, though the slight asymmetry suggests different dynamics around the two states. While a third intersection point is found at $(V_{\text{in,B}}^{(1)}, V_{\text{in,A}}^{(2)}) = (2.93V_T, 2.26V_T)$, it corresponds to an unstable saddle point. At an even higher $V_d = 40V_T$, the two states converge to $(V_{\text{in,B}}^{(1)}, V_{\text{in,A}}^{(2)}) = (0V_T, 40V_T)$ and $(40V_T, 0V_T)$, and symmetry is restored.

While the existence of two distinguishable informational states is guaranteed at sufficiently high V_d, there remains the question of whether these informational states are robust against noises. While in both the set and hold stage, $V_g^{(1)}$ and $V_g^{(2)}$ are usually sufficiently far from each other that it is possible to distinguish them definitively, there do exist occasions where the noise can mediate a transition. One such example is shown in Fig. 5.16(b) and (c) for the initialization $V_g^{(1)} = V_g^{(2)} = V_d = 5V_T$. As the outputs of the gates evolve from their initialization towards the steady state solution, there is a significant overlap between the two outputs around $t = 0.5\tau_p$, which leads to about 13% percent of the trajectories failing to retain the information and evolving to the wrong fixed point. This kind of perturbation happens when the overlap region includes the unstable intersection point on the VTC, and the change of convexity of the effective Hamiltonian brings the trajectory towards a different stable state. Such an initialization error is rare to observe either in the set or hold stage, and we show additional evidence for the robustness of the circuit at $V_g^{(1)} = V_g^{(2)} = 2.5V_T$ and $0V_T$ in Fig. 5.17. In addition, at a higher V_d, as the VTC becomes sharper, not only do the two minima in the Hamiltonian become more separated, their vicinity also become steeper, both

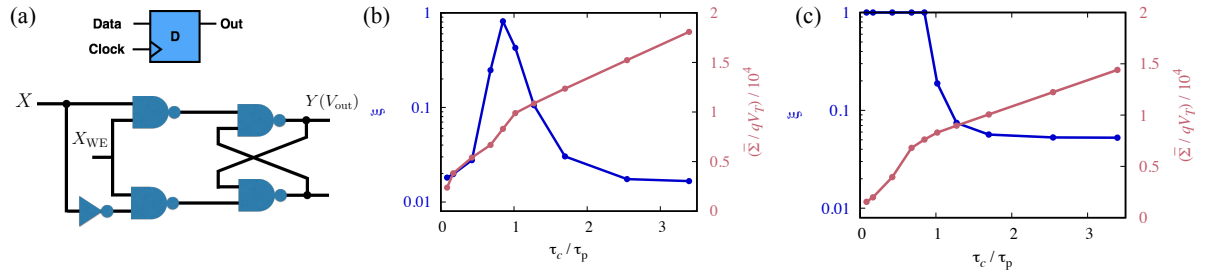

Figure 5.18: (a) The symbol (left) and circuit diagram (right) of a D flip-flop. (b-c) Error rate (blue, with axis label on the left) and average dissipation per gate per cycle (red, with axis label on the right) as a function of the clock cycle τ_c, scaled by the propagation delay of the NAND gate, for cycles with input (b) $X = 1$ and (c) $X = 0$. All NAND gates are operated at $V_d = 8V_T$.

of which facilitate the differentiation between the two states and thus will drastically improve the robustness of the device.

Sequential Circuit: D flip-flop

With the RS latch as a basic computing unit, we can model a memory storage module that synchronizes with the clock generator, called the D flip-flop. Modern computing devices typically include a pulse generator that oscillates between 0 and 1, with a clock cycle τ_c. To see how the clock is incorporated into the D flip-flop, we show the circuit diagram of a D flip-flop in Fig. 5.18(a), built up from 4 NAND gates and 1 NOT gate. The circuit can be readily modularized as a memory storage unit, denoted with the symbol D, that takes in an input X representing the data, another input $X_{\rm WE}$ synchronized with the clock, and generates an output Y. The two NAND gates with the feedback loop on the right hand side constitute an RS latch, which is responsible for the memory storage. When the write-enable input $X_{\rm WE} = 1$, the D flip-flop sets its output $V_{\rm out}$ in agreement with the data X, whereas when $X_{\rm WE} = 0$, the D flip-flop holds its stored value as its output, which can be further processed for computing purposes.

The clock cycle τ_c, or the clock frequency $1/\tau_c$, is an important parameter as it determines how fast data can be read and stored. In Fig. 5.18(b) and (c) we illustrate how the clock cycle influences the accuracy and dissipation of the data transmission process for a D flip-flop with $V_d = 8V_T$. We start with $X_{\rm WE} = 1$ and send in a stream of data $\mathbf{X} = \{1, 0, 1, 0, \cdots\}$. While $X_{\rm WE}$ alternates between 1 and 0 every $\tau_c/2$, the data input only changes every τ_c. This input data sequence is chosen to maximize the alternation in the output, and thus minimize the memory effect discussed earlier for the NOT gate. Therefore, the error rate and dissipation in this case are expected to be the highest among all possible input sequences. The error rate ξ is measured according to the output $V_{\rm out}$ at the end of each cycle, and is

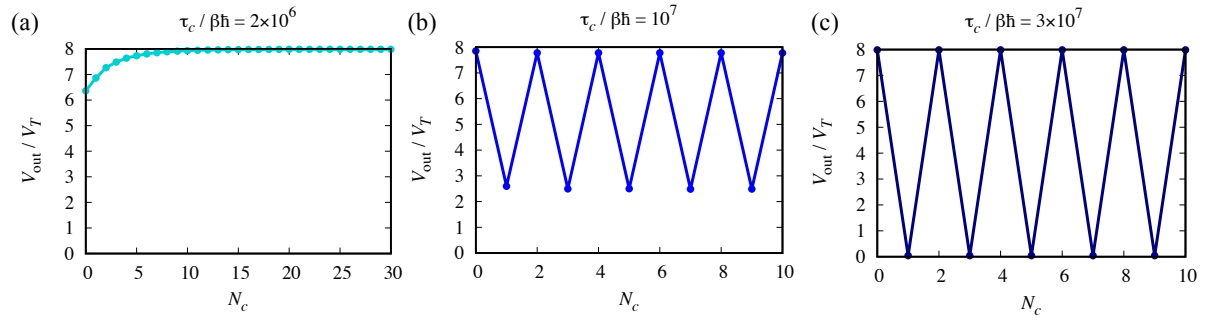

Figure 5.19: Output voltage of a Dflipflop with clock cycle (a) $\tau_c = 2 \times 10^6 \beta\hbar$, (b) $\tau_c = 10^7 \beta\hbar$, and (c) $\tau_c = 3 \times 10^7 \beta\hbar$. The input data sequence starts from $X_{\text{data}} = 1$ and alternates between 1 and 0. All gates are operated at $V_d = 8V_T$, and are initialized with $V_g = 0V_T$. We discard the first few cycles and average over more than 50 cycles when computing the average error rate and dissipation in Fig. 5.18, so that their values have no dependence on the initialization.

reported separately for the cycles with $X = 1$ and 0. The evolution of V_{out} as a function of the cycle number can be found in Fig. 5.19.

Similar to the behavior for the single NAND gate in Fig. 5.11(b), the error rate for $X = 0$ starts to decrease monotonically when τ_c is longer than the single gate propagation delay τ_p. The error rate for $X = 1$, however, first increases with τ_c before eventually decreasing. This counter-intuitive behavior comes from the memory retention behavior in the RS latch. Once data is stored in the RS latch, it tends to stay in the memory by influencing the transmission of the following data, and thus introduces temporal correlation between the outputs. The influence of the data can only be erased given sufficient time to transmit the following data. This temporal correlation time, or memory retention time, again coincides with the propagation delay τ_p. In this example, as the first input $X = 1$, the output retains the memory of a higher output at short τ_c, so the error rate for $X = 1$ is deceptively low, and the error rate for $X = 0$ is high. At $\tau_c \approx \tau_p$, the output is stuck between the high and low outputs before reaching either steady state, so that the error rate for either cycle is high. In this regime, the average dissipation accumulated within each cycle rises fast with τ_c, as charging processes contribute heavily to energy costs. When $\tau_c > \tau_p$, the memory effect is eventually overcome and the error rates for both cycles start to decay. The average dissipation rate also converges to a smaller constant value as within each cycle, the system is able to reach the steady state, in which much less dissipation is generated. The exponential scaling of τ_p with V_d implies that while the asymptotic error is expected to decrease when operating far from thermal energies $V_d \gg V_T$, the speed with which the D flip-flop can function with that lower error is significantly slower. Due to this lag, comparing between a lower and a higher V_d, the error is expected to be much lower in the former case for a fixed computing time on the order of τ_p of the lower V_d.

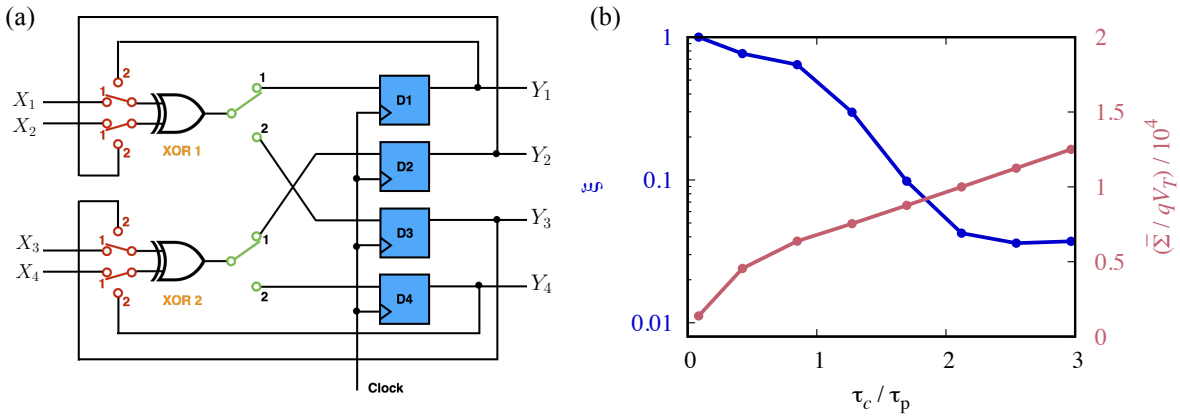

Figure 5.20: (a) Schematic of the parity computing device with 2 XOR gates and 4 D flip-flops. The input of each XOR gate is controlled by 2 input two-way switches, shown in red. The output two-way switch, shown in green, determines which D flip-flop is used to store the output of the XOR gate. (b) The average error rate (blue, with axis label on the left) and dissipation per gate per cycle (red, with axis label on the right) as a function of the time cycle τ_c, scaled by the propagation delay of a single NAND gate, averaged over different input sequences. All gates are operated at $V_d = 8V_T$.

5.5 Computing Devices

With the combinational circuit modularized as the arithmetic logic unit (ALU), and the sequential circuit as the memory storage device, we can combine the two components to model a computing device. We choose the task of computing the parity of a sequence of inputs $\mathbf{X} = \{X_1, X_2, \cdots, X_N\}$ of length N, which has wide applications in error detection. Such a task can be easily implemented by combining $(N-1)$ XOR gates in a sequential manner. However, when N is relatively large, due to the limitation in resources, it is beneficial to break up the task in several steps, and store intermediate results in memory. The clock generator synchronizes the operation of different components to ensure correct sequencing.

As an example, we consider 2 XOR gates as an ALU, and 4 D flip-flops, D1 to D4, as a memory device to check the parity of $N = 12$. Fig. 5.20(a) shows the schematic of our design, while the complete circuit diagram can be found in Fig. 5.21. Each XOR gate takes in 2 binary inputs at a time, the source of which is controlled by 2 input two-way switches, shown in red in Fig. 5.20(a). When the switch is connected to terminal 1, the input comes from the data sequence $\mathbf{X}$; whereas when terminal 2 is connected, the input comes from the data stored in a D flip-flop. At the end of each XOR gate is an output two-way switch, shown in green in Fig. 5.20(a), which controls where to store the output. We store new data only on free D flip-flops, where the data stored at an earlier time is already read out for post-processing and does not need to be held any more. The total system requires modeling over 100 transistors.

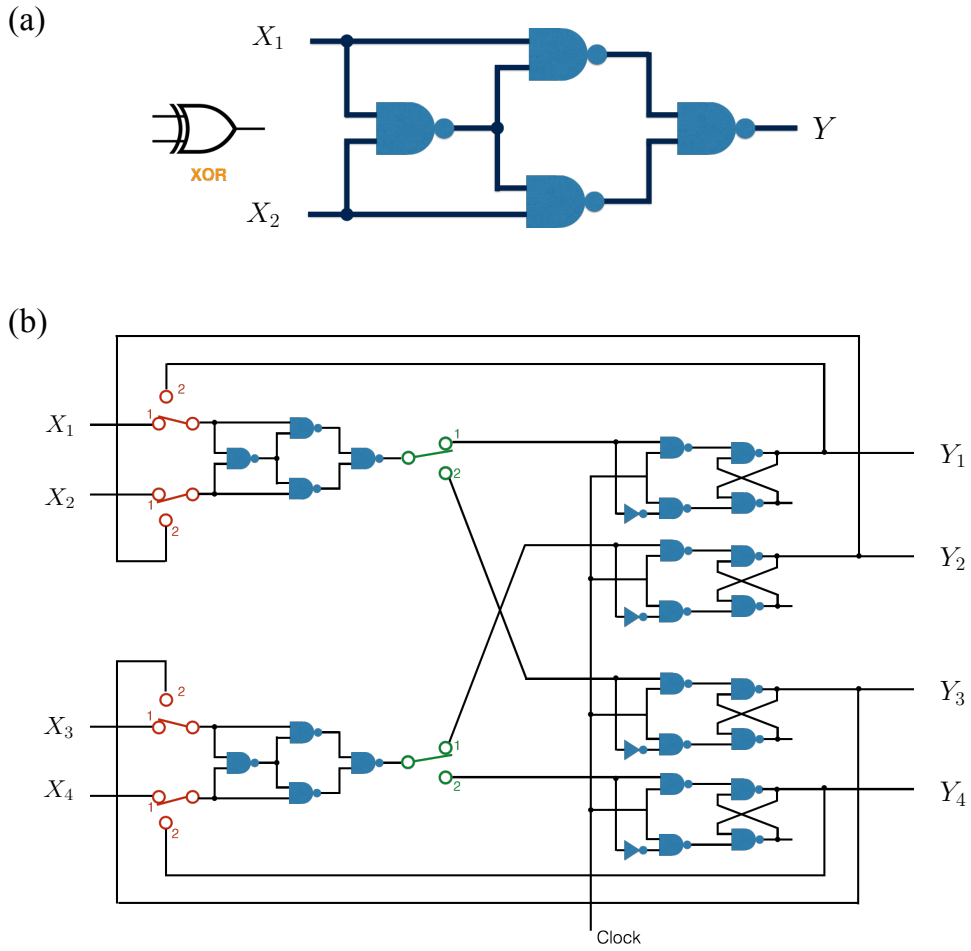

Figure 5.21: (a) Symbol (left) and circuit diagram (right) of a XOR gate, which takes in two inputs X_1, X_2, and compute their parity as output Y. (b) Circuit diagram of the parity computing device with 2 XOR gates and 4 D flip-flops.

We start the computation by sending in pairs of input data from the data sequence, and computing their parities with the XOR gates. The D flip-flops are set by outputs from the ALU (first D1, D2 and then D3, D4), and once all D flip-flops have been set, we free them by sending the stored information back to the ALU for further processing. The computation is terminated when all inputs are taken into account in the final output, and the entire task can be completed in 6 clock cycles. A computational tree graph that illustrates how intermediate outputs are related to the final output can be found in Fig. 5.22, with 12 input nodes in the 0th layer representing the input data, and a single final output $l_4^{(1)}$ that computes the parity of the inputs. The nodes in layer 1 to 3 represent intermediate computation results.

For concreteness, we consider the input sequence $\mathbf{X} = \{0, 0, 1, 1, 0, 1, 0, 0, 1, 0, 0, 0\}$ and plot in Fig. 5.23 the V_{out} of the XOR gates, D1 and D2, for an ensemble of trajectories.

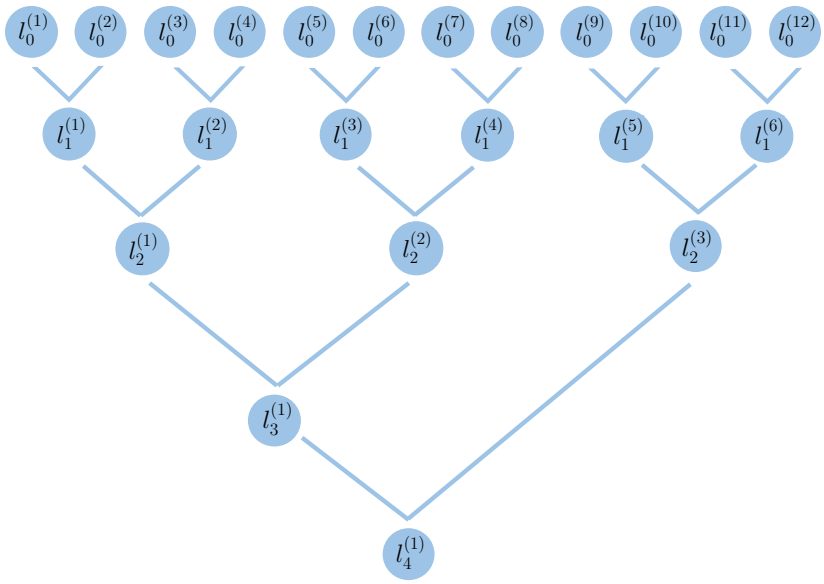

Figure 5.22: Computational tree graph of the device that computes the parity of 12 input data. The node $l_i^{(j)}$ denotes the jth output of the ith layer. The 0th layer has 12 nodes, which represent the 12 data in the input sequence. Each child node calculates the parity of its two parent nodes. The final output $l_4^{(1)}$ computes the parity of all the input data.

Here the clock cycle is chosen as $\tau_c = 10^7\beta\hbar$. All gates are operated at $V_d = 8V_T$, while all capacitors are initialized with zero charge. We highlight with red cross the time points where outputs are being read out from the D flip-flops. At $t = 0$, we send in 4 input data, X_1 to X_4, by connecting all the input two-way switches to terminal 1. Since all the D flip-flops are slack at the moment, we can store the computing results of the XOR gates into D1 and D2 by switching both output two-way switches to terminal 1 as well. The clock stays at 0 within the first half cycle while computations are being done at the ALU, until $t = \tau_c/2$, when the clock switches to 1 and the outputs of the ALU are being written into D1 and D2. At $t = \tau_c$, as the clock returns to 0, another 4 input data are sent in while the output two-way switches are connected to terminal 2 so that outputs can be sent to and stored at D3 and D4. At the end of the second cycle, when we realize that our memory devices are full and can not take in new inputs, we read out the outputs at D1 to D4 and send them back to the ALU as inputs by connecting all input two-way switches to 2. We continue the computation in this manner, until all input data are taken into account and the final output is read from D1 at $t = 6\tau_c$.

As before, we are interested in the time and dissipation required to achieve a certain accuracy. In Fig. 5.20(b), we show the error rate for the final output at $t = 6\tau_c$, and the average dissipation per gate (averaged over the 28 gates in this device) per clock cycle $\bar{\Sigma}$ as a function of τ_c with $V_d = 8V_T$. Both results are averaged over more than 10^4 inputs, which are sequences of independent and identically distributed Bernoulli random variables with equal probability of being 0 or 1. As expected, the average error rate decays with the

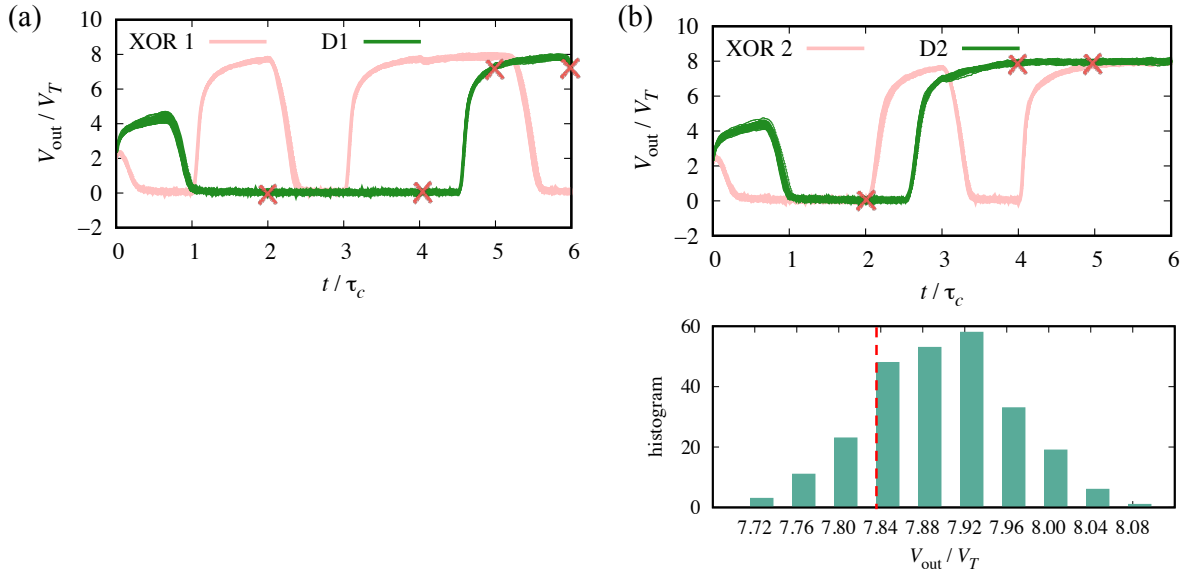

Figure 5.23: (a) For the input sequence $\mathbf{X} = \{0, 0, 1, 1, 0, 1, 0, 0, 1, 0, 0, 0\}$, the output of XOR 1 and its corresponding memory storage D1 for 64 individual trajectories at $V_d = 8V_T$, $\tau_c = 10^7\beta\hbar$. The red crosses label points where outputs on D1 are read out for further processing. (b) The output of XOR 2 and its corresponding memory storage D2 with the same parameters as in (a). The lower plot shows the histogram of outputs at D2 at $t = 4\tau_c$. The red dotted line labels the threshold under which the output corresponds to an error.

clock cycle until $\tau_c \approx 3\tau_p$, as the extended spatial dimension of the circuit increases the propagation delay in the final output. At such a high V_d, spatial correlations do not extend beyond neighboring gates, and are even weaker between different modules, especially for clock cycles longer than τ_p. The average dissipation first increases sharply and then converges to a linear growth in the limit of large τ_c, similar to the D flip-flop, but slightly lower than that in Fig. 5.18(c) for the same τ_c. This is because the input sequences are randomly chosen instead of alternating between 0 and 1, and the memory effect can help shorten the charging process, which most contributes to the entropy production. Additionally because of the synchronization, the D flip-flops may remain at a steady state for a few cycles before it is freed to store new data. During such periods, the dissipation is especially low as the entropy production in the steady state is minimal due to relatively small leakage currents. Therefore, computational protocols that minimize changes on the memory storage device is desirable for low-dissipation computing. Taking into consideration both the accuracy and dissipation, the optimal clock cycle to operate with is $\tau_c \approx 2\tau_p$, as lowering the speed further will only result in higher dissipation from the steady state.

In the computational tree graph in Fig. 5.22, if an error is observed in any of the nodes whose layer is deeper than 0, we look further at its parent nodes to trace where the error

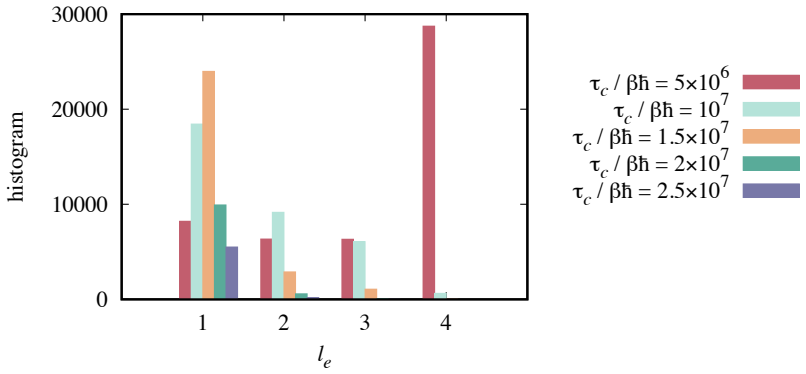

Figure 5.24: Histogram of error paths of length l_e for different clock cycle τ_c.

originates, and its child node (if existing) to see how far the error propagates. We call such a record of error vertically along the computational tree graph an error path, and its length is denoted as l_e. In this computational tree graph, the maximum value for l_e is 4, which means the error propagates from layer 1 all the way to the final output; while the minimum value for l_e is 1. Among the 1.28×10^4 simulations we have done with different input sequences, we make a histogram of the error paths with length l_e for different clock cycle τ_c, which is shown in Fig. 5.24. For the shortest clock cycle plotted $\tau_c = 5 \times 10^6 \beta\hbar$, which is too soon for the gates to reach their steady states, we observe an overwhelmingly high number of error paths of length $l_e = 4$. However, when τ_c is longer, we see an exponential decay in the number of error paths with increasing l_e. This exponential decay rate characterizes the temporal correlation between intermediate computation results. The rate increases with longer τ_c, indicating the diminishing correlations, or the weakening of the memory effect at longer clock cycle. With $\tau_c > 2 \times 10^7 \beta\hbar$, it is almost impossible to find an error path with $l_e = 4$ that propagates through the computational tree graph.

5.6 Conclusion

We have illustrated a realistic model for stochastic logic gates, and demonstrated its utility in building arbitrary logical circuits. Information manipulations, such as bit storage and erasing are represented by the charging and discharging of the capacitors, which is consistent with current data storage technology. While our model performs as a perfect logic circuit when operated in the limit of low noise, its thermodynamical consistency allows us to study the rich interplay between speed, accuracy and dissipation in the intermediate regimes, from which we can derive some useful design principles for low dissipation computing devices. For instance, we have provided a physical origin of input corruption in the combinational circuits, as well as feedback robustness in the sequential circuits, and illustrated how each can be improved drastically by operating at a slightly higher voltage. In addition, memory effects

should be exploited as much as possible to minimize dissipation. With modularization, it is straightforward to scale up our model to even larger and more complex systems, making it a useful model to study collective behaviors of circuits.

One of the major motivations of this work is to enable the design of low dissipation computing devices with maximal accuracy and speed. While there exists several theoretical results that propose bounds on the thermodynamic costs of computing [182, 212], understanding under what circumstances they are saturated requires a realistic model for the thermal noise. As each dynamical process in our model obeys a local detailed balance, we are able to harness the lessons of stochastic thermodynamics to define and analyze the time dependence and fluctuations of the entropy production. Note that the entropy production Σ we have referred to throughout the paper is different from the total dissipation, which is the heat released by the system, by a term ΔS - the change in the Shannon entropy of the system transistors. Nevertheless, we have used the term entropy production and dissipation interchangeably since for the timescales studied, the boundary term ΔS is orders of magnitude smaller than the cumulative term Σ, which is very large due to the large gate capacitance. This then raises the question of how to further decrease the irreversible dissipation and that associated with charging the gates. This problem is the crux of optimal control theory, and adiabatic circuit design [233, 234], from which some design principles can be borrowed. For example, while we have kept the input voltage of the transistors V_{in} fixed within each cycle, one can design optimal feedback protocol that controls it according to the state of the capacitor, in order to minimize the irreversible dissipation throughout the process. Such optimal feedback protocols already exist for simple thermodynamic engines [235], and we believe our model provides an ideal testing ground for applying more advanced stochastic control algorithms [236]. Marrying our model with a framework that integrates information with thermodynamics [237, 238], we hope to get a step closer to achieving a computing design that minimizes dissipation while maximizing accuracy and speed.

Bibliography

1. Baranyai, A. & Cummings, P. T. Steady state simulation of planar elongation flow by nonequilibrium molecular dynamics. *The Journal of Chemical Physics* **110,** 42–45 (1999).
2. Tenenbaum, A., Ciccotti, G. & Gallico, R. Stationary nonequilibrium states by molecular dynamics. Fourier's law. *Physical Review A* **25,** 2778 (1982).
3. Evans, D. J. Homogeneous NEMD algorithm for thermal conductivity – application of non-canonical linear response theory. *Physics Letters A* **91,** 457–460 (1982).
4. Hoover, W. G. *et al.* Lennard-Jones triple-point bulk and shear viscosities. Green-Kubo theory, Hamiltonian mechanics, and nonequilibrium molecular dynamics. *Physical Review A* **22,** 1690 (1980).
5. Müller-Plathe, F. A simple nonequilibrium molecular dynamics method for calculating the thermal conductivity. *The Journal of Chemical Physics* **106,** 6082–6085 (1997).
6. Tenney, C. M. & Maginn, E. J. Limitations and recommendations for the calculation of shear viscosity using reverse nonequilibrium molecular dynamics. *The Journal of Chemical Physics* **132,** 014103 (2010).
7. Tuckerman, M. E., Mundy, C. J., Balasubramanian, S. & Klein, M. L. Modified nonequilibrium molecular dynamics for fluid flows with energy conservation. *The Journal of Chemical Physics* **106,** 5615–5621 (1997).
8. Onsager, L. Reciprocal relations in irreversible processes. I. *Physical Review* **37,** 405 (1931).
9. Kubo, R. Statistical-mechanical theory of irreversible processes. I. General theory and simple applications to magnetic and conduction problems. *Journal of the Physical Society of Japan* **12,** 570–586 (1957).
10. Green, M. S. Markoff random processes and the statistical mechanics of time-dependent phenomena. II. Irreversible processes in fluids. *The Journal of Chemical Physics* **22,** 398–413 (1954).
11. Yamada, T. & Kawasaki, K. Nonlinear effects in the shear viscosity of critical mixtures. *Progress of Theoretical Physics* **38,** 1031–1051 (1967).

12. Evans, D. J. & Morriss, G. P. Transient-time-correlation functions and the rheology of fluids. *Physical Review A* **38,** 4142 (1988).

13. Crooks, G. E. Entropy production fluctuation theorem and the nonequilibrium work relation for free energy differences. *Physical Review E* **60,** 2721 (1999).

14. Gallavotti, G. & Cohen, E. G. D. Dynamical ensembles in stationary states. *Journal of Statistical Physics* **80,** 931–970 (1995).

15. Jarzynski, C. Nonequilibrium equality for free energy differences. *Physical Review Letters* **78,** 2690 (1997).

16. Barato, A. C. & Seifert, U. Thermodynamic uncertainty relation for biomolecular processes. *Physical Review Letters* **114,** 158101 (2015).

17. Gingrich, T. R., Horowitz, J. M., Perunov, N. & England, J. L. Dissipation bounds all steady-state current fluctuations. *Physical Review Letters* **116,** 120601 (2016).

18. Baiesi, M., Maes, C. & Wynants, B. Fluctuations and response of nonequilibrium states. *Physical Review Letters* **103,** 010602 (2009).

19. Harada, T. & Sasa, S.-i. Equality connecting energy dissipation with a violation of the fluctuation-response relation. *Physical Review Letters* **95,** 130602 (2005).

20. Speck, T. & Seifert, U. Extended fluctuation-dissipation theorem for soft matter in stationary flow. *Physical Review E* **79,** 040102 (2009).

21. Speck, T. & Seifert, U. Restoring a fluctuation-dissipation theorem in a nonequilibrium steady state. *Europhysics Letters* **74,** 391 (2006).

22. Basu, U. & Maes, C. *Nonequilibrium response and frenesy* in *J. Phys. Conf. Ser* **638** (2015), 012001.

23. Andrieux, D. & Gaspard, P. Fluctuation theorem and Onsager reciprocity relations. *The Journal of Chemical Physics* **121,** 6167–6174 (2004).

24. Gaspard, P. Multivariate fluctuation relations for currents. *New Journal of Physics* **15,** 115014 (2013).

25. Ellis, R. S. *Entropy, Large Deviations, and Statistical Mechanics* **821** (Taylor & Francis, 2006).

26. Touchette, H. The large deviation approach to statistical mechanics. *Physics Reports* **478,** 1–69 (2009).

27. Hedges, L. O., Jack, R. L., Garrahan, J. P. & Chandler, D. Dynamic order-disorder in atomistic models of structural glass formers. *Science* **323,** 1309–1313 (2009).

28. Hurtado, P. I. & Garrido, P. L. Spontaneous symmetry breaking at the fluctuating level. *Physical Review Letters* **107,** 180601 (2011).

29. Limmer, D. T. & Chandler, D. Theory of amorphous ices. *Proceedings of the National Academy of Sciences* **111,** 9413–9418 (2014).

30. Meixner, J., de Groot, S. & Mazur, P. *Non-equilibrium Thermodynamics* (North-Holland Publishing Company, Amsterdam, 1962).

31. Gurtin, M. E. in *Linear Theories of Elasticity and Thermoelasticity* 1–295 (Springer, 1973).

32. Irving, J. & Kirkwood, J. G. The statistical mechanical theory of transport processes. IV. The equations of hydrodynamics. *The Journal of Chemical Physics* **18,** 817–829 (1950).

33. Ferziger, J. H., Kaper, H. G. & Kaper, H. G. *Mathematical Theory of Transport Processes in Gases* (North-Holland, 1972).

34. Onsager, L. & Machlup, S. Fluctuations and irreversible processes. *Physical Review* **91,** 1505 (1953).

35. Zwanzig, R. Time-correlation functions and transport coefficients in statistical mechanics. *Annual Review of Physical Chemistry* **16,** 67–102 (1965).

36. Nitzan, A. *Chemical Dynamics in Condensed Phases: Relaxation, Transfer and Reactions in Condensed Molecular Systems* (Oxford University Press, 2006).

37. Kubo, R. Boulder Lectures in Theoretical Physics (1958).

38. Green, M. S. Markoff random processes and the statistical mechanics of time-dependent phenomena. *The Journal of Chemical Physics* **20,** 1281–1295 (1952).

39. Helfand, E. Transport coefficients from dissipation in a canonical ensemble. *Physical Review* **119,** 1 (1960).

40. Zwanzig, R. Memory effects in irreversible thermodynamics. *Physical Review* **124,** 983 (1961).

41. Evans, D. J. Rheological properties of simple fluids by computer simulation. *Physical Review A* **23,** 1988 (1981).

42. Alder, B. & Wainwright, T. Velocity autocorrelations for hard spheres. *Physical Review Letters* **18,** 988 (1967).

43. Mori, H. Statistical-mechanical theory of transport in fluids. *Physical Review* **112,** 1829 (1958).

44. Lebowitz, J. L. & Bergmann, P. G. Irreversible gibbsian ensembles. *Annals of Physics* **1,** 1–23 (1957).

45. Lebowitz, J., Percus, J. & Verlet, L. Ensemble dependence of fluctuations with application to machine computations. *Physical Review* **153,** 250 (1967).

46. Kubo, R., Yokota, M. & Nakajima, S. Statistical-mechanical theory of irreversible processes. II. Response to thermal disturbance. *Journal of the Physical Society of Japan* **12,** 1203–1211 (1957).

47. Bocquet, L. & Barrat, J.-L. Hydrodynamic boundary conditions, correlation functions, and Kubo relations for confined fluids. *Physical Review E* **49,** 3079 (1994).

48. Dyson, F. J. The radiation theories of Tomonaga, Schwinger, and Feynman. *Physical Review* **75,** 486 (1949).

49. Bochkov, G. & Kuzovlev, Y. E. General theory of thermal fluctuations in nonlinear systems. *Zh. Eksp. Teor. Fiz* **72,** 238–243 (1977).

50. Efremov, G. A fluctuation dissipation theorem for nonlinear media. *Sov. Phys. JETP* **28,** 1232 (1969).

51. Stratonovich, R. Contribution to the quantum nonlinear theory of thermal fluctuations. *Sov. Phys. JETP* **31,** 864 (1970).

52. Cohen, E. Kinetic theory of non-equilibrium fluids. *Physica A: Statistical Mechanics and its Applications* **118,** 17–42 (1983).

53. Dufty, J. W. & Lindenfeld, M. J. Nonlinear transport in the Boltzmann limit. *Journal of Statistical Physics* **20,** 259–301 (1979).

54. Visscher, W. M. Transport processes in solids and linear-response theory. *Physical Review A* **10,** 2461 (1974).

55. Kurchan, J. Fluctuation theorem for stochastic dynamics. *Journal of Physics A: Mathematical and General* **31,** 3719 (1998).

56. Lebowitz, J. L. & Spohn, H. A Gallavotti–Cohen-type symmetry in the large deviation functional for stochastic dynamics. *Journal of Statistical Physics* **95,** 333–365 (1999).

57. Basu, U., Krüger, M., Lazarescu, A. & Maes, C. Frenetic aspects of second order response. *Physical Chemistry Chemical Physics* **17,** 6653–6666 (2015).

58. Colangeli, M., Maes, C. & Wynants, B. A meaningful expansion around detailed balance. *Journal of Physics A: Mathematical and Theoretical* **44,** 095001 (2011).

59. Giardina, C., Kurchan, J., Lecomte, V. & Tailleur, J. Simulating rare events in dynamical processes. *Journal of Statistical Physics* **145,** 787–811 (2011).

60. Ray, U., Chan, G. K.-L. & Limmer, D. T. Importance sampling large deviations in nonequilibrium steady states. I. *The Journal of Chemical Physics* **148,** 124120 (2018).

61. Chetrite, R. & Touchette, H. *Nonequilibrium Markov processes conditioned on large deviations* in *Annales Henri Poincaré* **16** (2015), 2005–2057.

62. Chetrite, R. & Touchette, H. Variational and optimal control representations of conditioned and driven processes. *Journal of Statistical Mechanics: Theory and Experiment* **2015,** P12001 (2015).

63. Das, A. & Limmer, D. T. Variational control forces for enhanced sampling of nonequilibrium molecular dynamics simulations. *The Journal of Chemical Physics* **151,** 244123 (2019).

64. Giardina, C., Kurchan, J. & Peliti, L. Direct evaluation of large-deviation functions. *Physical Review Letters* **96,** 120603 (2006).

65. Bodineau, T., Lecomte, V. & Toninelli, C. Finite size scaling of the dynamical free-energy in a kinetically constrained model. *Journal of Statistical Physics* **147,** 1–17 (2012).

66. Garrahan, J. P. *et al.* First-order dynamical phase transition in models of glasses: an approach based on ensembles of histories. *Journal of Physics A: Mathematical and Theoretical* **42,** 075007 (2009).

67. Frenkel, D. & Smit, B. *Understanding Molecular Simulation: from Algorithms to Applications* (Elsevier, 2001).

68. Hidalgo, E. G., Nemoto, T. & Lecomte, V. Finite-time and finite-size scalings in the evaluation of large-deviation functions: numerical approach in continuous time. *Physical Review E* **95,** 062134 (2017).

69. Klymko, K., Geissler, P. L., Garrahan, J. P. & Whitelam, S. Rare behavior of growth processes via umbrella sampling of trajectories. *Physical Review E* **97,** 032123 (2018).

70. Nemoto, T., Jack, R. L. & Lecomte, V. Finite-size scaling of a first-order dynamical phase transition: Adaptive population dynamics and an effective model. *Physical Review Letters* **118,** 115702 (2017).

71. Nemoto, T. & Sasa, S.-i. Computation of large deviation statistics via iterative measurement-and-feedback procedure. *Physical Review Letters* **112,** 090602 (2014).

72. Ray, U., Chan, G. K.-L. & Limmer, D. T. Exact fluctuations of nonequilibrium steady states from approximate auxiliary dynamics. *Physical Review Letters* **120,** 210602 (2018).

73. Maes, C., Netočnỳ, K. & Wynants, B. Steady state statistics of driven diffusions. *Physica A: Statistical Mechanics and its Applications* **387,** 2675–2689 (2008).

74. Morriss, G. P. & Evans, D. J. Application of transient correlation functions to shear flow far from equilibrium. *Physical Review A* **35,** 792 (1987).

75. Honeycutt, R. L. Stochastic Runge-Kutta algorithms. i. white noise. *Physical Review A* **45,** 600 (1992).

76. Sivak, D. A., Chodera, J. D. & Crooks, G. E. Using nonequilibrium fluctuation theorems to understand and correct errors in equilibrium and nonequilibrium simulations of discrete Langevin dynamics. *Physical Review X* **3,** 011007 (2013).

77. Sarracino, A., Cecconi, F., Puglisi, A. & Vulpiani, A. Nonlinear response of inertial tracers in steady laminar flows: differential and absolute negative mobility. *Physical Review Letters* **117,** 174501 (2016).

78. Sendner, C., Horinek, D., Bocquet, L. & Netz, R. R. Interfacial water at hydrophobic and hydrophilic surfaces: slip, viscosity, and diffusion. *Langmuir* **25,** 10768–10781 (2009).

79. Petravic, J. & Harrowell, P. On the equilibrium calculation of the friction coefficient for liquid slip against a wall. *The Journal of Chemical Physics* **127,** 174706 (2007).

80. Huang, K. & Szlufarska, I. Green-Kubo relation for friction at liquid-solid interfaces. *Physical Review E* **89,** 032119 (2014).

81. Bocquet, L. & Barrat, J.-L. On the Green-Kubo relationship for the liquid-solid friction coefficient. *The Journal of Chemical Physics* **139,** 044704 (2013).

82. Alder, B. & Wainwright, T. Decay of the velocity autocorrelation function. *Physical Review A* **1,** 18 (1970).

83. Isobe, M. Long-time tail of the velocity autocorrelation function in a two-dimensional moderately dense hard-disk fluid. *Physical Review E* **77,** 021201 (2008).

84. Wainwright, T., Alder, B. & Gass, D. Decay of time correlations in two dimensions. *Physical Review A* **4,** 233 (1971).

85. Weeks, J. D., Chandler, D. & Andersen, H. C. Role of repulsive forces in determining the equilibrium structure of simple liquids. *The Journal of Chemical Physics* **54,** 5237–5247 (1971).

86. Che, J., Cagin, T. & Goddard III, W. A. Thermal conductivity of carbon nanotubes. *Nanotechnology* **11,** 65 (2000).

87. Jones, R. E. & Mandadapu, K. K. Adaptive Green-Kubo estimates of transport coefficients from molecular dynamics based on robust error analysis. *The Journal of Chemical Physics* **136,** 154102 (2012).

88. Gosling, E. M., McDonald, I. & Singer, K. On the calculation by molecular dynamics of the shear viscosity of a simple fluid. *Molecular Physics* **26,** 1475–1484 (1973).

89. Ashurst, W.-T. & Hoover, W. Dense-fluid shear viscosity via nonequilibrium molecular dynamics. *Physical Review A* **11,** 658 (1975).

90. Lees, A. & Edwards, S. The computer study of transport processes under extreme conditions. *Journal of Physics C: Solid State Physics* **5,** 1921 (1972).

91. Evans, D. J. & Holian, B. L. The Nose–Hoover thermostat. *The Journal of Chemical Physics* **83,** 4069–4074 (1985).

92. Hoover, W. G. Canonical dynamics: equilibrium phase-space distributions. *Physical Review A* **31,** 1695 (1985).

93. Hoover, W. G. & Ashurst, W. T. Nonequilibrium molecular dynamics. *Theoretical Chemistry: Advances and Perspectives* **1,** 1–51 (1975).

94. Evans, D. J. Molecular dynamics simulations of the rheological properties of simple fluids. *Physica A: Statistical Mechanics and its Applications* **118,** 51–68 (1983).

95. J Evans, D. & P Morriss, G. *Statistical Mechanics of Nonequilbrium Liquids* (ANU Press, 2007).

96. Dorfman, J. & Cohen, E. On the density expansion of the pair distribution function for a dense gas not in equilibrium. *Physics Letters* **16,** 124–125 (1965).

97. Dorfman, J. & Cohen, E. Velocity-correlation functions in two and three dimensions: Low density. *Physical Review A* **6,** 776 (1972).

98. Dorfman, J., Kirkpatrick, T. & Sengers, J. Generic long-range correlations in molecular fluids. *Annual Review of Physical Chemistry* **45,** 213–239 (1994).

99. Yamada, T. & Kawasaki, K. Application of mode-coupling theory to nonlinear stress tensor in fluids. *Progress of Theoretical Physics* **53,** 111–124 (1975).

100. Bertini, L., Chetrite, R., Faggionato, A. & Gabrielli, D. *Level 2.5 large deviations for continuous-time Markov chains with time periodic rates* in *Annales Henri Poincaré* **19** (2018), 3197–3238.

101. Harned, H. S., Owen, B. B. & King, C. The physical chemistry of electrolytic solutions. *Journal of The Electrochemical Society* **106,** 15C (1959).

102. Onsager, L. Report on a revision of the conductivity theory. *Transactions of the Faraday Society* **23,** 341–349 (1927).

103. Onsager, L. & Fuoss, R. Irreversible processes in electrolytes. Diffusion, conductance and viscous flow in arbitrary mixtures of strong electrolytes. *The Journal of Physical Chemistry* **36,** 2689–2778 (2002).

104. Onsager, L. & Kim, S. K. The relaxation effects in mixed strong electrolytes. *The Journal of Physical Chemistry* **61,** 215–229 (1957).

105. Onsager, L. & Kim, S. K. Wien effect in simple strong electrolytes. *The Journal of Physical Chemistry* **61,** 198–215 (1957).

106. Fuoss, R. M. & Onsager, L. Conductance of unassociated electrolytes. *The Journal of Physical Chemistry* **61,** 668–682 (1957).

107. Kaiser, V., Bramwell, S. T., Holdsworth, P. C. & Moessner, R. Onsager's Wien effect on a lattice. *Nature Materials* **12,** 1033–1037 (2013).

108. Ryu, J. C., Park, H. J., Park, J. K. & Kang, K. H. New electrohydrodynamic flow caused by the Onsager effect. *Physical Review Letters* **104,** 104502 (2010).

109. Wilson, S. *The theory of the Wien effect for a binary electrolyte* PhD thesis (Yale University, 1936).

110. Glarum, S. H. Dielectric relaxation of polar liquids. *The Journal of Chemical Physics* **33,** 1371–1375 (1960).

111. Klug, D., Kranbuehl, D. & Vaughan, W. Molecular correlation functions and dielectric relaxation. *The Journal of Chemical Physics* **50,** 3904–3905 (1969).

112. Nee, T.-W. & Zwanzig, R. Theory of dielectric relaxation in polar liquids. *The Journal of Chemical Physics* **52,** 6353–6363 (1970).

113. Démery, V. & Dean, D. S. The conductivity of strong electrolytes from stochastic density functional theory. *Journal of Statistical Mechanics: Theory and Experiment* **2016,** 023106 (2016).

114. Esfandiar, A. *et al.* Size effect in ion transport through angstrom-scale slits. *Science* **358,** 511–513 (2017).

115. Mouterde, T. *et al.* Molecular streaming and its voltage control in ångström-scale channels. *Nature* **567,** 87–90 (2019).

116. Secchi, E., Niguès, A., Jubin, L., Siria, A. & Bocquet, L. Scaling behavior for ionic transport and its fluctuations in individual carbon nanotubes. *Physical Review Letters* **116,** 154501 (2016).

117. Siria, A. *et al.* Giant osmotic energy conversion measured in a single transmembrane boron nitride nanotube. *Nature* **494,** 455–458 (2013).

118. Feng, J. *et al.* Observation of ionic Coulomb blockade in nanopores. *Nature Materials* **15,** 850–855 (2016).

119. Guan, W., Fan, R. & Reed, M. A. Field-effect reconfigurable nanofluidic ionic diodes. *Nature Communications* **2,** 1–8 (2011).

120. Karnik, R., Duan, C., Castelino, K., Daiguji, H. & Majumdar, A. Rectification of ionic current in a nanofluidic diode. *Nano Letters* **7,** 547–551 (2007).

121. Kim, S. J., Wang, Y.-C., Lee, J. H., Jang, H. & Han, J. Concentration polarization and nonlinear electrokinetic flow near a nanofluidic channel. *Physical Review Letters* **99,** 044501 (2007).

122. Vermesh, U. *et al.* Fast nonlinear ion transport via field-induced hydrodynamic slip in sub-20-nm hydrophilic nanofluidic transistors. *Nano Letters* **9,** 1315–1319 (2009).

123. Cheng, L.-J. & Guo, L. J. Nanofluidic diodes. *Chemical Society Reviews* **39,** 923–938 (2010).

124. He, Y. *et al.* Tuning transport properties of nanofluidic devices with local charge inversion. *Journal of the American Chemical Society* **131,** 5194–5202 (2009).

125. Picallo, C. B., Gravelle, S., Joly, L., Charlaix, E. & Bocquet, L. Nanofluidic osmotic diodes: Theory and molecular dynamics simulations. *Physical Review Letters* **111,** 244501 (2013).

126. Koneshan, S., Lynden-Bell, R. & Rasaiah, J. C. Friction coefficients of ions in aqueous solution at 25 C. *Journal of the American Chemical Society* **120,** 12041–12050 (1998).

127. Fumi, F. & Tosi, M. Ionic sizes and born repulsive parameters in the NaCl-type alkali halides – I: The Huggins-Mayer and Pauling forms. *Journal of Physics and Chemistry of Solids* **25,** 31–43 (1964).

128. Cugliandolo, L. F., Lecomte, V. & Van Wijland, F. Building a path-integral calculus: a covariant discretization approach. *Journal of Physics A: Mathematical and Theoretical* **52,** 50LT01 (2019).

129. Dzubiella, J., Hoffmann, G. & Löwen, H. Lane formation in colloidal mixtures driven by an external field. *Physical Review E* **65,** 021402 (2002).

130. Kavokine, N., Marbach, S., Siria, A. & Bocquet, L. Ionic Coulomb blockade as a fractional Wien effect. *Nature Nanotechnology* **14,** 573–578 (2019).

131. Péraud, J.-P., Nonaka, A. J., Bell, J. B., Donev, A. & Garcia, A. L. Fluctuation-enhanced electric conductivity in electrolyte solutions. *Proceedings of the National Academy of Sciences* **114,** 10829–10833 (2017).

132. Wolynes, P. G. Dynamics of electrolyte solutions. *Annual Review of Physical Chemistry* **31,** 345–376 (1980).

133. Habershon, S., Markland, T. E. & Manolopoulos, D. E. Competing quantum effects in the dynamics of a flexible water model. *The Journal of Chemical Physics* **131,** 024501 (2009).

134. Thompson, A. P. & Plimpton, S. J. *LAMMPS: A general open-source framework for particle-based simulation of materials on multiple scales.* tech. rep. (Sandia National Lab., Albuquerque, NM (United States), 2016).

135. Saitta, A. M., Saija, F. & Giaquinta, P. V. Ab initio molecular dynamics study of dissociation of water under an electric field. *Physical Review Letters* **108,** 207801 (2012).

136. Dufrêche, J.-F., Bernard, O., Turq, P., Mukherjee, A. & Bagchi, B. Ionic self-diffusion in concentrated aqueous electrolyte solutions. *Physical Review Letters* **88,** 095902 (2002).

137. Daily, J. W. & Micci, M. M. Ionic velocities in an ionic liquid under high electric fields using all-atom and coarse-grained force field molecular dynamics. *The Journal of Chemical Physics* **131,** 094501 (2009).

138. Heid, E. & Schröder, C. Solvation dynamics in polar solvents and imidazolium ionic liquids: failure of linear response approximations. *Physical Chemistry Chemical Physics* **20,** 5246–5255 (2018).

139. Netz, R. Electrofriction and dynamic stern layers at planar charged surfaces. *Physical Review Letters* **91,** 138101 (2003).

140. Sedlmeier, F., Shadkhoo, S., Bruinsma, R. & Netz, R. R. Charge/mass dynamic structure factors of water and applications to dielectric friction and electroacoustic conversion. *The Journal of Chemical Physics* **140,** 054512 (2014).

141. Balos, V. *et al.* Macroscopic conductivity of aqueous electrolyte solutions scales with ultrafast microscopic ion motions. *Nature Communications* **11,** 1–8 (2020).

142. Chandra, A. & Bagchi, B. Frequency dependence of ionic conductivity of electrolyte solutions. *The Journal of Chemical Physics* **112,** 1876–1886 (2000).

143. Jin, Y. *et al.* Coupling effects in electromechanical ion transport in graphene nanochannels. *Physical Review E* **102,** 033112 (2020).

144. Palmer, B. J., Chun, J., Morris, J. F., Mundy, C. J. & Schenter, G. K. Correlation function approach for diffusion in confined geometries. *Physical Review E* **102,** 022129 (2020).

145. Pean, C. *et al.* Confinement, desolvation, and electrosorption effects on the diffusion of ions in nanoporous carbon electrodes. *Journal of the American Chemical Society* **137,** 12627–12632 (2015).

146. Simonnin, P., Marry, V., Noetinger, B., Nieto-Draghi, C. & Rotenberg, B. Mineral-and ion-specific effects at clay-water interfaces: structure, diffusion, and hydrodynamics. *The Journal of Physical Chemistry C* **122,** 18484–18492 (2018).

147. Chang, C. W., Okawa, D., Majumdar, A. & Zettl, A. Solid-state thermal rectifier. *Science* **314,** 1121–1124 (2006).

148. Chang, C.-W., Okawa, D., Garcia, H., Majumdar, A. & Zettl, A. Breakdown of Fourier's law in nanotube thermal conductors. *Physical Review Letters* **101,** 075903 (2008).

149. Wang, M., Yang, N. & Guo, Z.-Y. Non-Fourier heat conductions in nanomaterials. *Journal of Applied Physics* **110,** 064310 (2011).

150. Xu, X. *et al.* Length-dependent thermal conductivity in suspended single-layer graphene. *Nature Communications* **5,** 1–6 (2014).

151. Yang, N., Zhang, G. & Li, B. Violation of Fourier's law and anomalous heat diffusion in silicon nanowires. *Nano Today* **5,** 85–90 (2010).

152. Narayan, O. & Ramaswamy, S. Anomalous heat conduction in one-dimensional momentum-conserving systems. *Physical Review Letters* **89,** 200601 (2002).

153. Spohn, H. Nonlinear fluctuating hydrodynamics for anharmonic chains. *Journal of Statistical Physics* **154,** 1191–1227 (2014).

154. Lepri, S. Relaxation of classical many-body Hamiltonians in one dimension. *Physical Review E* **58,** 7165 (1998).

155. Scheipers, J. & Schirmacher, W. Mode-coupling theory for the lattice dynamics of anharmonic crystals: self-consistent damping and the 1d Lennard-Jones chain. *Zeitschrift für Physik B Condensed Matter* **103,** 547–553 (1997).

156. Lepri, S., Livi, R. & Politi, A. Heat conduction in chains of nonlinear oscillators. *Physical Review Letters* **78,** 1896 (1997).

157. Lepri, S., Livi, R. & Politi, A. Energy transport in anharmonic lattices close to and far from equilibrium. *Physica D: Nonlinear Phenomena* **119,** 140–147 (1998).

158. Lepri, S., Livi, R. & Politi, A. On the anomalous thermal conductivity of one-dimensional lattices. *Europhysics Letters* **43,** 271 (1998).

159. Zabusky, N. J. & Kruskal, M. D. Interaction of "solitons" in a collisionless plasma and the recurrence of initial states. *Physical Review Letters* **15,** 240 (1965).

160. Blanco-Redondo, A. *et al.* Observation of soliton compression in silicon photonic crystals. *Nature Communications* **5,** 1–8 (2014).

161. Toda, M. Solitons and heat conduction. *Physica Scripta* **20,** 424 (1979).

162. Casati, G., Ford, J., Vivaldi, F. & Visscher, W. M. One-dimensional classical many-body system having a normal thermal conductivity. *Physical Review Letters* **52,** 1861 (1984).

163. Prosen, T. & Robnik, M. Energy transport and detailed verification of Fourier heat law in a chain of colliding harmonic oscillators. *Journal of Physics A: Mathematical and General* **25,** 3449 (1992).

164. Tsironis, G., Bishop, A., Savin, A. & Zolotaryuk, A. Dependence of thermal conductivity on discrete breathers in lattices. *Physical Review E* **60,** 6610 (1999).

165. Roberts, N. A. & Walker, D. A review of thermal rectification observations and models in solid materials. *International Journal of Thermal Sciences* **50,** 648–662 (2011).

166. Pereira, E. Graded anharmonic crystals as genuine thermal diodes: analytical description of rectification and negative differential thermal resistance. *Physical Review E* **82,** 040101 (2010).

167. Shah, T. N. & Gajjar, P. Study of thermal conductivity and thermal rectification in exponential mass graded lattices. *Physics Letters A* **376,** 438–441 (2012).

168. Yang, N., Li, N., Wang, L. & Li, B. Thermal rectification and negative differential thermal resistance in lattices with mass gradient. *Physical Review B* **76,** 020301 (2007).

169. Payton III, D. N., Rich, M. & Visscher, W. M. Lattice thermal conductivity in disordered harmonic and anharmonic crystal models. *Physical Review* **160,** 706 (1967).

170. Dhar, A., Saito, K. & Derrida, B. Exact solution of a Lévy walk model for anomalous heat transport. *Physical Review E* **87,** 010103 (2013).

171. Lepri, S. & Politi, A. Density profiles in open superdiffusive systems. *Physical Review E* **83,** 030107 (2011).

172. Lepri, S., Livi, R. & Politi, A. Thermal conduction in classical low-dimensional lattices. *Physics Reports* **377,** 1–80 (2003).

173. Pettini, M., Casetti, L., Cerruti-Sola, M., Franzosi, R. & Cohen, E. Weak and strong chaos in Fermi–Pasta–Ulam models and beyond. *Chaos: An Interdisciplinary Journal of Nonlinear Science* **15,** 015106 (2005).

174. Li, N. & Li, B. Temperature dependence of thermal conductivity in 1D nonlinear lattices. *Europhysics Letters* **78,** 34001 (2007).

175. Li, N., Liu, J., Wu, C. & Li, B. Temperature and frequency dependent mean free paths of renormalized phonons in nonlinear lattices. *New Journal of Physics* **20,** 023006 (2018).

176. Ming, Y. *et al.* Numerical extraction of sound velocities of energy transfer based on solitons in Fermi-Pasta-Ulam chains. *Physical Review E* **98,** 032215 (2018).

177. Jin, T., Yu, J., Zhang, N. & Zhao, H. Scattering of lattice solitons and decay of heat-current correlation in the Fermi-Pasta-Ulam-α- β model. *Physical Review E* **96,** 022116 (2017).

178. Arévalo, E., Mertens, F. G., Gaididei, Y. & Bishop, A. Thermal diffusion of supersonic solitons in an anharmonic chain of atoms. *Physical Review E* **67,** 016610 (2003).

179. Bennett, C. H. Notes on Landauer's principle, reversible computation, and Maxwell's Demon. *Studies In History and Philosophy of Science Part B: Studies In History and Philosophy of Modern Physics* **34,** 501–510 (2003).

180. Landauer, R. *Maxwell's Demon: Entropy, Information, Computing* (Princeton University Press, 1990).

181. Parrondo, J. M., Horowitz, J. M. & Sagawa, T. Thermodynamics of information. *Nature Physics* **11,** 131–139 (2015).

182. Wolpert, D. H. The stochastic thermodynamics of computation. *Journal of Physics A: Mathematical and Theoretical* **52,** 193001 (2019).

183. Johnson, J. B. Thermal agitation of electricity in conductors. *Physical Review* **32,** 97 (1928).

184. Nyquist, H. Thermal agitation of electric charge in conductors. *Physical Review* **32,** 110 (1928).

185. Van Der Ziel, A. Noise in solid-state devices and lasers. *Proceedings of the IEEE* **58,** 1178–1206 (1970).

186. Heinen, S., Kunisch, J. & Wolff, I. A unified framework for computer-aided noise analysis of linear and nonlinear microwave circuits. *IEEE Transactions on Microwave Theory and Techniques* **39,** 2170–2175 (1991).

187. Rizzoli, V. & Neri, A. State of the art and present trends in nonlinear microwave CAD techniques. *IEEE Transactions on Microwave Theory and Techniques* **36,** 343–365 (1988).

188. Maes, C. On the second fluctuation–dissipation theorem for nonequilibrium baths. *Journal of Statistical Physics* **154,** 705–722 (2014).

189. Gao, C. Y. & Limmer, D. T. Nonlinear transport coefficients from large deviation functions. *The Journal of Chemical Physics* **151,** 014101 (2019).

190. Lesnicki, D., Gao, C. Y., Rotenberg, B. & Limmer, D. T. Field-dependent ionic conductivities from generalized fluctuation-dissipation relations. *Physical Review Letters* **124,** 206001 (2020).

191. Kish, L. B. End of Moore's law: thermal (noise) death of integration in micro and nano electronics. *Physics Letters A* **305,** 144–149 (2002).

192. Seifert, U. Stochastic thermodynamics, fluctuation theorems and molecular machines. *Reports on Progress in Physics* **75,** 126001 (2012).

193. Cover, T. M. *Elements of Information Theory* (John Wiley & Sons, 1999).

194. Shannon, C. E. A mathematical theory of communication. *The Bell System Technical Journal* **27,** 379–423 (1948).

195. Jarzynski, C. Equalities and inequalities: Irreversibility and the second law of thermodynamics at the nanoscale. *Annu. Rev. Condens. Matter Phys.* **2,** 329–351 (2011).

196. Falasco, G. & Esposito, M. Dissipation-time uncertainty relation. *Physical Review Letters* **125,** 120604 (2020).

197. Ito, S. Stochastic thermodynamic interpretation of information geometry. *Physical Review Letters* **121,** 030605 (2018).

198. Ito, S. & Dechant, A. Stochastic time evolution, information geometry, and the Cramér-Rao bound. *Physical Review X* **10,** 021056 (2020).

199. Kuznets-Speck, B. & Limmer, D. T. Dissipation bounds the amplification of transition rates far from equilibrium. *Proceedings of the National Academy of Sciences* **118** (2021).

200. Shiraishi, N., Funo, K. & Saito, K. Speed limit for classical stochastic processes. *Physical Review Letters* **121,** 070601 (2018).

201. Gingrich, T. R., Rotskoff, G. M. & Horowitz, J. M. Inferring dissipation from current fluctuations. *Journal of Physics A: Mathematical and Theoretical* **50,** 184004 (2017).

202. Horowitz, J. M. & Gingrich, T. R. Proof of the finite-time thermodynamic uncertainty relation for steady-state currents. *Physical Review E* **96,** 020103 (2017).

203. Lahiri, S., Sohl-Dickstein, J. & Ganguli, S. A universal tradeoff between power, precision and speed in physical communication. *arXiv:1603.07758* (2016).

204. Banerjee, K., Kolomeisky, A. B. & Igoshin, O. A. Elucidating interplay of speed and accuracy in biological error correction. *Proceedings of the National Academy of Sciences* **114,** 5183–5188 (2017).

205. Murugan, A., Huse, D. A. & Leibler, S. Speed, dissipation, and error in kinetic proofreading. *Proceedings of the National Academy of Sciences* **109,** 12034–12039 (2012).

206. Piñeros, W. D. & Tlusty, T. Kinetic proofreading and the limits of thermodynamic uncertainty. *Physical Review E* **101,** 022415 (2020).

207. Rao, R. & Peliti, L. Thermodynamics of accuracy in kinetic proofreading: Dissipation and efficiency trade-offs. *Journal of Statistical Mechanics: Theory and Experiment* **2015,** P06001 (2015).

208. Wang, T.-L., Kuznets-Speck, B., Broderick, J. & Hinczewski, M. The price of a bit: energetic costs and the evolution of cellular signaling. *bioRxiv* (2020).

209. Plenio, M. B. & Vitelli, V. The physics of forgetting: Landauer's erasure principle and information theory. *Contemporary Physics* **42,** 25–60 (2001).

210. Sagawa, T. & Ueda, M. Information thermodynamics: Maxwell's demon in nonequilibrium dynamics. *Nonequilibrium Statistical Physics of Small Systems: Fluctuation Relations and Beyond,* 181–211 (2013).

211. Still, S., Sivak, D. A., Bell, A. J. & Crooks, G. E. Thermodynamics of prediction. *Physical Review Letters* **109,** 120604 (2012).

212. Wolpert, D. & Kolchinsky, A. The thermodynamics of computing with circuits. *New Journal of Physics* (2020).

213. Bagrets, D. & Nazarov, Y. V. Full counting statistics of charge transfer in Coulomb blockade systems. *Physical Review B* **67,** 085316 (2003).

214. Devoret, M. H. *et al.* Effect of the electromagnetic environment on the Coulomb blockade in ultrasmall tunnel junctions. *Physical Review Letters* **64,** 1824 (1990).

215. Wasshuber, C. *Computational Single-Electronics* (Springer Science & Business Media, 2001).

216. Freitas, N., Delvenne, J.-C. & Esposito, M. Stochastic thermodynamics of nonlinear electronic circuits: a realistic framework for thermodynamics of computation. *arXiv:2008.10578* (2020).

217. Gu, J. & Gaspard, P. Counting statistics and microreversibility in stochastic models of transistors. *Journal of Statistical Mechanics: Theory and Experiment* **2020,** 103206 (2020).

218. Gu, J. & Gaspard, P. Microreversibility, fluctuations, and nonlinear transport in transistors. *Physical Review E* **99,** 012137 (2019).

219. Esposito, M., Harbola, U. & Mukamel, S. Fluctuation theorem for counting statistics in electron transport through quantum junctions. *Physical Review B* **75,** 155316 (2007).

220. Nakamura, S. *et al.* Fluctuation theorem and microreversibility in a quantum coherent conductor. *Physical Review B* **83,** 155431 (2011).

221. Datta, S. *Electronic Transport in Mesoscopic Systems* (Cambridge University Press, 1997).

222. Wachtel, A., Rao, R. & Esposito, M. Thermodynamically consistent coarse graining of biocatalysts beyond Michaelis–Menten. *New Journal of Physics* **20,** 042002 (2018).

223. Datta, S. A simple kinetic equation for steady-state quantum transport. *Journal of Physics: Condensed Matter* **2,** 8023 (1990).

224. Harbola, U., Esposito, M. & Mukamel, S. Quantum master equation for electron transport through quantum dots and single molecules. *Physical Review B* **74,** 235309 (2006).

225. Leijnse, M. & Wegewijs, M. Kinetic equations for transport through single-molecule transistors. *Physical Review B* **78,** 235424 (2008).

226. Koski, J. V., Maisi, V. F., Sagawa, T. & Pekola, J. P. Experimental observation of the role of mutual information in the nonequilibrium dynamics of a Maxwell demon. *Physical Review Letters* **113,** 030601 (2014).

227. Koski, J. *et al.* Distribution of entropy production in a single-electron box. *Nature Physics* **9,** 644–648 (2013).

228. Breuer, H.-P. & Petruccione, F. *The Theory of Open Quantum Systems* (Oxford University Press, 2002).

229. Gillespie, D. T. A general method for numerically simulating the stochastic time evolution of coupled chemical reactions. *Journal of Computational Physics* **22,** 403–434 (1976).

230. Crooks, G. E. Field guide to continuous probability distributions. *Berkeley Institute for Theoretical Sciences, Berkeley* (2019).

231. Verdú, S. *et al.* A general formula for channel capacity. *IEEE Transactions on Information Theory* **40,** 1147–1157 (1994).

232. Rahman, A. & Blackmore, D. Threshold voltage dynamics of chaotic RS flip-Flops. *Chaos, Solitons & Fractals* **103,** 555–566 (2017).

233. Frank, M. P. Common mistakes in adiabatic logic design and how to avoid them. *Embedded Systems and Applications* **216** (2003).

234. Zulehner, A., Frank, M. P. & Wille, R. *Design automation for adiabatic circuits* in *Proceedings of the 24th Asia and South Pacific Design Automation Conference* (2019), 669–674.

235. Horowitz, J. M. & Parrondo, J. M. Designing optimal discrete-feedback thermodynamic engines. *New Journal of Physics* **13,** 123019 (2011).

236. Das, A. & Limmer, D. T. Variational design principles for nonequilibrium colloidal assembly. *The Journal of Chemical Physics* **154,** 014107 (2021).

237. Barato, A. C. & Seifert, U. Stochastic thermodynamics with information reservoirs. *Physical Review E* **90,** 042150 (2014).

238. Deffner, S. & Jarzynski, C. Information processing and the second law of thermodynamics: An inclusive, Hamiltonian approach. *Physical Review X* **3,** 041003 (2013).